Use Authorization

In presenting this thesis in partial fulfillment of the requirements for an advanced degree at Idaho State University, I agree that the Library shall make it freely available for inspection. I further state that permission for extensive copying of my thesis for scholarly purposes may be granted by the Dean of the Graduate School, Dean of my academic division, or by the University Librarian. It is understood that any copying or publication of this thesis for financial gain shall not be allowed without my written permission.

Signature_____

Date_____

SIMILARITY SCALING EFFECTS ON THE THERMAL HYDRAULIC BEHAVIOR OF A RANDOMLY PACKED PB-FHR CORE USING A SURROGATE FLUID

by

Scott Wahlquist

Thesis

submitted in partial fulfillment

of the requirements for the degree of

Master of Science in the Department of Nuclear Engineering

Idaho State University

Spring 2022

To the Graduate Faculty:

The members of the committee appointed to examine the thesis of Scott Wahlquist find it satisfactory and recommend that it be accepted.

_____

Dr. Amir Ali,
Major Advisor, Committee Chair

_____

Dr. Su-Jong Yoon,
Committee Member

_____

Dr. Richard Schultz,
Committee Member

_____

Dr. Anish Sebastian,
Graduate Faculty Representative

Acknowledgments

I want to thank my parents, Steve and Lita Wahlquist, for their support and encouragement in pushing me to do my best. A special thanks to my advisor Dr. Amir F. Ali, for the invaluable knowledge he passed on to me and the many additional projects I have been privileged to work with him on in tandem with this thesis project. I want to thank my committee members Dr. Su-Jong Yoon, Dr. Richard Schultz, and Dr. Anish Sebastian, for their invaluable feedback.

Table of Contents

List of Figures.....vii
List of Tables.....x
List of Abbreviations.....xiii
List of Symbols.....xiv
Abstract.....xv
Chapter 1: Introduction.....1
1-1. PB-FHR Technological Characteristics.....2
1-2. Mk-1 PB-FHR General Description.....3
1.2.1. TRISO Particle Fuel.....4
1.2.2. Direct Reactor Auxiliary Cooling System.....6
1.2.3. Liquid Fluoride Salt Coolants.....7
1-3. Literature Review.....7
1-4. Research Objectives.....11
1-5. Significance of Study.....12
1-6. Assumptions/Limitations/Delimitations.....12
Chapter 2: Numerical Methodology.....14
2-1. Fluid Flow in Packed Beds.....14
2-2. Heat Transfer in Packed Beds.....15
2-3. Conservation Equations.....17
2.3.1. Continuity (Mass) Equation.....17
2.3.2. Momentum Equation.....17
2.3.3. Energy Equation.....18
2-4. Finite Volume Methodology.....18
2-5. Geometrical Flow Path Design.....19
2.5.1. MATLAB Code.....20
2.5.2. Geometric Flow Path Generation.....21
2-6. Mesh Generation.....22
2.6.1. y+ Boundary Layer Theory.....22
2.6.2. Discretization Error Methods.....23
Chapter 3: Numerical Setup.....26
3-1. Thermophysical Properties of FLiBe.....26
3.1.1. History and Relevance of FLiBe.....27
3.1.2. Density.....30

3.1.3. Dynamic Viscosity 31
3.1.4. Specific Heat Capacity 32
3.1.5. Thermal Conductivity 32
3.1.6. Ideal Thermophysical Properties 32
3-2. Model Validation 34
3-3. Effects of Mesh and Gap Size 36
3.3.1. y+ Analysis Results 37
3.3.2. Results of Gap Size Analysis 37
3.3.3. Results of Mesh Sensitivity Analysis 41
3-4. Effects of Number of Pebbles 42
Chapter 4: Scaling Methodology 46
4-1. Surrogate Fluid Utilization in Scaled Experiments 46
4-2. Potential Candidates of FLiBe Surrogate Fluids 47
4-3. Thermophysical Properties of Dowtherm-A 47
4-4. Scaling Methodology 49
4.4.1. Thermophysical Property Ratios 50
4.4.2. Geometrical Parameter Ratios 54
4.4.3. Flow Conditions Ratios 55
4.4.4. Heating Power Ratios 56
4-5. Scaling Distortion Theory 59
Chapter 5: Numerical Results and Discussion 60
5-1. Results of FLiBe Cases 60
5.1.1. Comparison with Established Correlations 61
5.1.2. Development of FLiBe Nu Correlation 66
5-2. Results of Dowtherm-A Cases 67
5.2.1. Development of Dowtherm-A Nu Correlation 68
5-3. Comparative Analysis between FLiBe and Dowtherm-A 70
5-4. Development of Nu Distortion Correction Factor 72
Chapter 6: Conclusion and Future Work 74
6-1. Summary of Results 74
6-2. Future Work 76
6-3. Conclusion 76
6-4. List of Publications 77
References 78
Appendix A: Sample of Mesh Sensitivity Data 84

Appendix B: Sample of Similarity Scaling Data 90
Appendix C: Sample of Numerical Data 105

List of Figures

Figure 1. Diagram detailing the main salt loop, DRACS loops, and NACC power conversion system. 3
Figure 2. Layers of general TRISO fuel particle utilized in several pebble bed reactors. 6
Figure 3. (a) Cross-section of pebble typically used in gas-cooled pebble bed reactors; (b) Cross-section of pebble used for the Mk-1 PB-FHR. 6
Figure 4. (a) Gap method by introducing an artificial gap between each pebble; (b) Gap method by slightly reducing the diameter of each sphere. The dashed lines represent the original size of each sphere. 10
Figure 5. Cap method, which flattens the surface perpendicular to each adjacent pebble. 10
Figure 6. (a) Overlap method creates a contact zone between each adjacent pebble. The dashed lines represent the overlap region between pebbles; (b) the bridge creates cylindrical bridges at near-contact points between adjacent pebbles. 10
Figure 7. The analyzed bulk temperature section was reduced by two times the pebble radius to avoid near-wall effects. 16
Figure 8. Reducing the post-processing domain reduces the void fraction and eliminates the wall effect. The reduced void fraction is akin to the Mk-1 PB-FHR core porosity. 16
Figure 9. Example of node locations for the finite volume method. An example of a control volume is highlighted in yellow. 19
Figure 10. Flow chart of the iterative process in determining the center points of a specified number of spheres in a cylindrical domain. 20
Figure 11. Figure outputted from MATLAB code shows pebbles' location once each sphere is modeled. The figure shows 50 pebbles with a 0.01-mm minimum gap size between pebbles. 21
Figure 12. Plotted thermophysical properties over the range of 875 < T < 1250 K. 33
Figure 13. Geometries of randomly packed pebble bed channels used for validation purposes. 36
Figure 14. Comparison between the validation data and the current simulation work. 36
Figure 15. Comparison of mesh refinements: (a) 0.735-mm mesh with 1.5-mm prism layer thickness; (b) 0.735-mm mesh with 100% relative prism layer thickness, (c) 0.5-mm mesh with 100% relative prism layer thickness. 38
Figure 16. Effects of various minimum gap sizes on the Nu and ΔP for Pr = 15.0. 40
Figure 17. Finalized refined mesh shown for 50 randomly packed pebbles. 42
Figure 18. Determination of N using the finalized mesh specification and δp. 43

Figure 19. (a) Results for N = 40, 50, 60, 75, and 100 for 500 < Re < 2500 and Pr = 15.0; (b) Average percentage difference with increasing number of pebbles. 44
Figure 20. (a) Results for Re vs. ΔP for N = 40, 50, 60, 75, and 100 with Pr = 15.0; (b) Results for Re vs. normalized ΔP with Pr = 15.0. 45
Figure 21. Comparison between Dowtherm-A data and polynomial equations using developed regression coefficients. 49
Figure 22. Geometries of varying scales for surrogate fluid cases. 51
Figure 23. Equivalent temperatures of FLiBe and Dowtherm-A that match Pr = 19.4. 52
Figure 24. Equivalent temperatures of FLiBe and Dowtherm-A that match Pr = 15.0. 52
Figure 25. Equivalent temperatures of FLiBe and Dowtherm-A that match Pr = 11.9. 53
Figure 26. Equivalent temperatures of FLiBe and Dowtherm-A that match Pr = 9.64. 53
Figure 27. Equivalent temperatures of FLiBe and Dowtherm-A that match Pr = 7.95. 54
Figure 28. Change in superficial velocity at various Pr for all investigated length scales. 57
Figure 29. Power provided to each pebble for each reduced length scale case and Pr. 58
Figure 30. Similitude theory as applied for fluid mechanics and convective heat transfer for this analysis 59
Figure 31. Results of Nu and ΔP for flowing FLiBe for the ranges of 500 < Re < 2500 and 7.95 < Pr < 19.4. 60
Figure 32. Temperature and pressure contour of a vertical cross-section of test section at various Re and Pr. 62
Figure 33. Comparison of various Nu correlations to current simulation data for Pr = 15.0. 63
Figure 34. The Nu relative error when compared to the Wakao correlation increases as the core temperature increases. 64
Figure 35. Development of Nu correlation using several experimental data sets. The top legend represents solutions at steady-state, and the bottom legend represents unsteady-state solutions. The data collected for this analysis are compared with all data sets. 65
Figure 36. Comparison of collected ΔP and f data for N = 75 pebbles and Pr = 15.0 with previous pebble bed correlations developed for low-Pr fluids. 66
Figure 37. Development of FLiBe Nu correlation in a randomly packed pebble bed for the range of 500 < Re < 2500 and 7.95 < Pr < 19.4. 67
Figure 38. Nu data comparison between collected simulation data (marker) and developed correlation (line). 67
Figure 39. Results of Nu and ΔP for Dowtherm-A for 500 < Re < 2500 and 7.95 < Pr < 19.4. 69

Figure 40. Development of Nu correlation for all investigated length scales (1:1, 0.75:1, and 0.5:1). 70
Figure 41. Nu data comparison between collected simulation data (marker) and developed correlation (line) for all investigated length scales. 71
Figure 42. Comparison between all reduced length scales and FLiBe showed similar distortion levels for all investigated Pr. 72
Figure 43. Comparison between FLiBe Nu data results and Dowtherm-A Nu data results with the introduced distortion correction factor. 73
Figure 44: Simple schematic of potential heat transfer facility for experimentally quantifying the thermal-hydraulic behavior of a PB-FHR core. 76

List of Tables

Table 1. Mk-1 PB-FHR TRISO fuel particle design [3]. 5
Table 2. Geometrical specifications of Mk-1 PB-FHR fuel (Technical description). 6
Table 3. The chosen thermophysical properties for LiF-BeF2 with 66-37 mol% composition for this analysis. 33
Table 4. Prism layer analysis results using a forced $y+$ = 1 for Pr = 15.0. 37
Table 5. Nu comparison of the gap size between pebbles and the base element size for 50 pebbles with Pr = 15.0 and Re = 2500. 39
Table 6. ΔP comparison of the gap size between pebbles and the base element size for 50 pebbles with Pr = 15.0 and Re = 2500. 39
Table 7. Nu Grid convergence index analysis of Pr = 15.0 for Re = 500, 1250, and 2500. 41
Table 8. ΔP Grid convergence index analysis of Pr = 15.0 for Re = 500, 1250, and 2500. 41
Table 9. The relative error for extended pebble count study using validation data initial and boundary conditions. 43
Table 10. Regression coefficients for single-phase thermophysical properties of Dowtherm-A. 49
Table 11. Equivalent temperatures between FLiBe and Dowtherm-A that produces identical Pr. 50
Table 12. The thermophysical property ratios determined by matching Pr at certain temperatures. 54
Table 13. Dimensional scaling based on length scale factor 55
Table 14. The geometrical parameters used to create geometry surrounding the pebble domain based on length scale factor 55
Table 15. Velocity ratios for each investigated Pr and length scale. 56
Table 16. Determination of power ratio required for reduced scales at various Pr. 58
Table 17. List of Nu correlations applicable to investigated Re and Pr ranges from this study. 62
Table 18. Minimum gap thickness study for δ = 0.05 mm at various mesh sizes with 100% relative prism layer thickness. 84
Table 19. Minimum gap thickness study for δ = 0.01 mm at various mesh sizes with 100% relative prism layer thickness. 85
Table 20. Minimum gap thickness study for δ = 0.005 mm at various mesh sizes with 100% relative prism layer thickness. 86
Table 21. Grid Convergence Index (GCI) discretization error for δ = 0.05 mm at Re = 500, 1250, and 2500. 87

Table 22. Grid Convergence Index (GCI) discretization error for δ = 0.01 mm at Re = 500, 1250, and 2500. 88
Table 23. Grid Convergence Index (GCI) discretization error for δ = 0.005 mm at Re = 500, 1250, and 2500. 89
Table 24. Similarity scaling results between FLiBe and Dowtherm-A at full scale (1:1 scale) for Pr = 19.4. 90
Table 25. Requisite flow conditions between FLiBe and Dowtherm-A at full scale (1:1 scale) for Pr = 19.4. 91
Table 26. Similarity scaling results between FLiBe and Dowtherm-A at full scale (1:1 scale) for Pr = 7.95. 92
Table 27. Requisite flow conditions between FLiBe and Dowtherm-A at full scale (1:1 scale) for Pr = 7.95. 93
Table 28. Similarity scaling results between FLiBe and Dowtherm-A at reduced length scale (0.75:1 scale) for Pr = 19.4. 94
Table 29. Requisite flow conditions between FLiBe and Dowtherm-A at reduced length scale (0.75:1 scale) for Pr = 19.4. 95
Table 30. Similarity scaling results between FLiBe and Dowtherm-A at reduced length scale (0.75:1 scale) for Pr = 7.95. 96
Table 31. Requisite flow conditions between FLiBe and Dowtherm-A at reduced length scale (0.75:1 scale) for Pr = 7.95. 97
Table 32. Similarity scaling results between FLiBe and Dowtherm-A at reduced length scale (0.5:1 scale) for Pr = 19.4. 98
Table 33. Requisite flow conditions between FLiBe and Dowtherm-A at reduced length scale (0.5:1 scale) for Pr = 19.4. 99
Table 34. Similarity scaling results between FLiBe and Dowtherm-A at reduced length scale (0.5:1 scale) for Pr = 11.9. 100
Table 35. Requisite flow conditions between FLiBe and Dowtherm-A at reduced length scale (0.5:1 scale) for Pr = 11.9. 101
Table 36. Requisite flow conditions between FLiBe and Dowtherm-A at reduced length scale (0.5:1 scale) for Pr = 9.64. 102
Table 37. Similarity scaling results between FLiBe and Dowtherm-A at reduced length scale (0.5:1 scale) for Pr = 7.95. 103
Table 38. Requisite flow conditions between FLiBe and Dowtherm-A at reduced length scale (0.5:1 scale) for Pr = 7.95. 104

Table 39. Numerical results for FLiBe at Pr = 19.4 with N = 75 pebbles...... 105
Table 40. Numerical results for Dowtherm-A at full length scale (1:1) for Pr = 19.4 with N = 75 pebbles...... 105
Table 41. Numerical results for Dowtherm-A at reduced length scale (0.75:1) for Pr = 19.4 with N = 75 pebbles...... 106
Table 42. Numerical results for Dowtherm-A at reduced length scale (0.5:1) for Pr = 19.4 with N = 75 pebbles...... 106

List of Abbreviations

AEC	Atomic Energy Commission
ANP	Aircraft Nuclear Propulsion
BCC	Body-Centered Cubic
CAD	Computer Aided Design
DEM	Discrete Element Method
DRACS	Direct Reactor Auxiliary Cooling System
FCC	Face-Centered Cubic
FHR	Fluoride Salt-Cooled High-Temperature Reactor
FIMA	Fissions per Initial heavy Metal Atom
GCI	Grid Convergence Index
HTGR	High-Temperature Gas Reactor
H2TS	Hierarchical Two-Tiered Scaling
IET	Integral Effects Test
IPyC	Inner Pyrolytic Carbon
INL	Idaho National Laboratory
LES	Large Eddy Simulation
LOCA	Loss Of Coolant Accident
KP-FHR	Kairos Power-Fluoride Salt-Cooled High-Temperature Reactor
MSR	Molten Salt Reactor
Mk-1	Mark-1
MSRE	Molten Salt Reactor Experiment
NACC	Nuclear Air-Brayton Combined Cycle
NGNP	Next-Generation Nuclear Plant
NRC	Nuclear Regulatory Commission
ORNL	Oak Ridge National Laboratory
PB-FHR	Pebble Bed-Fluoride Salt-Cooled High-Temperature Reactor
PLT	Prism Layer Thickness
PWR	Pressurized Water Reactor
q-DNS	quasi-Direct Numerical Simulation
RANS	Reynolds-Average Navier Stokes
SST	Shear Stress Transport
TRISO	TRi-structural ISOtropic
WALE	Wall-Adapting Local Eddy-Viscosity

List of Symbols

A_{cyl}	Area of the cylindrical domain (mm^2)
A_s	The surface area of a single pebble (mm^2)
C_p	Specific heat capacity (J/kgK)
D_{cyl}	The equivalent diameter of reactor core vessel (mm)
DF	Distortion factor
D_p	Diameter of single pebble (m)
f	Friction factor
h	Investigated mesh size (mm)
H_{add}	Height of extended region beyond pebble region (mm)
h_{avg}	Average heat transfer coefficient (W/m^2K)
H_{cyl}	Active height of the cylindrical domain (not the pebble domain) (mm)
H_p	Height of pebble region (mm)
k_{in}	Thermal conductivity (W/mK)
N	Number of pebbles
Nu	Nusselt number
Pr	Prandtl number
Q_{gen}	Heating power of single pebble (W)
R	Active height to diameter ratio
R_{cyl}	The equivalent radius of reactor core vessel (mm)
Re	Reynolds number
R_ϕ	Relative error of investigated value of interest
T	Temperature (K)
T_{in}	Inlet temperature (K)
$\overline{T_s}$	Average pebble surface temperature (K)
$T_{s,i}$	The surface temperature of pebble i (K)
$\overline{T_\infty}$	Average bulk fluid temperature (K)
$T_{\infty,i}$	The bulk fluid temperature of pebble i (K)
$T_{H0} - T_{C0}$	Temperature difference (K)
u_i	Superficial velocity (m/s)
V_p	The volume of a single pebble (mm^3)
$V_{t,p}$	The total volume of pebbles in the domain (mm^3)
$V_{cyl,p}$	The total volume of the pebble domain (mm^3)
y^+	Non-dimensional wall distance for a wall-bounded flow
δ_p	The minimum gap size between pebbles (mm)
ρ	Density (kg/m^3)
μ	Dynamic viscosity (Pa·s)
ϕ	Investigated value of interest
ΔP	Pressure drop (Pa)
Δs	Required first cell height of mesh near the wall (m)

Subscripts: R, ratio; t, total; m, model; p, prototype.

SIMILARITY SCALING EFFECTS ON THE THERMAL HYDRAULIC BEHAVIOR OF A RANDOMLY PACKED PB-FHR CORE USING SURROGATE FLUID

Thesis Abstract

Idaho State University (2022)

Computational analyses were performed to quantify the inherent Nu scaling distortion caused by similarity scaling between FLiBe and its surrogate fluid Dowtherm-A for a randomly packed pebble bed akin to the MK-1 PB-FHR core. Preliminary studies were conducted to determine the optimum modeling approach, geometrical flow path design, minimum gap size between pebbles, mesh specifications, and the number of required pebbles. Results showed using the realistic approach with artificial spacing between pebbles with δ_p = 0.005 mm, N = 75, and h = 0.5 mm to be sufficient in producing an accurate Nu to the validation data. Using similarity scaling techniques, the requisite flow and heating conditions for various length scales (1:1, 0.75:1, and 0.5:1) using Dowtherm-A were determined. Simulations were performed for FLiBe and Dowtherm-A at the three-length scales for the investigated ranges of 500 < Re < 2500 and 7.95 < Pr < 19.4. The FLiBe numerical results showed similar behavior to the Wakao correlation, which is currently the recommended Nu correlation for PB-FHR cores. The collected data for FLiBe was used to develop a Nu correlation. The resulting correlation, $Nu = 0.633Re^{0.6}Pr^{0.5}$, showed good agreement with the numerical data, producing only $\pm$5% error. The Nu results of the Dowtherm-A data at various length scales displayed similar behavior despite having distinctly different flow and heating conditions between each length scale. The collected Dowtherm-A data was also used to develop a Nu correlation, independent of the length scale. The resulting correlation, $Nu = 0.268Re^{0.6}Pr^{0.745}$, showed good agreement with the numerical data, showing $\pm$10% error. Comparison between the FLiBe and Dowtherm-A data sets showed similar distortion values for all investigated length scales, showing -14% at Pr = 19.4 and -30% at Pr = 7.95 for Dowtherm-A. A Nu distortion correction factor (Ψ) was developed, resulting in $\Psi = 2.362Pr^{-0.245}$. Thus, if Dowtherm-A were to be experimentally investigated for a PB-FHR core with correctly reduced power and flow conditions, the Nu data results can be multiplied by this distortion correction factor to achieve similar results for FLiBe. By implementing the developed Nu distortion correction into the Dowtherm-A data sets, roughly $\pm$2% error at Pr = 19.4 and $\pm$8% error at Pr = 7.95 for the FLiBe numerical data results was observed.

Keywords: pebble bed, fluoride salt, similarity scaling, Nusselt number

Chapter 1: Introduction

The utilization of similarity scaling techniques allows certain reactor core thermal-hydraulic behaviors to be replicated using surrogate fluids. The actual reactor coolant's thermal-hydraulic behavior can be replicated by performing small-scale experiments under reduced temperature, time, size, and power with appropriate surrogate fluids. In a small-scale test facility, utilizing surrogate fluids through similarity scaling can eliminate safety concerns that would be present with the actual reactor coolant. Similarity scaling is accomplished by matching dimensionless numbers pertaining to the desired phenomenon. Matching the necessary dimensionless numbers theoretically produces identical results. However, theoretically-driven quantification of behaviors does not always account for discrepancies caused by similarity scaling, such as randomness and dissimilar thermophysical property changes with temperature between fluids. The difference in an observed behavior between a coolant and its surrogate fluid at theoretically matching conditions, known as the scaling distortion, can be crucial information for justifying the reasoning between incongruities despite being theoretically analogous.

In 2008, several potential surrogate fluids were identified for the molten salt FLiBe, the primary coolant utilized in the Mark-1 Pebble Bed Fluoride Salt-Cooled High-Temperature Reactor, also known as the Mk-1 PB-FHR [1]. The primary candidate for FLiBe was a mineral oil known as Dowtherm-A, which can successfully match the Prandtl number (*Pr*) at various temperatures. As a result, the Nusselt number (*Nu*) can be matched by also matching the Reynolds number (*Re*) between FLiBe and Dowtherm-A.

The Mk-1 PB-FHR is a pre-conceptual reactor design developed to evaluate the usage of an annular pebble-bed core with low-pressure fluoride-based salts. Completed in 2014, the Mk-1 PB-FHR preconceptual design was proven to have high intrinsic safety and more flexible and valuable services than current reactor systems, making it a viable candidate for future commercial reactor technologies. The usage of a pebble bed core was not a new concept at the time, having been studied extensively for gas-cooled reactors, of which some concepts utilized spherical fuel. However, despite the extensive computational research into studying the hydrodynamic and thermal heat transport behavior of such reactors, comparisons of the presently available literature have shown discrepancies between the flow path's geometrical design and simulation strategy. Only by achieving good agreement with experimental data can a given model/setup be officially validated. Unfortunately for pebble bed fluoride salt-cooled high-temperature reactor (PB-FHR)

concepts, the usage of fluoride-based salts in small-scale experimentation is accompanied by many additional safety concerns and experimental limitations. Thus few experimental studies have been pursued at the university level. Fortunately, by substituting surrogate fluids with the correct usage of similarity scaling techniques, the surrogate fluid can theoretically imitate the heat transport phenomena of the fluoride-based salt.

In this chapter, an overview of the technological characteristics and market relevance of the Mk-1 PB-FHR is discussed in detail. This study presents a comparison of potential design methods and simulation strategies to identify an appropriate design and simulation approach. The primary research objectives and the significance of performing such analyses are defined. Limitations and assumptions of the research are also mentioned.

1-1. PB-FHR Technological Characteristics

The PB-FHR is an amalgamation of several advanced Gen IV reactor system components. The design combines the robust coated particle fuel form developed for high-temperature gas-cooled reactors (HTGR), the direct reactor auxiliary cooling system (DRACS) created for liquid-metal fast reactors, and the high volumetric heat capacity liquid-fluoride salts as coolants from molten salt reactor (MSR) concepts. The culmination of coated particle fuel and high-*Pr* molten salt coolants allows the PB-FHR to operate at high temperatures and low pressures, making the PB-FHR an economically viable option.

As energy consumption demands continue to increase with the rising global population, identifying potentially innovative electricity-producing technologies will become imperative to ensure the structural integrity of the world's energy infrastructure. Nuclear energy has been proven to provide reliable base load electricity to consumers with practically zero emissions. Given the intricately designed passive safety system, robust fuel form, and highly convective coolant, the commercialization of PB-FHR technologies has a high probability of coming to fruition in the coming years. The KP-FHR, a PB-FHR concept developed by Kairos Power, is currently undergoing extensive review from the Nuclear Regulatory Commission. Once approved, Kairos Power is set to build the Hermes reactor at Oak Ridge National Laboratory, a low-power demonstration of the PB-FHR concept. This intermediate facility will hopefully validate its capability to deliver low-cost nuclear heat fit to competitively rival the cost of natural gas in the United States' electricity market.

1-2. Mk-1 PB-FHR General Description

The Mk-1 PB-FHR is a pre-conceptual nuclear reactor design developed by the University of California, Berkeley, as part of the U.S. Department of Energy Integrated Research Project collaboration with the Massachusetts Institute of Technology and the University of Wisconsin-Madison. The initial pre-conceptual design was for a small, modular 236 MWth pebble bed reactor that utilizes the nuclear air-Brayton combined cycle (NACC) based on a modified General Electric 7FB gas turbine, enabling peak power production and the ability to provide flexible capacity and several ancillary services to the grid. The Mk-1 PB-FHR was designed to produce a base-load of 100 MWe with a potential increased power output upwards of 242 MWe, accomplished by co-firing natural gas in series with the nuclear-generated power cycle turbine. The majority of the reactor specifications for the Mk-1 PB-FHR were based on the generic FHR concept, which included the utilization of TRISO fuel particles, DRACS, and liquid fluoride-based salt coolant. A flow schematic of the Mk-1 PB-FHR is provided in Figure 1.

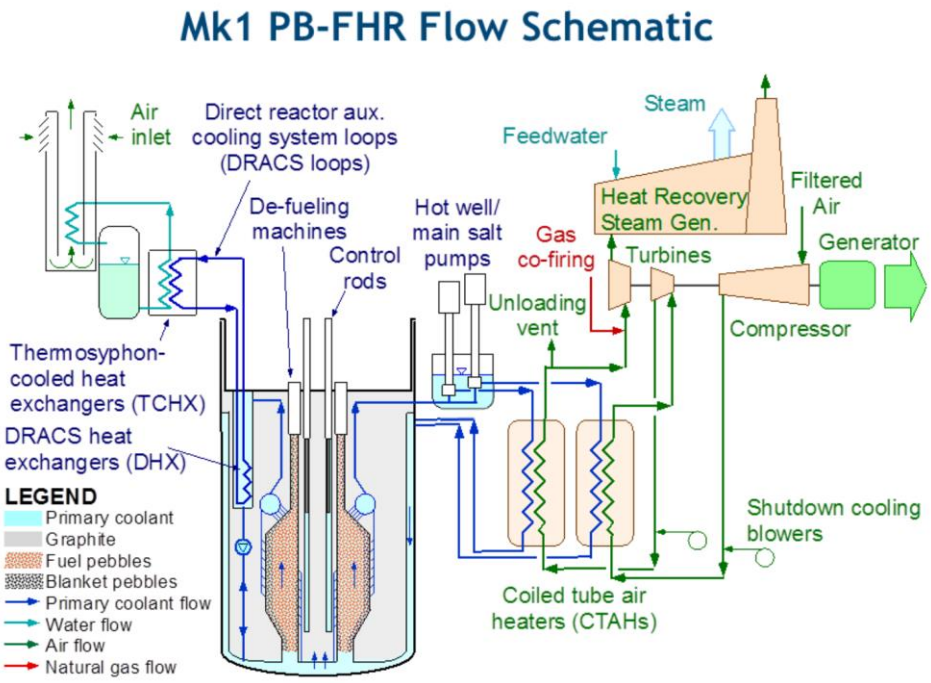

Figure 1. Diagram detailing the main salt loop, DRACS loops, and NACC power conversion system.

Under normal operating conditions, the core inlet and bulk-average outlet temperatures reported for the Mk-1 PB-FHR were 600°C and 700°C, respectively. The reactor system operates at near atmospheric pressures. The primary coolant volumetric flow rate at 100% power was

around 0.52-0.54 m^3/s. The peak power density was 80 W/cm^3, and the average power density was 20 W/cm^3. The power conversion efficiency using the NACC is 42.4%, which is much higher when compared with standard pressurized water reactor (PWR) designs, being only about 33% efficient.

1.2.1. TRISO Particle Fuel

The acronym for 'TRISO' stands for TRi-structural ISOtropic particle fuel, a type of micro fuel particle that is fabricated into cylindrical pellets, annular compacts, plates, and billiard ball-sized spheres called "pebbles." The robust microencapsulated fuel form was initially developed for use in HTGRs in the 1960s and gained popularity throughout the years, with many of the Gen IV reactor designs utilizing this fuel form, including the Mk-1 PB-FHR. According to the Nuclear Regulatory Commission [2], the contemporary goal of coated particle fuel and the associated fuel form is to (1) Allow the reactor to operate at extremely high-temperature conditions with very high fractional fuel particle integrity during normal operations and accident scenarios as well as very low fission product release during normal operation and under accident conditions, and (2) Possess high fuel burnup (>10% FIMA for pebble bed and >20% FIMA for prismatic core) to allow economical operation of the reactor system and good fissile material utilization. The TRISO fuel particle can survive operating temperatures upward of 1200°C and accident conditions up to 1800°C.

A single TRISO fuel particle size is roughly 1-mm, with a fuel kernel diameter of 0.5-mm. The typical TRISO fuel kernel is composed of either uranium dioxide (UO_2) or a two-phase mixture of UO_2 and uranium carbide (UC_2), known as uranium oxycarbide (UCO). Fuel kernels made using thorium and plutonium are also possible but do not possess burnup rates as high as the UO_2 or UCO kernels, which ultimately lowers the peak power potential of the reactor system. The UO_2 kernel was the first fuel kernel proposed due to its extensive research, but the fission reactions from UO_2 produced large amounts of carbon monoxide, causing a pressure buildup in the TRISO particle. On the other hand, the UCO kernel produces small amounts of carbon monoxide, so for higher operating temperatures and higher burnup rates seen in many Gen IV reactors, the UCO fuel kernel is more commonly used. The uranium composition of TRISO fuel can be upwards of 20% 235U.

The fuel kernel is encased in several structural layers – porous graphite buffer layer, inner pyrolytic carbon layer, silicon carbide layer, and outer pyrolytic carbon layer – forming a pressure

vessel around the kernel to prevent the release of fission gases into the reactor. The porous graphite buffer layer provides additional space for the released gases to collect, originating from fission reactions and chemical reactions between the carbon buffer layer and oxygen release from the UO_2 or UCO fuel kernel. The inner Pyrolytic Carbon layer (IPyC) is overlaid on the porous graphite layer to provide a smooth surface for the silicon carbide to bind to, acting as a shield for the fuel kernel from the chlorine released during fabrication and providing structural integrity. The silicon carbide (SiC) layer is applied as the major fission product barrier to prevent the fission gas from releasing into the coolant. The outer pyrocarbon layer compresses the SiC layer, providing a compressive pressure to contain the internally generated pressures and offer protection from high temperatures and pressures externally generated in the reactor vessel from other TRISO fuel matrices. The TRISO fuel particle design implemented in the Mk-1 PB-FHR was based on design studies for a 290-MWth core and scaled down to a 236-MWth core. The TRISO fuel particle design details are summarized in Table 1 and visualized in Figure 2.

Table 1. Mk-1 PB-FHR TRISO fuel particle design [3].

Parameter	Value
Fuel kernel diameter (μm)	400
Fuel kernel density (kg/m3)	10500
Fuel kernel composition	$UC_{1.5}O_{0.5}$
Buffer layer thickness (μm)	100
PyC inner layer thickness (μm)	35
SiC layer thickness (μm)	35
PyC outer layer thickness (μm)	35

Typically, the distribution of TRISO particles is layered throughout the pebble, as shown in Figure 3a. In the Mk-1 PB-FHR design, the TRISO fuel particles are situated in an annular fuel-particle-embedded graphite matrix, which sits between low-density core and high-density graphite coating, as shown in Figure 3b.

The annular fuel zone contains roughly 4730 coated TRISO particles containing around 1.5 g of 19.9% enriched uranium. According to the Technical Report of the Mk-1 PB-FHR, the usage of the PB-FHR fuel annulus in the pebble design allows for a lower average and peak temperature than the pebbles used in gas-cooled pebble bed reactors. The dimensions of the Mk-1 PB-FHR pebble are summarized in Table 2.

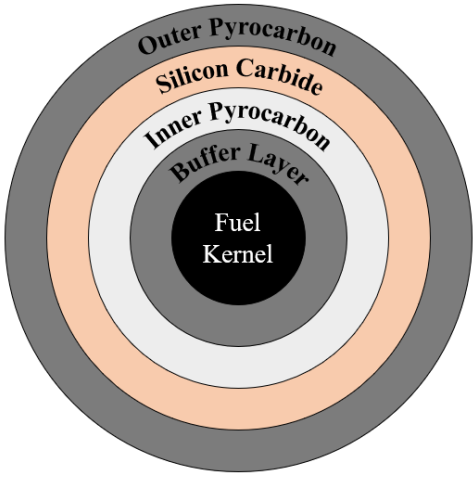

Figure 2. Layers of general TRISO fuel particle utilized in several pebble bed reactors.

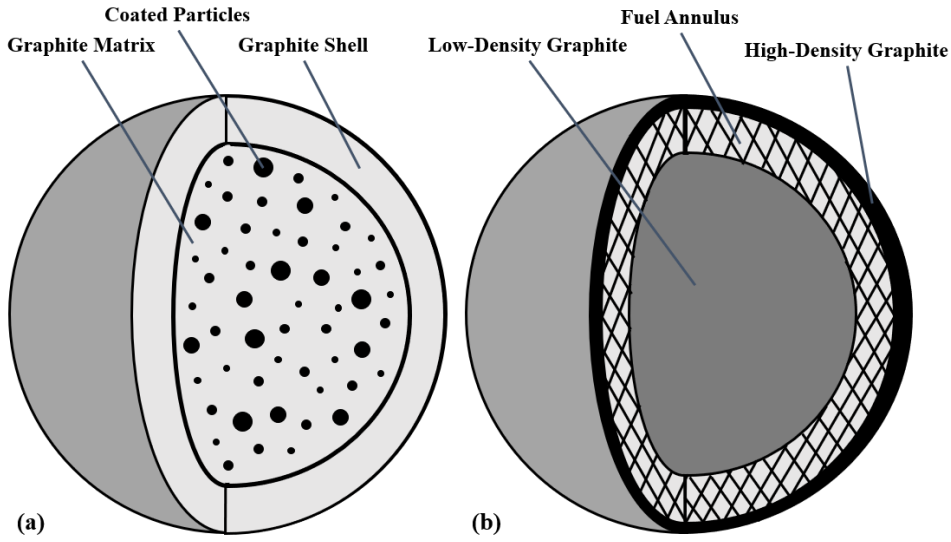

Figure 3. (a) Cross-section of pebble typically used in gas-cooled pebble bed reactors; (b) Cross-section of pebble used for the Mk-1 PB-FHR.

Table 2. Geometrical specifications of Mk-1 PB-FHR fuel (Technical description).

Parameter	Value (mm)
Pebble diameter (D_p)	30
Low-density graphite core	25
Fuel annulus	4
High-density graphite coating	1

1.2.2. Direct Reactor Auxiliary Cooling System

The direct reactor auxiliary cooling system (DRACS) is a passive residual heat removal system that features three natural circulation/convection loops that rely on buoyancy as the driving

force. During accident scenarios such as loss of coolant accidents (LOCA), the fluidic diode minimizing the parasitic flow into the DRACS primary loop activates in response to reactor shutdown measures, initiating heat transfer between the primary DRACS loop and a secondary natural circulation salt loop. The secondary natural circulation salt loop transports the heat to an external heat sink cooled by atmospheric air. Utilizing DRACS allows any excess heat to be removed passively, acting as an additional safety measure.

1.2.3. Liquid Fluoride Salt Coolants

Fluoride salts have been extensively researched as potentially viable coolants in PB-FHR technologies. According to the Technical Description of the Mk-1 PB-FHR [4], fluoride salts have been proven to have uniquely high volumetric heat capacity, low chemical reactivity with air and water, very low volatility at high temperature, effective natural circulation heat transfer, and high retention of most fission products. The liquid fluoride salt coolants FLiBe (^{7}LiF and BeF_2), which theoretically contains the lowest possible parasitic neutron capture, has become the prime candidate for potential PB-FHR coolants.

1-3. Literature Review

Most research on pebble bed reactors was accomplished using symmetric face-centered cubic (FCC) lattice structures. This approach, which has a homogenous core with equal spacing, does not accurately reflect the reality of an actual pebble bed core, of which all pebbles are randomly packed. The inherent randomness of the pebble bed geometric flow path causes a significant change in the hydrodynamic and thermal behavior compared to an FCC-lattice structure. By comparing an FCC lattice structure with an actual packed bed, drastic differences were observed in both the heat transfer and pressure drop [5]. Comparison between FCC and BCC lattice structures discovered that the two configurations have significant variations in *Nu* [6]. Investigations of the flow behavior around an FCC configuration showed that eddies were created and destroyed quickly between pebbles due to the symmetry of the test section [7]. Studies of the flow vorticity in FCC pebble bed lattices showed that a symmetric pebble bed lattice would cause recirculation flow, creating stagnation locations in the upper and lower regions of the pebbles and subsequently inducing local hot spots at those locations [8]. By making the position of each pebble in the reactor core random, the intersecting flow and hot spot locations are random, and the heat transfer distribution is unevenly distributed in the core, which is more representative of an actual

PB-FHR core, where each pebble location consistently changes as each pebble is cycled out. Randomly packed pebbles can be generated using a random point generator with a specified radial distance between surrounding points [9]. Pebble locations formed from the discrete element method (DEM) after the dynamic settling of pebbles can also be used to define the cartesian coordinates of each pebble's center in a domain [10].

Depending on the desired physical phenomena, specific simulation strategies are necessary. When modeling a pebble bed core, which can be considered a porous media, there are essentially two approaches: the porous media and the realistic approach. The porous media approach uses an averaged concept of porosity to create the flow domain, incorporating an empirically determined flow resistance in the porous region. The realistic approach accounts for each surface, treating each pebble as a separate entity that can be post-processed individually. Investigations into comparing a porous media and realistic approach revealed that the porous media approach could be used to capture thermal-hydraulic parameters such as bulk fluid temperature increases and averaged pressure drop (ΔP) quickly and reasonably. However, the porous media approach could not accurately capture temperature variations around the pebble surface, vortices, flow separation in the pores, and variations of *Nu* at azimuth and zenith angles [11]. The conclusion for the investigation showed that the porous media approach can capture volume-averaged global characteristics of the flow behavior but cannot accurately capture the local heat transfer phenomena necessary to quantify the *Nu* and is thus inferior to performing the realistic approach, where each pebble is individually modeled, meshed, and simulated. The porous media approach was applied to a PB-FHR core using FLiBe as the coolant, coming to the same conclusion that the porous model can only obtain averaged thermal-hydraulic characteristics and cannot accurately predict detailed local flow and heat transfer phenomena [12].

By using the realistic approach, the backflow and secondary-flow phenomena can be captured. However, this means that each surface must be individually meshed, which creates two significant problems: (1) Discretizing a mesh down to a reasonable size to capture the thermal-hydraulic behavior of an entire reactor core is impossible, and (2) The treatment of the inter-pebble region must be modeled. Regarding the impracticability of modeling an entire PB-FHR core using the realistic approach, studies have shown that if you were to take a segment out of the reactor core and only model a particular portion of the reactor, the *Nu* could be roughly matched to the actual behavior of the reactor core during normal operation [9]. Concerning the modeling of the inter-

pebble region, ideally, the gap size between pebbles that are supposed to touch should be zero, but this is unfortunately difficult to accomplish computationally due to commercial CAD tools not allowing zero-spacing between pebbles. Investigations of the mesh generation complication of near-contact points concluded that it is numerically impossible to simulate a point-contact between pebbles and that alternatives must be discovered [13, 14]. Two pebbles touching with zero separation were generated using the CFX-5 Build module [7]. Still, to accomplish this, a common point on the vertices of the plane perpendicular must be manually situated, which is practically impossible when dealing with several pebbles in a 3D space. Alternative methods to modeling the inter-pebble region have been proposed, detailing their comparison to zero-separation core analyses from experimental efforts. The two main categories for modeling the inter-pebble region are the no-contact and contact zone methods. The no-contact zone has two methods: the gap method and the cap method, and the contact zone method also has two methods, namely the overlap method and the bridge method.

The gap method creates an artificial spacing between each pebble, seeking to minimize the gap size between pebbles while still allowing meshing to occur. Some studies on the gap method reduced the size of the pebbles to achieve a gap [15], while others maintained the originally intended diameter of the sphere and introduced an artificial gap [9, 16-18]. Figure 4 details the difference between manually positioning the pebbles versus reducing the size of the pebble slightly to create the gap between pebbles. The cap method, as shown in Figure 5, flattens the sphere surface perpendicular to each adjacent pebble [17, 19]. The tiny gaps produced using either of these two methods will, in turn, cause jetting flow between each pebble. The high-velocity flow at these locations consequently affects the pebbles' surface temperature distribution, ultimately affecting the heat transfer performance at those locations.

The overlap method, as shown in Figure 6a, creates a contact zone between each adjacent pebble, allowing for each sphere to overlap one another [5, 17-18, 20-21]. The bridge method, as shown in Figure 6b, creates cylindrical bridges at near-contact points between adjacent pebbles [18, 22]. The overlap and bridge method produce similar phenomena, where the local flow around the contact zones become stagnant. The stagnant flow around these zones results in an increased chance of hot spots at near-pebble regions, affecting the heat transfer significantly.

Out of all the methods proposed, the gap method has been proven by the literature to have a minor effect on the heat transfer behavior compared to alternative methods, thus making it the

primary choice in modeling a randomly packed pebble bed. The method of not reducing the size of each pebble and creating an artificial space between each pebble is used in this study.

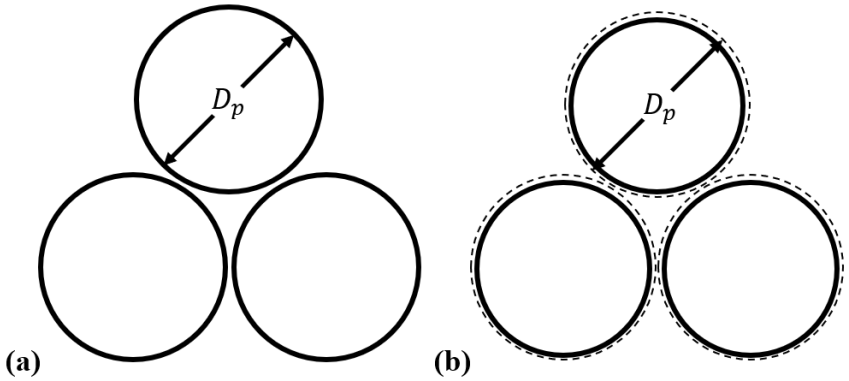

Figure 4. (a) Gap method by introducing an artificial gap between each pebble; (b) Gap method by slightly reducing the diameter of each sphere. The dashed lines represent the original size of each sphere.

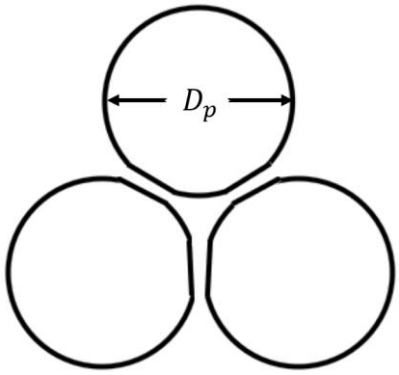

Figure 5. Cap method, which flattens the surface perpendicular to each adjacent pebble.

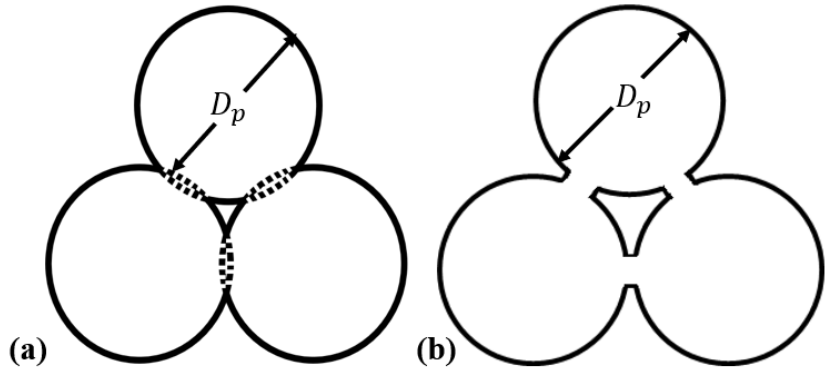

Figure 6. (a) Overlap method creates a contact zone between each adjacent pebble. The dashed lines represent the overlap region between pebbles; (b) the bridge creates cylindrical bridges at near-contact points between adjacent pebbles.

1-4. Research Objectives

The Mk-1 PB-FHR coolant FLiBe is simulated at varying Re and Pr in a cylinder filled with randomly-packed, isotropic spheres comparable to the established Mk-1 PB-FHR design specifications to quantify the average Nu. The reactor core is reduced geometrically using similarity scaling techniques at specific length scales. The appropriate thermophysical properties and boundary conditions that theoretically reproduce identical Re and Pr are determined for the surrogate fluid Dowtherm-A. Simulations are performed for the same Re and Pr using the surrogate fluid at various length scales to quantify the Nu. Comparisons are made between the collected FLiBe data set and the Dowtherm-A data sets at various length scales, and appropriate correlations are developed along with a scaling distortion correction factor for Dowtherm-A.

The subject matter of this thesis can be categorized into four main objectives:

1. Benchmarking Analysis – Results for the average heat transfer coefficient in a randomly packed pebble bed using FLiBe were reported for a single Re and Pr at steady-state for various numbers of pebbles. The average convective heat transfer coefficients at varying numbers of pebbles were compared and validated to q-DNS validated LES data sets. Using the same geometrical and mesh specifications, thermophysical properties, and flow/heating conditions, these same cases are repeated to verify the suitability of their chosen turbulence model. This justifies this study's chosen turbulence model.
2. Parametric Study of Mesh and Gap Size – The effects of the minimum gap size between pebbles (δ_p) and mesh specifications on the heat transfer and pressure drop are analyzed simultaneously to determine an appropriate δ_p and mesh specifications to be used in all simulation work. The effect of the number of pebbles (N) is revisited after concluding on the appropriate δ_p and mesh specifications.
3. FLiBe Case Study – Using the concluded N, δ_p and mesh specifications, flowing FLiBe is simulated for $500 < Re < 2500$ and $7.96 < Pr < 19.4$ to evaluate the effects of Pr on Nu and ΔP. A Nu correlation is developed for flowing FLiBe in a randomly packed pebble bed for the aforementioned Re and Pr ranges.
4. Similarity Scaling Study – The thermophysical properties of Dowtherm-A are calibrated to match the Pr simulated using FLiBe identically. The reactor core is reduced geometrically at specific length scales, altering the flow and heating conditions to match Re simulated for

FLiBe. The flow and heating conditions are identified using similarity scaling techniques for each length scale. The same Re and Pr ranges conducted for FLiBe are simulated for each length scale using Dowtherm-A. The effects of Pr on Nu and ΔP are quantified for Dowtherm-A. A Nu correlation is developed for Dowtherm-A in a randomly packed bed for the same Re and Pr ranges as the FLiBe cases. The FLiBe and Dowtherm-A cases at various reduced length scales are compared and analyzed. A Nu distortion correction factor is developed using the developed Nu correlations for both FLiBe and Dowtherm-A.

1-5. Significance of Study

The pre-conceptual design of the Mk-1 PB-FHR has been adopted into the commercial reactor design developed by Kairos Power, known as the KP-FHR, which is in the latter stages of NRC licensing review. The land has already been purchased at Oak Ridge National Laboratory (ORNL) for large-scale prototype construction of the Hermes reactor, the KP-FHR intermediate test facility. The KP-FHR pebble bed core was designed and optimized using trial-and-error methods, so accurately quantifying the pebble bed core without building intermediate experimental facilities can potentially cut costs significantly. Quantifying the thermal and hydrodynamic behavior of the surrogate fluid, Dowtherm-A provides essential information about the scaling distortion with regards to FLiBe at theoretically identical conditions, justifying the discrepancies in the heat transfer performance if a small-scale experiment of this setup was conducted. The research presented in this thesis provides a solid foundation for building up a small-scale experiment, which can be used for validation purposes.

1-6. Assumptions/Limitations/Delimitations

Thermal radiation depends on wavelength, temperature, and chemical composition, making it a complex phenomenon to simulate computationally. The molten salt FLiBe is considered a simple halide salt with no chromophores present to provide color, thus making FLiBe a highly transparent fluid. The transparency of FLiBe does not imply that the thermal radiation is negligible, but unfortunately, there is little to no data and modeling for the effects of infrared absorption on fluoride salts. During the MSR program, measurements of liquid salts were performed at Oak Ridge National Laboratory but were never reported. A few experiments were conducted to determine fluoride salts' radiative heat transfer effects. An experiment on the heat transfer of turbulent FLiBe in a 2-cm-diameter tube with a surface emissivity of 1 determined the

radiative heat flux to be <2% of the convective heat transfer [23]. Another experiment was performed for laminar flow in an NGNP intermediate heat exchanger, which found the net radiative heat flux to be about 40% of the convective heat transfer. In general, radiation heat transfer cannot be ignored for laminar flow but can be ignored for turbulent flow. However, each situation must be evaluated to determine whether radiative heat transfer contributes significantly to the thermal-hydraulic behavior.

Surrogate fluids in scaled experiments typically match *Re* and *Pr* at lower temperatures than their respective coolant. The heating mechanism used to provide a constant or alternating heat source is usually electrical, which provides little to no thermal radiative heat transfer. The thermal radiative heat transfer occurring in the primary coolant loop of molten salt reactors has a potentially significant effect on heat transport. When necessary, corrections accounting for the thermal radiation effects must be applied to low-temperature surrogate fluids' flow/heating conditions. Future work is needed to account for the thermal radiative heat transfer effects in molten salt reactors. The analyses performed using FLiBe in this thesis only account for its convective heat transfer behavior and not its thermal radiative heat transfer nor conductive abilities. Potential future work can investigate correction factors to better represent the combination of heat transfer types in PB-FHRs.

Chapter 2: Numerical Methodology

The numerical methodology used to quantify the Nu and ΔP of flowing FLiBe and a surrogate fluid Dowtherm-A in a randomly packed pebble bed is presented here. The necessary fluid flow and heat transfer equations necessary to quantify the Nu and ΔP in packed beds are detailed. The conservation equations are explained along with the finite volume methodology implemented in this study. The generation of the geometrical flow path is described. The mesh generation techniques are briefly discussed, along with the relative and GCI methods for quantifying the discretization error for mesh sensitivity analyses.

2-1. Fluid Flow in Packed Beds

The fluid flow behavior inside a pebble bed reactor is defined by the Reynolds number (Re), the ratio of inertial forces to viscous forces. For internal flow, the characteristic length used in the Re calculation is usually defined as the hydraulic diameter of the container's cross-section. However, for pebble bed flow, the characteristic length is defined differently. The Re for a pebble bed reactor has been widely defined as:

$$Re = \frac{\rho_i u_i D_p}{\mu_i} \tag{1}$$

where ρ_i (kg/m^3) and μ_i (kg/m·s) are the density and dynamic viscosity of the coolant, respectively, evaluated at the inlet temperature of the reactor core, u_i (m/s) is the superficial fluid velocity, which is the flow velocity calculated based on an empty column, and D_p (m) is the diameter of a single pebble in the test section, assuming that all spheres are isotropic [24].

The Re range of the Mk-1 PB-FHR occurs in the laminar and transitional flow regime under forced circulation as defined in Eq. 1. The average Re is around 500. For smooth straight pipes, the transition between laminar and turbulent flow occurs at $Re \approx 2300$, but when dealing with flow that has several obstructions between the inlet and outlet, the Re range for the laminar and turbulent regimes are different. Dissimilar geometric flow paths such as porous media and pebble beds fit this description. The maximum Re reported for the Mk-1 PB-FHR for the purely laminar regime is Re = 952, assuming pure axial flow in the bed even though there would still be some cross-flow [4]. The supposed pure laminar flow value of Re = 952 does not, however, correlate to the absolute possible maximum Re in the reactor. Though the maximum Re for the purely laminar flow in a pebble bed is around Re = 952, this does not imply that no turbulence is

occurring below this number. At locations between two or more pebbles, transition to turbulent flow occurs due to the increased pressure causing constricting flow between pebbles. It is thus imperative to choose a turbulence model when modeling a pebble bed test section.

2-2. Heat Transfer in Packed Beds

The convective heat transfer performance is defined by the Nusselt number (Nu), which is the ratio of convective to conductive heat transfer across a boundary. Similar to the Re definition for pebble beds, the Nu is defined as:

$$Nu = \frac{h_{avg} D_p}{k_i} \tag{2}$$

where h_{avg} (W/m^{2}K) is the average heat transfer coefficient, D_p (m) is the diameter of a single pebble, and k_i (W/m·K) is the thermal conductivity evaluated at the inlet temperature conditions. Assuming the walls to be adiabatic and fully insulated and the heating power of each pebble to be uniform, the convective heat transfer coefficient can be calculated using the convective heat transfer equation, rearranged as:

$$h_{avg} = \frac{Q_{gen}}{A_s(\overline{T_s} - \overline{T_\infty})} \tag{3}$$

where Q_{gen} (W) is the heating power of a single pebble, A_s (m^2) is the surface area of a single pebble, $\overline{T_s}$ (K) is the average pebble surface temperature of all pebbles, and $\overline{T_\infty}$ (K) is the average bulk fluid temperature.

The average pebble surface temperature $\overline{T_s}$ is calculated by adding the average surface temperature of each pebble and dividing it by the total number of pebbles:

$$\overline{T_s} = \frac{1}{N}\sum_{i=1}^{N} T_{s,i} \tag{4}$$

The average bulk fluid temperature $\overline{T_\infty}$ is calculated by adding the average bulk fluid temperatures evaluated at the height of the center point of each pebble and dividing it by the total number of pebbles:

$$\overline{T_\infty} = \frac{1}{N}\sum_{i=1}^{N} T_{\infty,i} \tag{5}$$

Due to the adiabatic wall boundary and applied no-slip conditions, the flow velocity and heat flux is expected to be lower in the region closer to the wall. To eliminate the effects of near-

wall behavior, the observed bulk temperature section for each pebble ($T_{\infty,i}$) is reduced by two times the pebble radius, as shown in Figure 7.

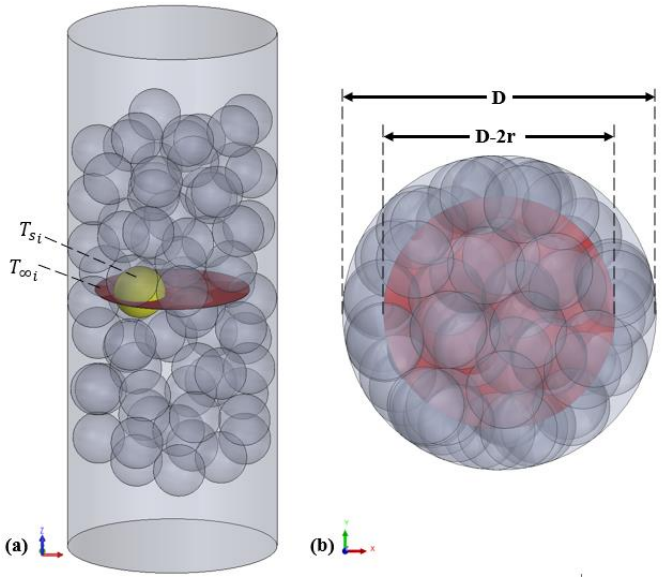

Figure 7. The analyzed bulk temperature section was reduced by two times the pebble radius to avoid near-wall effects.

By reducing the post-processing domain by two times the pebble radius in both the axial and radial direction, the void fraction is theoretically reduced to around 0.4 [9], the Mk-1 PB-FHR core void fraction value. The post-processing domain for calculated Nu is visualized in Figure 8.

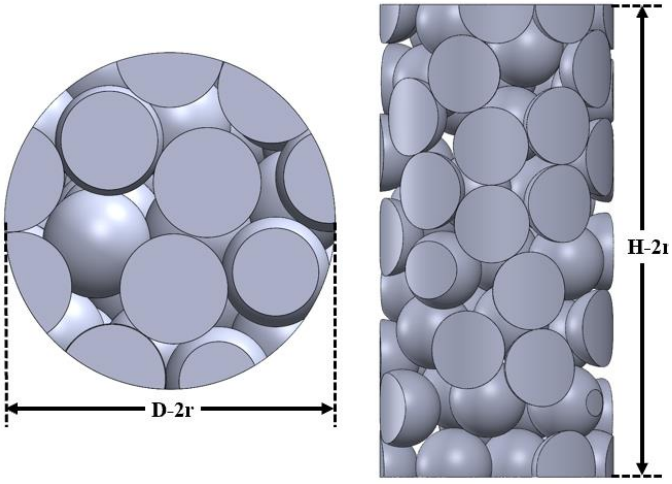

Figure 8. Reducing the post-processing domain reduces the void fraction and eliminates the wall effect. The reduced void fraction is akin to the Mk-1 PB-FHR core porosity.

2-3. Conservation Equations

In CFD analyses, three fundamental physical principles must be conserved to model fluid dynamics and heat transfer phenomena correctly. These are the continuity, momentum, and energy conservation equations. These equations can appear in various forms depending on the phenomena of interest attempted to be modeled. The conservation equations and their derivation form for incompressible flow without change in thermophysical properties with temperature are presented here, though, in reality, the thermophysical properties change as a function of temperature.

2.3.1. Continuity (Mass) Equation

The continuity equation follows the universal rule that matter cannot be created nor destroyed. The form of the continuity equation typically follows the conservation of mass law. If a fluid is passing through an infinitesimal, fixed control volume, then the continuity equation can be written as:

$$\frac{\partial \rho}{\partial t} + \boldsymbol{\nabla} \cdot (\rho \boldsymbol{V}) = 0 \tag{6}$$

where ρ is the fluid density and $\boldsymbol{V}$ is the fluid velocity vector field. The first term represents the change in density in the control volume, and the second represents the change in mass flux passing into and out of the control surface. By rearranging Eq. 6 to be in the substantial derivative form, the continuity equation can be written as:

$$\frac{D\rho}{Dt} + \rho(\boldsymbol{\nabla} \cdot \boldsymbol{V}) = 0 \tag{7}$$

If the fluid is incompressible, as what is observed in the Mk-1 PB-FHR core, the first term in Eq. 8 can be set to zero, which simplifies the continuity equation down to the following equation:

$$\boldsymbol{\nabla} \cdot \boldsymbol{V} = 0 \tag{8}$$

2.3.2. Momentum Equation

The conservation of momentum equation is ultimately derived from Newton's second law, which states that the rate of change of momentum of a body over time is directly proportional to the force applied. For fluid dynamics, the momentum in a system is conserved by using the Navier-Stokes equation. If the dynamic viscosity (μ) is constant and the desired flow is incompressible, the Navier-Stokes equation can be defined as:

$$\rho \frac{D\boldsymbol{V}}{Dt} = \rho \boldsymbol{f} - \boldsymbol{\nabla} p + \mu \nabla^2 \boldsymbol{V} \tag{9}$$

where $\rho \frac{DV}{Dt}$ represents the combination of the rate of increase of momentum per unit volume in the control volume and the rate of momentum lost by convection per unit volume through the control surface. The term $\rho \boldsymbol{f}$ represents the body forces per unit volume, which typically only includes the gravitational force. The variable $\boldsymbol{f}$, can generally be replaced with the acceleration of the gravity vector $\boldsymbol{g}$. The term $-\boldsymbol{\nabla} p$ represents the pressure gradient. The term $\mu \nabla^2 \boldsymbol{V}$ represents the viscous stress tensor term. The Navier-Stokes equation can be divided into three scalar equations for each Cartesian direction [25]. The Navier-Stokes equation refers to the components of the viscous momentum equation, but often all three equations (continuity, momentum, and energy) are referred to as the Navier-Stokes equations.

2.3.3. Energy Equation

The conservation of energy equation comes from the first law of thermodynamics, which states that the total energy of an isolated system is constant; that energy cannot be created nor destroyed, but only transformed from one form to another. For an incompressible fluid with constant thermal conductivity, the energy equation for fluid dynamics can be defined as:

$$\rho \frac{De}{Dt} = \frac{\partial Q}{\partial t} + k \nabla^2 T + \Phi \tag{10}$$

where $\rho \frac{De}{Dt}$ represents the change in internal energy per unit mass per unit volume, $\frac{\partial Q}{\partial t}$ is the rate of heat produced per unit volume by external sources, $k \nabla^2 T$ is the gradient rate of heat lost per unit volume by conduction through the control surface. The term Φ is the dissipation function, representing the expended mechanical energy rate from the fluid's deformation process due to viscosity changes.

2-4. Finite Volume Methodology

The finite volume method is the most common technique utilized for modeling flow. Ultimately, the finite volume method is a technique for representing and evaluating partial differential equations in the form of algebraic equations. The conservation equations (continuity, momentum, and energy) are applied to a fixed space known as the control volume for fluid mechanics and heat transfer, as shown in Figure 9. Using the divergence theorem, the conservation equations are discretized to surface integrals, which can be evaluated as fluxes at the surface of each control volume.

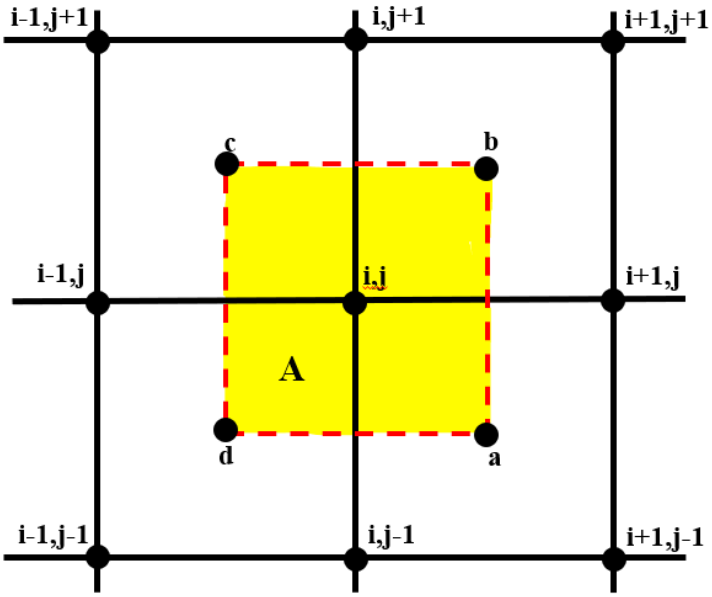

Figure 9. Example of node locations for the finite volume method. An example of a control volume is highlighted in yellow.

The points in Figure 9 represent the control volumes' boundaries, which for quadrilateral meshes are typically placed approximately halfway between actual nodes. The dashed lines and highlighted section represent the surface of a control volume.

There are several advantages of using the finite volume method over the finite difference and finite element methods. One notable advantage is that the mesh grid is not structured to line up all nodes. The finite volume method can solve meshes of complex geometric flow paths without being restricted due to rigid connectivity and node alignment. Thus, control volumes for tetrahedral and polyhedral meshes can solve the conservation equations.

Another advantage is that the finite volume method uses cell-averaged values, which enforces the conservation of quantities at discretized levels. Since each control volume surface in a grid is adjacent to at least one other control volume surface, the fluxes are directly balanced, and thus conservation discretization is automatically obtained through integral conservation laws. For this study, due to the complexity of randomly packed pebbles, the finite volume method is utilized to determine Nu and ΔP.

2-5. Geometrical Flow Path Design

The flow path generation for a randomly packed pebble bed was accomplished in two steps. The first step was to determine the cartesian coordinates of every single pebble in a cylindrical

domain. The cartesian coordinates were identified using an in-house MATLAB code. Once the locations of each pebble were known, the second step was to utilize CAD software to generate the actual flow path.

2.5.1. MATLAB Code

The cartesian coordinates of each pebble in the core test section were derived using an in-house MATLAB code, which can derive the center points of a specified number of spheres in a specified volume. Initially, the core was developed to generate the random distribution of TRISO particles in a single sphere. The core has since been updated to calculate random pebbles in a cube or cylinder. The container shape, which for this study is a cylinder, can be specified along with its volume radius and height. Several vital aspects are required to be specified, including the particle diameter, which for this case is the size of a single pebble, the minimum gap size between particles which forces a minimum artificial gap size to be created without reducing the size of each pebble, and the number of pebbles in the domain. The cartesian coordinates of each pebble are generated using the following steps, as shown in Figure 10:

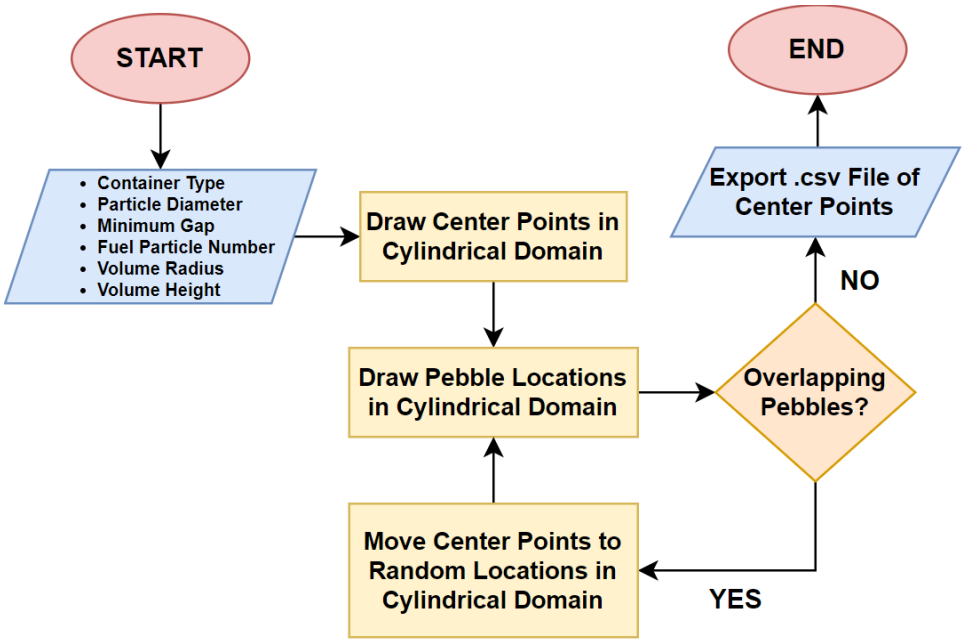

Figure 10. Flow chart of the iterative process in determining the center points of a specified number of spheres in a cylindrical domain.

The center points of individual pebbles are randomly generated in the cylindrical domain by first drawing random center points. Each pebble's volumetric space is theoretically derived in

cartesian coordinates, followed by a logic statement identifying pebbles that overlap each other. The pebbles which intersect one another are moved to new locations, and the process is repeated until no spheres are overlapping [26]. A ".csv" file indicating the center points of each pebble is outputted along with a picture showing the overall geometry once each pebble is drawn, as shown in Figure 11. Using the finalized center points of each pebble from the ".csv" file, the geometric flow path is created using CAD software.

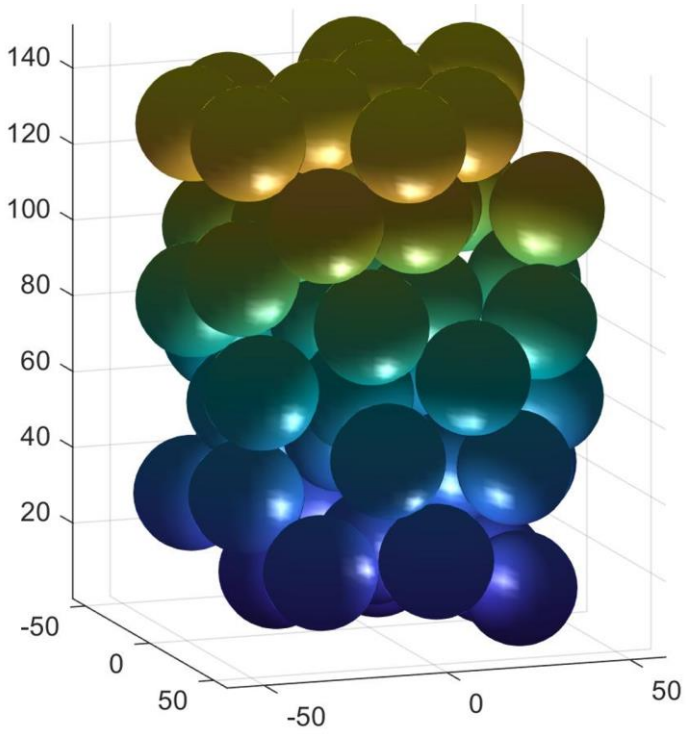

Figure 11. Figure outputted from MATLAB code shows pebbles' location once each sphere is modeled. The figure shows 50 pebbles with a 0.01-mm minimum gap size between pebbles.

2.5.2. Geometric Flow Path Generation

The CAD software SolidWorks 2020 was utilized to generate the geometric flow path domain. A 3D sketch was started, and each point from the ".csv" file was drawn manually, specifying its cartesian location. Each point drawn was fixed. On the front plane, a sphere with the specified radius of a single pebble from the Mk-1 PB-FHR (D_p = 30-mm) was drawn. Using a sketch-driven pattern operation, the sphere was repeated for all pebbles, and the pebble on the front plane was hidden. A custom plane was generated in the MATLAB code at a z-location of half the specified volume height. A circle was then drawn on the custom plane with the specified radius

used in the MATLAB code for the cylinder dimensions. The circle was then extruded beyond the pebble domain to satisfy the active height to diameter ratio ($R = H_{cyl}/D_{cyl} = 1.69$), where H_{cyl} is the active height of the cylindrical domain (not the pebble domain) and D_{cyl} is the equivalent diameter of the Mk-1 PB-FHR core [9]. The extrusion of the cylindrical domain is not merged with the modeled pebbles. Using a Boolean operation, the pebbles in the domain were subtracted from the cylindrical domain, resulting in the desired geometrical flow path.

2-6. Mesh Generation

Due to the complexity of the flow domain, polyhedral mesh elements were used in this study. Each polyhedral element contains several additional neighboring nodes compared with other elements, allowing for thoroughly accurate gradients' approximations. The stretching of each polyhedral element has less impact on the mesh quality than for tetrahedral elements, allowing for the model to be more numerically stable. Polyhedral meshing contains approximately five times fewer cells than a tetrahedral mesh but requires no more surface preparation than the tetrahedral mesh. Polyhedral meshes are generated using a tetrahedral mesh and a dualization scheme that marks the center of each tetrahedral cell and the midpoint of each boundary edge. Starting from boundary edges, the midpoints of each boundary edge, corner points, and midpoints of each tetrahedral cell are connected, and the tetrahedral cell nodes are removed. This process is repeated until all tetrahedral cell nodes are removed completely. The new connections from the midpoints and corner points are the polyhedral mesh.

2.6.1. y+ Boundary Layer Theory

When coupling fluid mechanics and heat transfer in computational analyses, it becomes crucial to ensure that hydrodynamic and thermal boundary layers are captured by the mesh so that all effects, including heat transfer, are captured. FLiBe and its surrogate fluid Dowtherm-A are high-Pr fluids, meaning the thermal boundary layer is very close to the wall, which for this study would be each pebble's surface. Since the superficial velocity only accounts for an empty column or pipe, it would appear that the investigative Re range for this analysis ($500 < Re < 2500$) occurs in the laminar regime. However, the heat transfer occurring near each pebble surface is enhanced due to the accelerating fluid motion, which can cause localized turbulence.

To ensure that the generated mesh for this analysis is sufficient enough to capture the heat transfer phenomenon near the wall, a dimensionless quantity known as y^+ is calculated. The formal

definition of $y^+$is a non-dimensional wall distance for a wall-bounded flow. This value can be used to calculate the first cell height of the mesh near the wall (Δs). The ideal value for $y^+$when using a near-wall model approach should be $y^+ < 1$, but certain low-Re turbulence models considering enhanced wall treatment only require a $y^+ < 5$, since the velocity profiles are assumed to be laminar and viscous stress dominates the wall shear.

The y^+can be determined using the following relationship:

$$y^+ = \frac{u_\tau \, \Delta s \, \rho}{\mu} \tag{11}$$

which can be rearranged to solve for Δs:

$$\Delta s = \frac{y^+ \mu}{u_\tau \, \rho} \tag{12}$$

To calculate Δs using $y^+ = 1$, the wall friction velocity (u_τ) must be calculated first. This is defined as follows:

$$u_\tau = \sqrt{\frac{\tau_w}{\rho}} \tag{13}$$

$$\tau_w = 0.5 C_f \rho u^2 \tag{14}$$

$$C_f = \frac{0.058}{Re^{0.2}} \tag{15}$$

where τ_w is the wall shear stress, u is the freestream velocity, and C_f is the skin friction coefficient.

2.6.2. Discretization Error Methods

Analyzing the effect of mesh size on the convergence of an observed phenomenon is crucial to performing CFD analyses correctly. Firstly, iterative convergence is necessary to perform any discretization error estimation, meaning that at least three or four orders of magnitude must be observed for each normalized residual in each analysis for the flow/heating equations to be considered solved. Even though the analysis is considered solved, it does not necessarily mean that the calculated values are correct or match with analytical or experimental solutions. There are several ways to observe the convergence over a series of different mesh sizes, but the two methods utilized to quantify the effects of the mesh in this study are the relative error and grid convergence index (GCI) methods. The investigated value of interest is denoted as ϕ, where the mesh for ϕ_1 (h_1) is finer than the mesh for ϕ_2 (h_2), and so on.

The relative error method starts with a very coarse mesh and observes the behavior at residual convergence. The mesh is then reduced, and the same analysis is performed and compared with the coarser mesh. This process is repeated until little to no difference is observed. The relative error method can be described as:

$$R_{\phi}(\%) = \frac{\phi_2 - \phi_1}{\phi_1} \tag{16}$$

The other method is the grid convergence index (GCI) method, utilizing the Richardson extrapolation for discretization error estimation [27]. For a three-dimensional cell grid, the mesh size can be calculated as:

$$h = \left[\frac{1}{N}\sum_{i=1}^{N}(\Delta V_i)\right]^{1/3} \tag{17}$$

where ΔV_i is the volume of a cell, and N is the total number of cells in the mesh. The value of h is typically specified as the mesh base element size in many CFD software.

To perform the GCI method, three significantly different mesh sizes must be simulated with identical conditions (h_1, h_2, h_3). The order from fine to coarse is $h_1 < h_2 < h_3$. Based on industry/research experience, the recommended grid refinement factor $r = h_{coarse}/\ h_{fine}$ should be greater than 1.3. The apparent order p can be determined using the following expressions:

$$p = \frac{1}{\ln(r_{21})}\left|ln|\varepsilon_{32}/\varepsilon_{21}| + q(p)\right| \tag{18}$$

$$q(p) = \ln\left(\frac{r_{21}^{p} - s}{r_{32}^{p} - s}\right) \tag{19}$$

$$s = 1 \cdot sgn(\varepsilon_{32}/\varepsilon_{21}) \tag{20}$$

where $r_{21} = h_2/h_1$, $r_{32} = h_3/h_2$, $\varepsilon_{32} = \phi_3 - \phi_2$, and $\varepsilon_{21} = \phi_2 - \phi_1$. If both r ratios are constant, then $q(p)$ becomes zero, allowing the iterative process to be bypassed. When the r ratios are not constant, p can be solved using fixed-point iteration by setting the initial guess to an arbitrary number. After several iterations using Equations 18-20, the apparent order p can be determined. If s is positive, then monotonic convergence is observed, showing the converged values continuously approaching a particular value as the mesh is further discretized towards zero. If s is negative, then oscillatory convergence is observed, showing that as the mesh is discretized further, the behavior oscillates around a specific value. Once the apparent order is determined, the extrapolated values between h_2 and h_1 and between h_3 and h_2 can be calculated using the following relationship:

$$\phi_{ext}^{21} = \left(r_{21}^{p}\phi_1 - \phi_2\right)/(r_{21}^{p} - 1) \tag{21}$$

Using the extrapolated value for Eq. 21, the approximate relative error and extrapolated relative error can be calculated using the apparent order p:

$$e_a^{21} = \left|\frac{\phi_1 - \phi_2}{\phi_1}\right| \tag{22}$$

$$e_{ext}^{21} = \left|\frac{\phi_{ext}^{21} - \phi_1}{\phi_{ext}^{21}}\right| \tag{23}$$

Finally, the fine-grid convergence index, which is the percentage difference the fine grid (h_1) is away from the asymptotic numerical value, can be determined using the following expression:

$$GCI_{fine}^{21} = \frac{1.25e_a^{21}}{r_{21}^{p} - 1} \tag{24}$$

Chapter 3: Numerical Setup

The numerical setup and preliminary studies conducted to compute the heat transfer and pressure drop of FLiBe in a randomly packed pebble bed are presented here. The determination of the thermophysical properties of FLiBe used in this study is discussed. The turbulence model is investigated and validated against established heat transfer coefficient data for a randomly packed pebble bed using FLiBe as the coolant. The effects of the mesh and minimum gap size are investigated. The relative and GCI methods for quantifying discretization error are presented for a single Pr and various Re. After concluding on an appropriate mesh and gap size, the effects of the number of pebbles are investigated, determining an appropriate minimum number of pebbles necessary to quantify a converged Nu with the increasing number of pebbles.

3-1. Thermophysical Properties of FLiBe

FLiBe is a high-Pr ionic salt that operates at high temperatures and low pressures, possessing an extensive range of reactor operating temperatures ranging from 459°C to 1430°C. Unlike other popular Gen IV reactor coolants such as sodium or potassium metals, FLiBe possesses a relatively docile mechanical reaction with water and air. Due to this passive safety characteristic, loss-of-coolant accident (LOCA) scenarios are less likely, even with its low solubility and hygroscopic properties. The composition of FLiBe used in all current PB-FHR concepts is a combination of lithium fluoride and beryllium fluoride (LiF-BeF_2 or $2LiF$-BeF_2 with 67-33 mol% composition). The combination of the chemical composition and operating conditions makes FLiBe an incredibly effective coolant with the aptitude to operate in a temperature-strenuous environment. However, this compound contains the carcinogenic behavior of beryllium and the highly corrosive nature of lithium. Thus, several safety accommodations are necessary to ensure the perpetuity of the reactor system operations and the safety of those working with it.

The behavior of FLiBe under normal operating conditions can be numerically calculated by applying the thermophysical properties into computational calculations. The thermophysical properties for FLiBe needed for this study are density $(\rho)_p$, dynamic viscosity $(\mu)_p$, specific heat capacitance $(C_p)_p$ and thermal conductivity $(k)_p$. The subscript "p" denotes the prototypical fluid, which for this study is FLiBe. Since the only data available describing the theoretically ideal thermophysical properties are obtained through experimental studies, the history of FLiBe thermophysical property correlations is presented.

3.1.1. History and Relevance of FLiBe

The quantification of the thermophysical properties of FLiBe has been extensively researched since the inception of the idea of molten salt coolants for reactor technologies in the early 1950s and 1960s. The majority of the data collection efforts for molten salt thermophysical properties originated from Oak Ridge National Laboratory (ORNL), catalyzed by the Aircraft Nuclear Propulsion (ANP) and the Molten Salt Reactor Experiment (MSRE) programs sponsored by the Atomic Energy Commission (AEC) and the United States military.

The first attempts at measuring the thermophysical properties of molten fluoride salt mixtures were performed at ORNL [28], where correlations predicting the liquid densities of fluoride mixtures at elevated temperatures were developed. The quantification of liquid densities of fluoride mixtures was accomplished through applying Archimedes' principle of buoyancy, which was experimentalized by suspending a plummet in molten salt from an analytical balance entirely cased in a hermetically sealed dry-box. In 1956, a thorough summary of the thermophysical properties obtained through experimental studies was published, reporting on several different compositions of fluoride salts, two of which included varying compositions of FLiBe [29]. Similar to previous experiments, the experimental results derived from the buoyancy principle were repeated to ensure the density measurements were in accordance with previous work. From the repeated experiments, the density error analysis results were shown to have at most a $\pm$5% difference between the data collected and the actual values, and the correlation developed from their experimental data was also within $\pm$5%. The specific heat capacity was determined by testing the molten salts with two different constant-pressure calorimeters (ice and copper block), with their data showing a $\pm$20% error for predicted values and $\pm$10% range of experimental accuracy. The dynamic viscosity of FLiBe was determined through two devices, a capillary efflux viscometer and a modified Brookfield rotational device, which exhibited similar results to the specific heat capacity results, showing $\pm$20% error for predicted values and $\pm$10% range of experimental accuracy. The thermal conductivity of FLiBe was determined using one-directional heat flow, which reported errors less than $\pm$25%. From their results, it was determined that some thermophysical properties (ρ and k) could be linearly expressed as a function of temperature.

In 1968, many of the thermophysical properties of FLiBe and other molten fluoride salts were compiled by Cantor [30]. The additivity of molar volumes estimated correlations for the density of various liquid fluoride salts by determining the density at two different temperatures

and determining the thermophysical property constants. The maximum uncertainty determined for the density of FLiBe was 2%. The specific heat capacitance for molten salts was estimated by assuming the mole-fraction additivity and assigning set values based on the average cal/mol·K derived by the simple rule of Dulong and Petit, which states that alkali and alkaline earth halides have roughly 8 cal/mol·K. The liquid specific heat capacitance was defined as the average of two independent sets of measurements, one provided by Hoffman and Lones [31] and the other by Douglas and Payne [32]. The maximum uncertainty determined for the specific heat capacity of FLiBe was ±3%. The maximum determined uncertainty for the dynamic viscosity was 15% by Cantor. The thermal conductivity of FLiBe was tabulated from a theoretical equation derived by Rao [33] and adapted for molten salts by Turnbull [34], observing upwards of ±10% uncertainty, as reported by Cornwell [35].

An additional experiment in 1969 was performed to determine the density and dynamic viscosity of FLiBe, specifically using a coaxial-cylinder viscometer [36]. The composition of FLiBe was 64-36 mol% Li-F BeF_2, measured over 200°C temperature intervals. The observed dynamic viscosity showed an exponential decrease in viscosity as the LiF concentration increased. The dynamic viscosity was concluded to display Arrhenius behavior and that the molar volumes were additive.

In 1973, data was published showing the molar volumes obtained from the density measurements for FLiBe to be within 2% of the volumes calculated from additive contributions of the components [37]. The molar volume comparison was accomplished using a dilatometric method for molten salts. The density-temperature curves for FLiBe were given from 25-700°C and were calculated from room-temperature pycnometric determinations and estimated expansivities of the solid salts. The dynamic viscosity of FLiBe was determined using the oscillating-cup method. Around the same time, a method to determine the thermal conductivity of fluoride salt mixtures by using an apparatus that can vary the gap size the fluid can occupy was developed, aptly named the variable-gap method [38]. The variable-gap technique measures fluid thermal conductivity by using forced-convection one-directional heat flow. The specimen thickness can be varied continuously during the operation to understand the impact of undesirable factors such as inhomogeneities, natural convection, radiative heat transfer, and corrosion. The data collected from the variable-gap apparatus with the Rao-Turnbull correlation showed an average deviation of ±5%.

In 1974, Janz developed a correlation for the density of FLiBe using similar methods performed by Cohen and Cantor, using the buoyancy principle to calculate the density and the dilatometric method to measure the dynamic viscosity [39]. The recommended values for the density and viscosity were based on the works of Cantor. A few years later, correlations of the thermophysical properties of peritectic FLiBe, based mainly on the graphical compatibility with the current data [40]. The more complex equations were attained using trial-and-error calculations using multiple linear regression. The thermophysical correlation uncertainties for density, viscosity, specific heat, and thermal conductivity were $\pm$4%, $\pm$40%, $\pm$20%, and $\pm$20%, respectively, showing the viscosity to contain the most significant potential error. The causation of the massive uncertainty was concluded to be the mole composition of LiF and BeF_2, of which many previous studies have varied the chemical composition of FLiBe.

By the end of the 1980s, the Archimedean method for density determination was established to be a very reliable experimental method according to the rule of additivity of molar volumes. The same was established for the specific heat, which was quantified through the mole additivity and was experimentally proven to show little to no variation in the specific heat as a function of temperature, thus concluding the property to be a constant. The thermal conductivity measurements through the calorimeter and variable-gap size methods were in accordance with each other. The dynamic viscosity of FLiBe was still being investigated due to its sensitive nature. In 1988, thermophysical property data for four compositions of FLiBe for the density and nine compositions of FLiBe for the viscosity, extending the varying composition of FLiBe for the viscosity to include the 66-34 mol% LiF-BeF_2 composition, which is used in most MSRs [41]. The density and viscosity correlations published were the same as in 1974.

Molten salt research dwindled from the late 1980s to the early 2000s, and not much new information was published. In 2003, density values at critical conditions (near melting point/critical point) were fitted for the data range of $732.2 < T < 4498.8$ K [42]. In 2006, a non-linear behavior in the density changes of FLiBe was discovered for the temperature range of 943 to 1003 K [43]. The reported reason for the odd behavior was the formation of gas bubbles. A piecewise correlation for density based on temperature was developed based on this finding.

After several years of research into FLiBe thermophysical properties, many literature reviews of molten salt thermophysical properties were published, concluding on many different correlations made throughout the years. Benes and Konings [44] recommended using Cantor's

1974 density correlation and the Hoffman and Lones and Douglas and Payne constant value for specific heat capacity. The thermal conductivity correlation developed by Cooke was determined to be the most widely accepted. The viscosity literature review agreed with several published literature [28,37,45-47].

In 2013, Idaho National Laboratory listed and compiled the thermophysical correlations for 67-33 mol% LiF-BeF2, listing the limitations of existing correlations to predict density, viscosity, specific heat capacity, surface tension, and thermal conductivity [48] values over a range of temperatures. The impact of the thermophysical properties on the Nusselt number was also discussed in the publication. The 2013 INL report is used to quantify the thermophysical properties of FLiBe in this study.

3.1.2. Density

Due to the simplicity of determining the density of fluids, the literature available for the density of FLiBe showed an overall smaller uncertainty than other thermophysical properties. All correlations for density are documented in the literature explicitly as a function of temperature. Similar to other Newtonian fluids, the density of FLiBe exhibits a linear decrease as the temperature increases. Thus, the density can be expressed in the form:

$$\rho = a - bT \tag{25}$$

where ρ (kg/m^3) is the density, T (K) is the temperature, and a and b are thermophysical constants determined through the rule of additivity of molar volumes.

The density of FLiBe and other molten salts were proven to follow the rule of additivity of molar volumes [49], which states:

$$\rho(T) = \frac{\sum_{i=1}^{n} N_i M_i}{\sum_{i=1}^{n} N_i V_i(T)} \tag{26}$$

where N_i is the mole fraction, M_i is the molecular weight, and $V_i(T)$ is the molar volume at temperature T of component i. By determining the density of FLiBe at two different temperatures using the rule of additivity of molar volumes and substituting the density into Eq. 25, the thermophysical constants a and b can be determined.

Janz was one of the first to develop a widely accepted correlation for the density of FLiBe, proposing the following correlation in 1974 for 67-33 mol% LiF-BeF_2 with an applicable temperature range from 800-1080 K:

$$\rho(T) = 2413 - 0.488T \tag{27}$$

In 2003, Zaghloul later added density values at critical conditions (near melting point/critical point) to the data proposed by Janz and fitted the data, resulting in a correlation that accounts for the entire temperature range (732.2-4498.8 K):

$$\rho(T) = 2415.6 - 0.49072T \tag{28}$$

In 2006, Ignat'ev observed a non-linear behavior in the density changes in the range of 943 to 1003 K. He deduced that the odd behavior was because of the formation of gas bubbles. Thus, a piecewise correlation for density based on temperature was developed:

$$\rho(T) = \begin{cases} 2163 \pm 2.3 - (0.406 \pm 0.029)(T - 874.4), & T < 973\ K \\ 2163 \pm 2.3 - (0.687 \pm 0.096)(T - 874.4), & T > 973\ K \end{cases} \tag{29}$$

The correlation proposed by Ignat'ev et al. can be simplified by neglecting the uncertainties provided in the density measurements, resulting in the following piecewise function used in this study.

$$(\rho)_p = \begin{cases} 2518 - 0.406T, & T < 973\ K \\ 2763.7 - 0.0687T, & T > 973\ K \end{cases} \tag{30}$$

3.1.3. Dynamic Viscosity

The dynamic viscosity was proven throughout the literature to have the most considerable uncertainty due to the significant variation with temperature and the differences in mol% compositions tested. The reason why molten salts containing Beryllium (Be^{2+}) tend to be more sensitive to temperature than other molten salts is due to the Be^{2+} cation having a notable tendency to self-associate with itself when the fluoride melt does not possess the requisite number of fluoride anions (1:4 Be:F) to satisfy the valence coordination demands of Be^{2+} [50]. This leads the Be^{2+} cation to extend its electron network and increase its viscosity [51]. Due to this chemical phenomenon, the composition of FLiBe cannot contain more than 45 mol% BeF_2. The higher the mol% of BeF_2 in the salt solution, the more volatile the viscosity is with temperature. From the literature, it was proven that the viscosity of FLiBe showed Newtonian behavior and can be expressed in the form of the Arrhenius equation, which states:

$$\mu = Ae^{B/T} \tag{31}$$

where μ (kg/m·s) is the dynamic viscosity, T (K) is the temperature, and A and B are thermophysical constants.

The determination of the dynamic viscosity was accomplished through several different methods, such as the capillary, oscillating sphere, oscillating hollow cylinder, rotational cylinder,

and coaxial-cylinder viscometrical methods. The dynamic viscosity correlation used in this study was developed by Williams [51] and is applicable for the temperature range of 873-1073 K:

$$(\mu)_p = 0.000116e^{3755/T} \tag{32}$$

3.1.4. Specific Heat Capacity

The specific heat capacity is widely accepted as a constant with little to no variation with temperature. Thus, no simple correlation for heat capacity was developed for FLiBe salt. The only published analytical expression was again from Williams [51], which was based on Dulong and Petit's estimation equation [52]:

$$C_p = \frac{8\sum_{i=1}^{n} N_i p_i}{\sum_{i=1}^{m} N_i M_i} \tag{33}$$

where N_i is the mole fraction, M_i is the molecular weight of component i, and p_i is the number of atoms in a molecule.

The analytical value of 2397.73 J/kg·K at 973 K was presented, whereas corresponding experimentally measured values were 2415.78 J/kg·K. Many of the publications presented in the literature provided values ranging between 2350-2380 J/kg·K. The value used in this study is the one based off the experimental value:

$$(C_p)_p = 2415.78 \tag{34}$$

3.1.5. Thermal Conductivity

Investigations into determining the thermal conductivity of FLiBe discovered a slight linear increase in thermal conductivity with the increase in temperature. The thermal conductivity correlations agree with the temperature range between 500-650 K [43,51,53]. The correlation used in this study is:

$$k = 0.629697 + 0.0005T \tag{35}$$

3.1.6. Ideal Thermophysical Properties

Based on the literature presented for the thermophysical properties of FLiBe, the implemented thermophysical properties to be used in this simulation work are shown in Table 3 and visualized in Figure 12.

Table 3. The chosen thermophysical properties for LiF-BeF2 with 66-37 mol% composition for this analysis.

Thermophysical Property	Equation	Units
Density $(\boldsymbol{\rho})_p$	$2518 - 0.406T$	kg/m^3
Dynamic Viscosity $(\boldsymbol{\mu})_p$	$0.000116e^{3755/T}$	kg/(m·s)
Specific Heat Capacity $(\boldsymbol{C_p})_p$	2415.78	J/(kg·K)
Thermal Conductivity $(\boldsymbol{k})_p$	$0.629697 + 0.0005T$	W/(m·K)

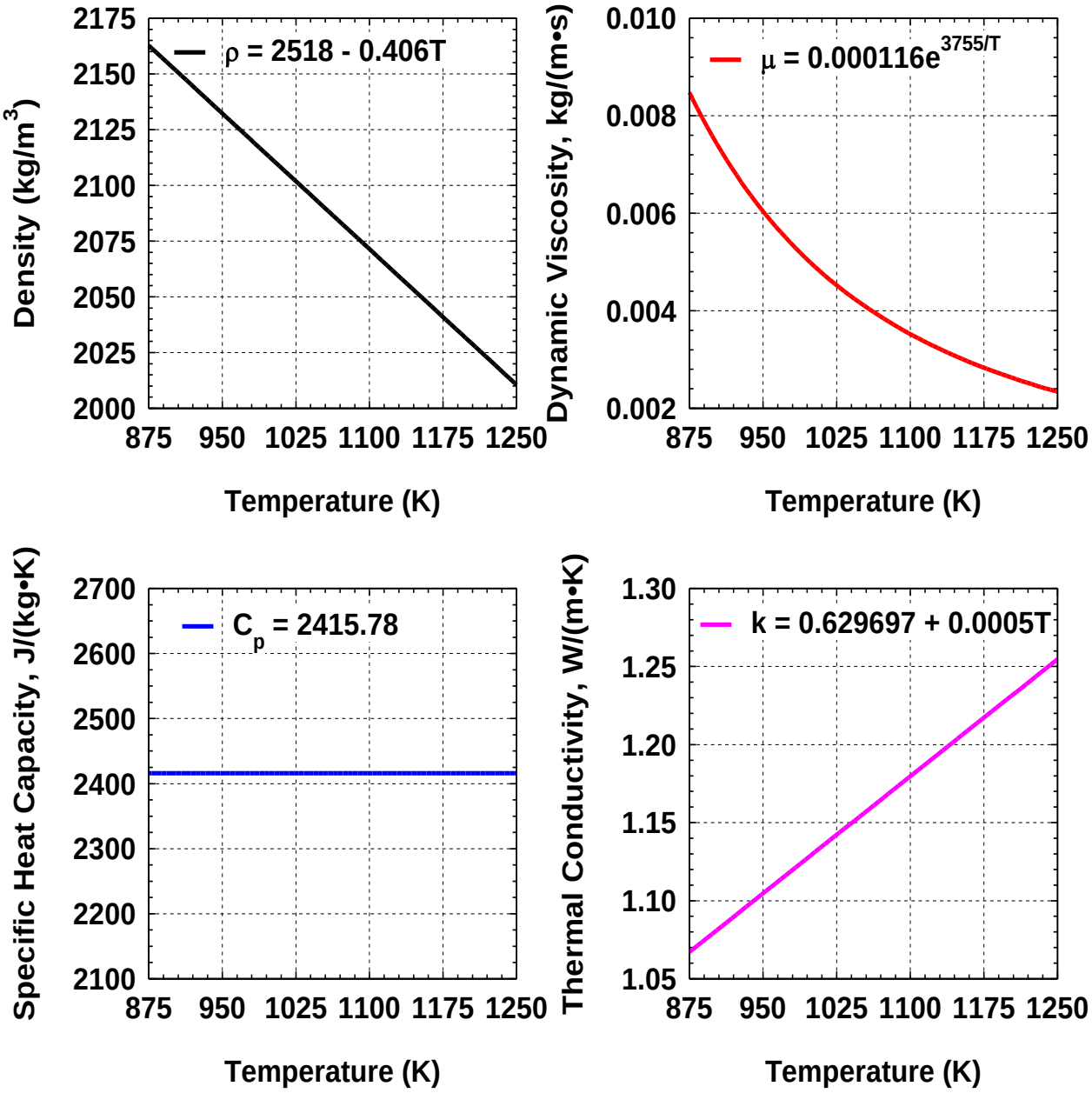

Figure 12. Plotted thermophysical properties over the range of 875 < T < 1250 K.

3-2. Model Validation

The calculated numerical data from this computational analysis must be validated with previously established data to justify this simulation work's turbulence model. A numerical analysis that investigated the heat transfer coefficient of flowing FLiBe in a randomly packed pebble bed was used to validate the proper turbulence model in this analysis [9]. Large-Eddy Simulations (LES) were conducted with FLiBe to produce reference data to evaluate the suitability and applicability of the Reynolds-Average Navier Stokes (RANS) model for packed pebbles. The LES was first conducted for a single FCC pebble channel using the WALE sub-grid scale model and compared with quasi-Direct Numerical Simulation (q-DNS) data [54]. The time averaged velocity and temperature profiles showed a maximum difference of 2.0% between the LES and q-DNS results. Investigations into various turbulence models were then performed to validate their numerical setup with the validated LES data set. The investigated eddy-viscosity-based turbulence models were the Low-Re Realizable k-ε and Low-Re k-ω SST models.

The conclusion from their investigations into various turbulence models showed that the shear-stress transport (SST) k-ω turbulence model with gamma transition and low-Re approach showed better agreement with the q-DNS/LES data than the Realizable k-ε model in terms of both velocity and temperature profiles. The Realizable k-ε model showed a widely different velocity peak location than the k-ω SST model compared with the LES data set. Thus, the k-ω SST model was chosen for their simulations.

The k-ω SST turbulence model solves transport equations for the turbulent kinetic energy k and the specific dissipation rate ω to calculate the turbulent eddy viscosity [55]. The two advection-diffusion equations are presented as follows:

$$\frac{\partial k}{\partial t} + \nabla \cdot (\boldsymbol{u}k) = P_k - \beta^* k\omega + \nabla \cdot [(\nu + \sigma_k \nu_T)\, \nabla k] \tag{36}$$

$$\frac{\partial \omega}{\partial t} + \nabla \cdot (\boldsymbol{u}\omega) = \delta S^2 - \beta \omega^2 + \nabla \cdot [(\nu + \sigma_\omega \nu_T)\, \nabla \omega] + 2(1 - F_1)\frac{\sigma_{w2}}{\omega} \nabla k \cdot (\nabla \omega)^T \tag{37}$$

$$\nu_T = \frac{a_1 k}{\max(a_1 \omega_i S F_2)} \tag{38}$$

where $P_k = min[\nu_T(\nabla \times \boldsymbol{u}) \cdot (\nabla \times \boldsymbol{u})^T, 10\beta^* k\omega]$ and S is the absolute value of the vorticity. The constants in the k-ω SST turbulence model are as follows: $a_1 = 0.31$, $\beta_1 = 0.075$, $\beta_2 = 0.0828$, $\beta^* = 0.09$, $\delta_1 = 0.5532$, $\delta_2 = 0.4403$, $\sigma_{k1} = 0.85$, $\sigma_{k2} = 1.0$, $\sigma_{\omega 1} = 0.5$, and $\sigma_{\omega 2} = 0.856$. The

k-ω SST turbulence model is considered usable at near-wall layers past the viscous sub-layer, thus making it a viable low-Re turbulence model without extra damping. This characteristic of this model is exceptionally beneficial to simulating pebble bed flow using high-Pr fluids since the majority of the heat transfer occurs near or past the laminar sublayer. The second order upwind convection discretization scheme was chosen as the solver for all cases.

The k-ω SST turbulence model utilizes the low-Re approach, incorporating a low-y^+ wall treatment, in which the boundary layer was resolved with a fine layered mesh ($y^+ \sim 1$). The generated fine layered mesh allows for additional modeling beyond the assumption of laminar flow to be omitted. However, STAR-CCM+ does not apply this approach, instead applying standard wall function to obtain the boundary conditions where the centroid of a near-wall cell lies in the viscous sublayer of the boundary layer. Thus, an all-y^+ wall treatment was applied.

The validation data to be used for this analysis [9] reported the average heat transfer coefficient (h_{avg}) for N = 30, 40, 50, and 60 pebbles with a base element size of 0.735-mm, fixed gap size of 0.01-mm, and six prism layers at a single Re. The flow direction was from the bottom of the core to the top, with gravity present. According to their collected data at the single Re and Pr, 50 pebbles was considered a suitable number for h_{avg} to achieve a converged result, showing that further increase in N has little to no effect on h_{avg}. Additionally, the gap size of δ_p = 0.01-mm was considered to be small enough to capture a converged h_{avg} and that further gap size reduction had insignificant effects on h_{avg}. The gap size between the pebble and cylindrical domain was considered negligible.

For this validation study, the same in-house MATLAB code was used to generate randomly packed pebbles containing the same range of the number of pebbles previously simulated, as seen in Figure 13. Using the same turbulence model and mesh specifications used from the validated work, simulations were performed at the same Re and Pr to validate the conclusion provided. Due to the inherent uncertainty present from the randomly defined geometric flow path, the numerical results were not expected to match exactly. According to Figure 14, the difference between the simulation and validation data showed minimal differences (±1%), showing good agreement between the two analyses. Though the used mesh and gap size seemed to provide a leveling off of Nu at around 50 pebbles, the effects of the mesh and minimal gap size between pebbles were investigated further.

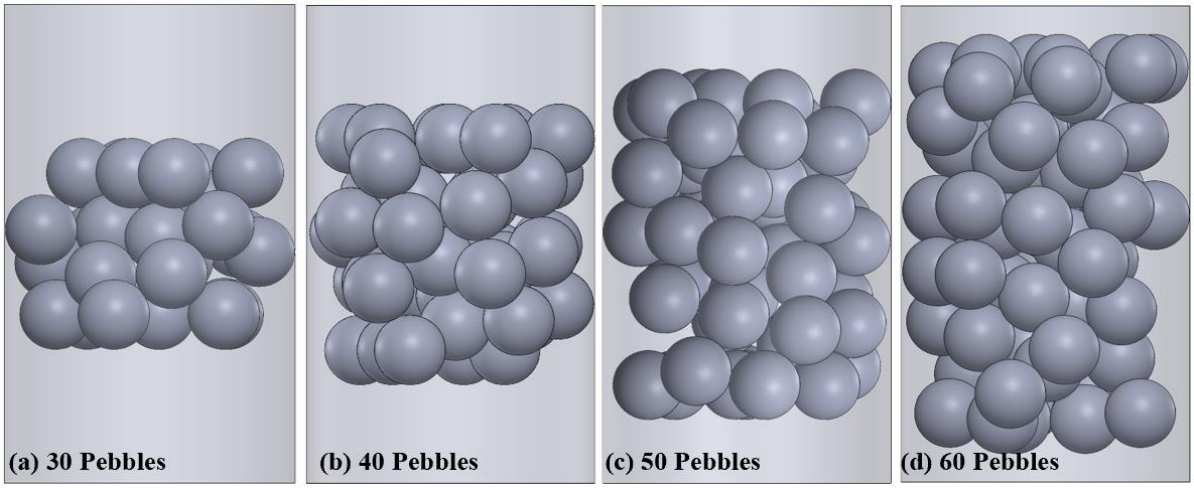

Figure 13. Geometries of randomly packed pebble bed channels used for validation purposes.

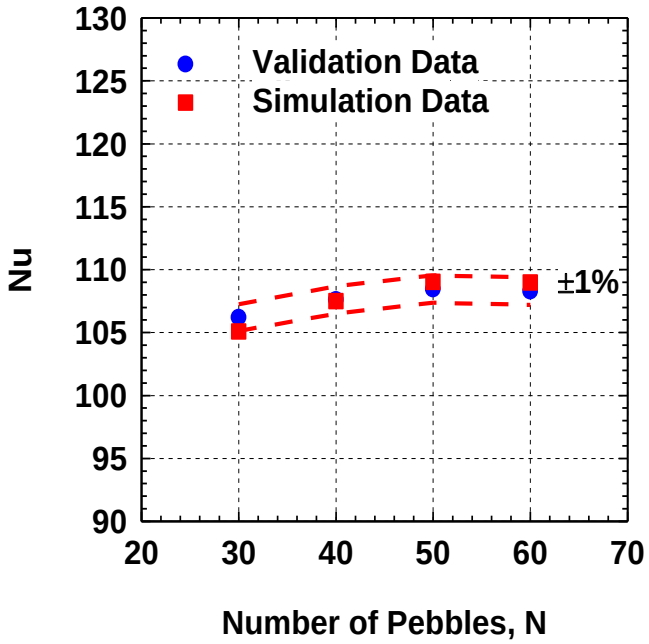

Figure 14. Comparison between the validation data and the current simulation work.

3-3. Effects of Mesh and Gap Size

The mesh and gap sizes were investigated simultaneously to determine the appropriate mesh element size and minimum gap size between pebbles to be used in this simulation work. The original mesh utilized in the validation cases contained seven prism layers with a manually specified prism layer thickness. The mesh generated for this study had six prism layers, but the

total prism layer thickness value was identical to a regular mesh element size. A y^+ analysis was conducted to evaluate the suitability of the original and refined mesh resolutions.

3.3.1. y+ Analysis Results

The original mesh utilized for validation purposes [9] used polyhedral elements with a 0.735-mm base element size and a manually specified total prism layer thickness (PLT) of 1.5-mm. Seven prism layers were specified with a stretching ratio of 1.3. In Figure 15, three meshes are shown comparing the original mesh and two meshes (0.735-mm and 0.5-mm), where the total prism layer thickness was defined as the size of a single element with six prism layers.

Using flat plate boundary theory, the mesh resolution was evaluated for *Pr* = 15.0, as shown in Table 4. Based on Table 4, the original mesh was considered sufficient from the standpoint of flat plate boundary theory. However, due to the tiny gap between each pebble, an accelerated flow was observed at the surrounding boundaries near the non-existing perpendicular contact between pebbles. As the Re increases, the required Δs also decreases. The prism layer thickness was defined as the size of a single element to ensure that the heat transfer phenomenon is captured near the wall in these regions.

Table 4. Prism layer analysis results using a forced y^+ = 1 for Pr = 15.0.

Parameter	Re		
	500	1250	2500
y^+	1	1	1
C_f	0.0168	0.0139	0.0121
τ_w	0.0498	0.2591	0.9023
u_τ	0.0059	0.0137	0.0257
Δs, required (mm)	0.6559	0.2875	0.1541
Δs, 1.5mm PLT (mm)	0.1176	0.1176	0.1176
Δs, 0.735 mm PLT (mm)	0.0576	0.0576	0.0576
Δs, 0.5 mm PLT (mm)	0.0392	0.0392	0.0392

3.3.2.Results of Gap Size Analysis

To investigate the mesh element size and minimum gap size between pebbles, several Re (500, 1250, 2500) were analyzed for 50 pebbles at a single Pr of 15.0 using flowing FLiBe for various element sizes and δ_p as shown in Figure 16. The total prism layer thickness was defined as the thickness of a single element. The element sizes analyzed were 0.8-, 0.735- (original), 0.6-,

0.5-, and 0.4-mm. The investigated minimal gap sizes between pebbles (δ_p) were 0.05-, 0.01-, and 0.005-mm.

According to Figure 16, as the minimum gap between pebbles decreased, there was a slight reduction in the Nu for all investigated Re. The mesh size showed little to no effect on the Nu for the lower Re, but did show slight variation at higher Re. Concerning the pressure drop, a sizeable ΔP reduction was observed at Re = 2500 for δ_p = 0.01-mm. A possible explanation for the severe ΔP reduction is the randomness of the generated flow path. A relative error analysis was conducted at the highest investigated Re to show how the mesh ultimately impacts the Nu and ΔP over all considered gap sizes with the maximum error. The results for the relative error analysis are displayed in Tables 5 and 6.

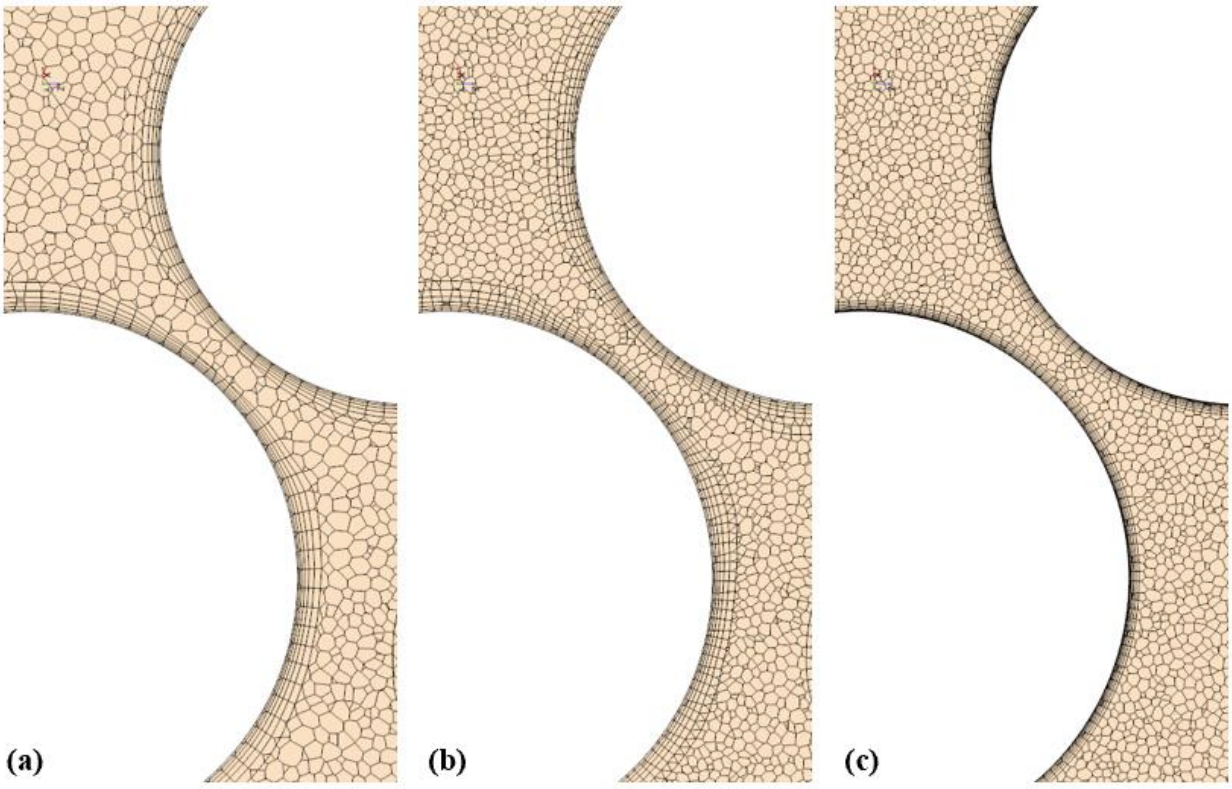

Figure 15. Comparison of mesh refinements: (a) 0.735-mm mesh with 1.5-mm prism layer thickness; (b) 0.735-mm mesh with 100% relative prism layer thickness, (c) 0.5-mm mesh with 100% relative prism layer thickness.

According to Tables 5 and 6, the Nu relative error between reduced mesh sizes decreased similarly for all sizes. However, for δ_p= 0.05-mm, as the base element size decreased, the Nu continued to rise, while δ_p = 0.01-mm and 0.005-mm showed oscillatory values as the base

element size decreased. Relative comparisons of Nu between δ_p= 0.05-mm and 0.01-mm gap sizes showed a massive reduction in the relative error as the element size was decreased. The relative error was slightly reduced further between δ_p= 0.01-mm and 0.005-mm. As the gap size was reduced, the Nu also displayed reduced error relative to the base case. Regarding the pressure drop, the maximum ΔP relative error showed oscillatory behavior, with ≈1% observed for all δ_p. Thus, the minimum gap size between pebbles of $\delta_p = 0.005$-mm was chosen.

Table 5. Nu comparison of the gap size between pebbles and the base element size for 50 pebbles with Pr = 15.0 and Re = 2500.

Base Element Size (mm)	$\delta_p = 0.05$ mm		$\delta_p = 0.01$ mm		$\delta_p = 0.005$ mm	
	Nu	R_{Nu}	Nu	R_{Nu}	Nu	R_{Nu}
0.8	274.438	1.405%	267.068	0.054%	267.201	0.48%
0.735	274.068	1.538%	266.277	0.242%	265.932	0.72%
0.6	275.247	1.115%	265.886	0.389%	264.041	0.10%
0.5	276.330	0.726%	265.806	0.419%	263.790	0.09%
0.4	278.350	BASE	266.925	BASE	264.016	BASE

Table 6. ΔP comparison of the gap size between pebbles and the base element size for 50 pebbles with Pr = 15.0 and Re = 2500.

Base Element Size (mm)	$\delta_p = 0.05$ mm		$\delta_p = 0.01$ mm		$\delta_p = 0.005$ mm	
	ΔP	$R_{\Delta P}$	ΔP	$R_{\Delta P}$	ΔP	$R_{\Delta P}$
0.8	4820.588	0.699%	4556.345	0.344%	4859.649	0.03%
0.735	4843.638	1.181%	4566.262	0.563%	4860.964	0.27%
0.6	4800.296	0.276%	4597.099	1.242%	4847.773	1.06%
0.5	4781.194	0.124%	4485.991	1.205%	4899.639	0.53%
0.4	4787.110	BASE	4540.698	BASE	4925.702	BASE

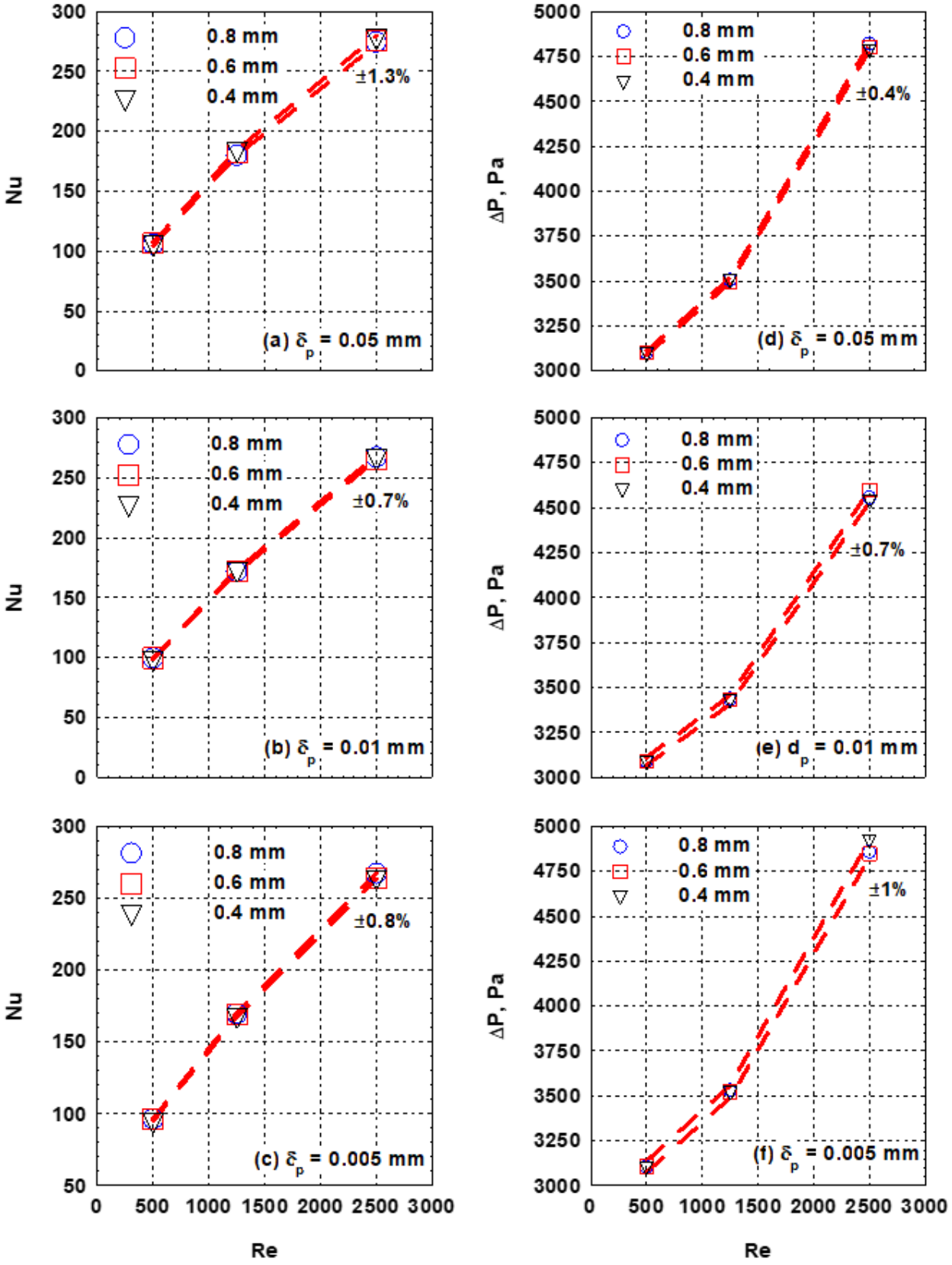

Figure 16. Effects of various minimum gap sizes on the Nu and ΔP for Pr = 15.0.

3.3.3.Results of Mesh Sensitivity Analysis

The sensitivity of the mesh was further investigated using the GCI method for the δ_p = 0.005-mm. The investigated element sizes were h = 0.735, 0.4, and 0.6-mm, Re = 500, 1250, and 2500 and Pr = 15.0. The results of the GCI analyses are presented in Tables 7 and 8.

Table 7. Nu Grid convergence index analysis of Pr = 15.0 for Re = 500, 1250, and 2500.

	Re = 500	Re = 1250	Re = 2500
N_1, N_2, N_3	35895034, 12357587, 6951953		
r_{21}, r_{32}	1.5, 1.225		
ϕ_1, ϕ_2, ϕ_3	95.29, 96.36, 96.31	167.95, 168.95, 169.02	264.02, 264.04, 265.93
p	5.369	3.623	21.207
ϕ_{ext}^{21}	95.153	167.654	264.016
e_a^{21}	1.122%	0.593%	0.0097%
e_{ext}^{21}	0.144%	0.178%	0.0000%
GCI_{fine}^{21}	0.179%	0.222%	0.0000%

Table 8. ΔP Grid convergence index analysis of Pr = 15.0 for Re = 500, 1250, and 2500.

	Re = 500	Re = 1250	Re = 2500
N_1, N_2, N_3	35895034, 12357587, 6951953		
r_{21}, r_{32}	1.5, 1.225		
ϕ_1, ϕ_2, ϕ_3	3105.62, 3107.15, 3106.83	3522.44, 3521.61, 3535.76	4925.70, 4847.77, 4860.96
p	2.840	13.604	3.212
ϕ_{ext}^{21}	3104.91	3522.45	4954.80
e_a^{21}	0.0493%	0.0237%	1.5821%
e_{ext}^{21}	0.0228%	0.0001%	0.5872%
GCI_{fine}^{21}	0.0285%	0.0001%	0.7384%

Based on the GCI results from Tables 7 and 8, the Nu and ΔP percentage errors for the fine-grid solution showed less than 1% error from the asymptotic numerical value based on Richardson extrapolation. The Nu numerical uncertainty for Re = 500 and 1250 was around 0.2%, and for Re = 2500, the Nu numerical uncertainty was practically zero, showing 2E-6% error in the fine-grid solution. The ΔP numerical uncertainty was also less than 1% from the asymptotic numerical value. The maximum uncertainty for ΔP was observed at the highest Re. This location was expected to have the largest uncertainty since more turbulence would be present.

Between the relative error and GCI results, it was concluded that reducing the base mesh element size would provide a more accurate result. The results between the 0.6- and 0.4-mm

meshes were minimal, and a mesh grid size between 0.6- and 0.4-mm would be considered sufficient, though 0.4-mm would be considered the most accurate. However, to run a grid size of 0.4-mm (35895034 elements) for Re = 500, it would take 13.6 hours using 100 processors. If the grid size was increased to 0.5-mm (20775803), the needed time it would take to run using 100 cores would be 8.73 hours. Comparing the 0.5- and 0.4-mm mesh sizes, increasing the base element size of the mesh by 0.1 mm would reduce the run time by 36% with practically no effect on the heat transfer and pressure drop. Thus, the chosen base element size used in this simulation work was 0.5-mm. The finalized mesh utilized in this simulation work is shown in Figure 17.

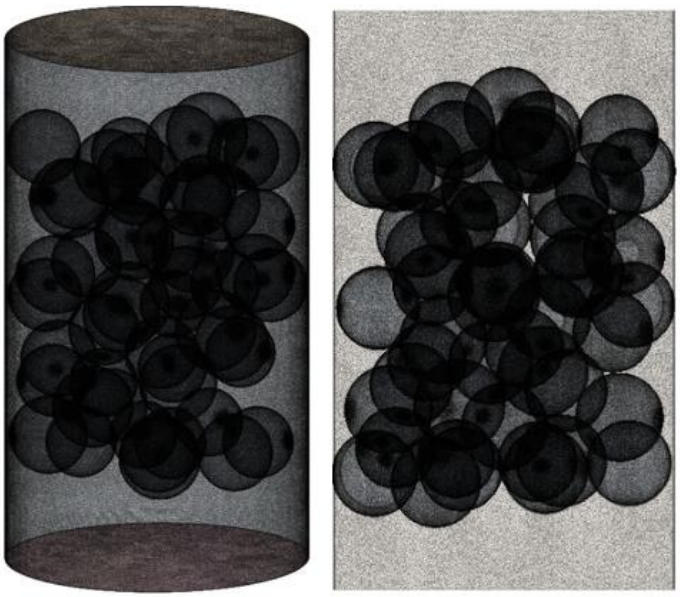

Figure 17. Finalized refined mesh shown for 50 randomly packed pebbles.

3-4. Effects of Number of Pebbles

Using the concluded mesh size and minimum gap size from the performed sensitivity analyses, the cases containing various numbers of pebbles were developed from scratch using δ_p = 0.005-mm and 0.5-mm mesh with 100% relative total prism layer thickness. The numbers of pebbles were extended beyond what was previously reported. The numbers of pebbles investigated were N = 30, 40, 50, 60, 75, and 100. The same Re and Pr were repeated for each case containing the varying number of pebbles, as shown in Figure 18.

Figure 18a showed that the Nu has a slight decrease as the number of pebbles increases. Though no pressure drop data was provided from the validation data [9], the pressure drop was still plotted to show that as the number of pebbles increases, the pressure drop also increases, as

shown in Figure 18b. Using the N = 100 pebbles case as the base value, the Nu relative error between each subsequent pebble increase was calculated, as shown in Table 9.

Table 9. The relative error for extended pebble count study using validation data initial and boundary conditions.

Number of Pebbles, N	Nu	R_{Nu}(%)	ΔP	$\Delta P/N$
30	105.1021597	-2.815%	1912.753	63.758
40	108.1463548	-2.111%	2562.940	64.074
50	110.4791179	-0.781%	3184.563	63.691
60	111.3482207	1.394%	3796.268	63.271
75	109.8173168	0.671%	4775.405	63.672
100	109.0857398	BASE	6323.143	63.231

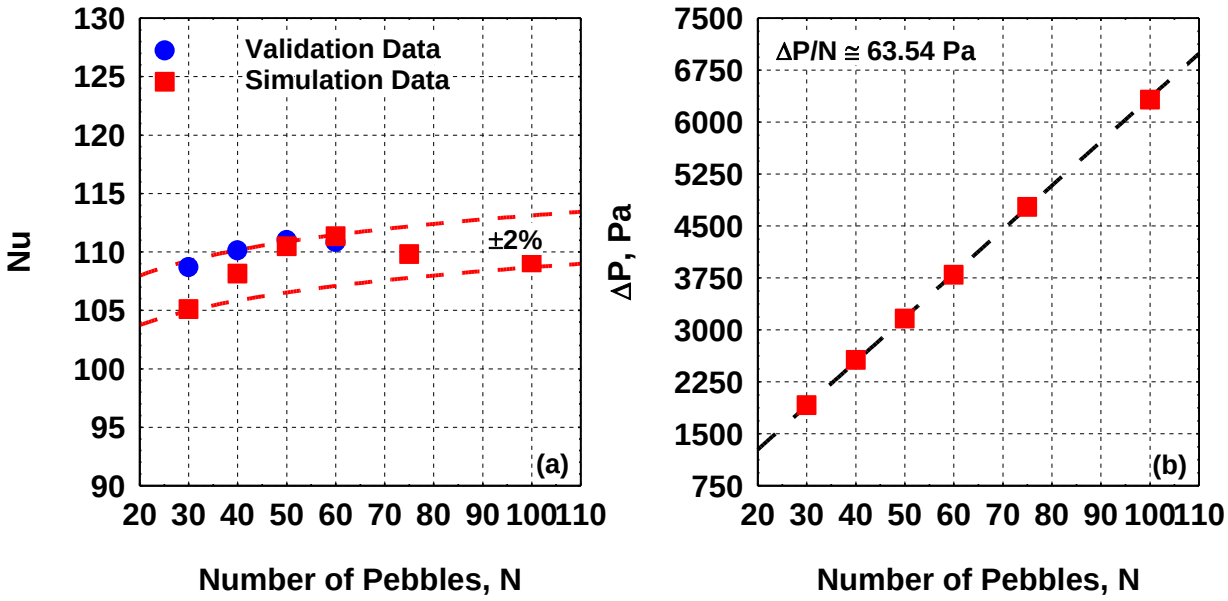

Figure 18. Determination of N using the finalized mesh specification and δ_p.

By curve fitting all the data for N = 40-100, the Nu maximum possible error observed was $\pm$2%, as shown in Figure 19a. The effect of the number of pebbles on the Nu for Re = 500, 1250, and 2500 are plotted in Figure 19b for the same Pr. The maximum difference in the Nu as the number of pebbles increases occurred at the lowest observed Re = 500. Between N = 75 and 100 pebbles, the observed difference was >1% for all investigated Re at Pr = 15.0, showing similar conclusions to what was presented in Table 9 and Figure 18a, which were evaluated for Pr = 19.4.

For Re = 2500 in particular, as the number of pebbles increased, the Nu slightly increased as well. Between N = 75 and 100, there is practically no change, but at N = 40, 50, and 60, the Nu was slightly lower. It can thus be concluded that if only lower Re were to be investigated, the

original N = 50 would be considered sufficient, but if Re were higher, then N = 75 would provide the leveling off for the Nu, and that further increase would be unnecessary.

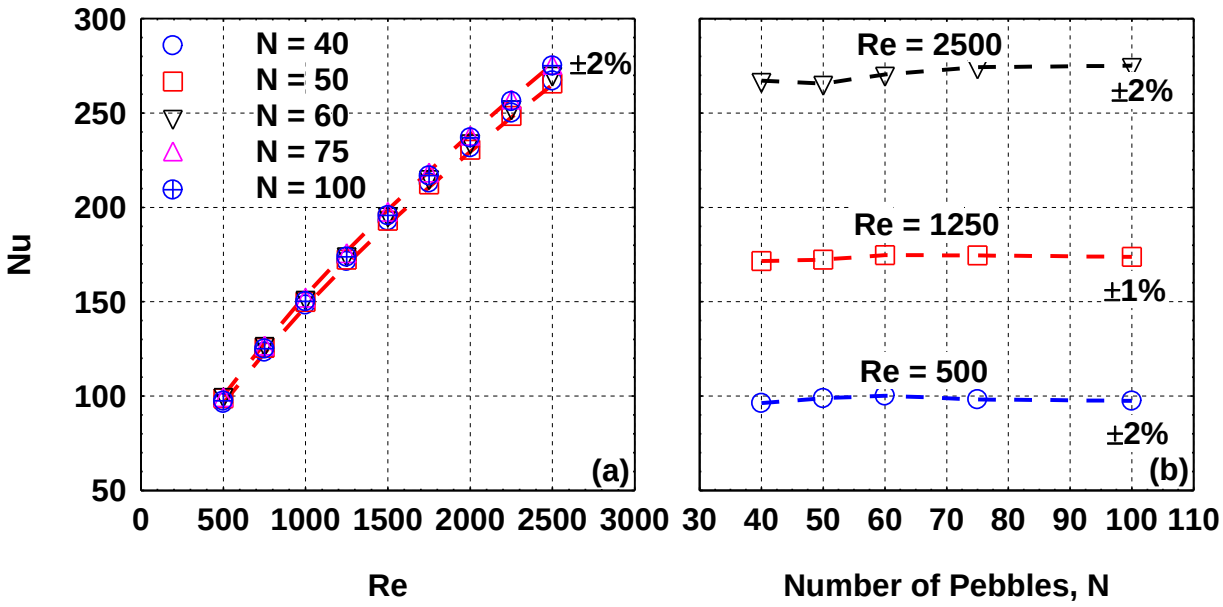

Figure 19. (a) Results for N = 40, 50, 60, 75, and 100 for 500 < Re < 2500 and Pr = 15.0; (b) Average percentage difference with increasing number of pebbles.

The ΔP was plotted against N for Pr = 15.0 in Figure 20a to show how an increase in N would lead to a higher ΔP. To observe the contribution of ΔP per pebble, the ΔP was normalized based on the number of pebbles simulated, as presented in Figure 20b. The observed maximum error between the varying number of pebbles was $\pm$5%.

In conclusion, based on the results from Tables 5 and 7 and Figures 18 and 19, the heat transfer behavior is slightly altered by the number of pebbles being simulated with <1% change observed between N = 75 and 100 pebbles. The pressure drop behavior showed more variation with Re than for Nu, with roughly $\pm$5% observed between N = 75 and 100 pebbles. Thus, N = 75 pebbles were concluded to be an appropriate number of pebbles to simulate for all cases.

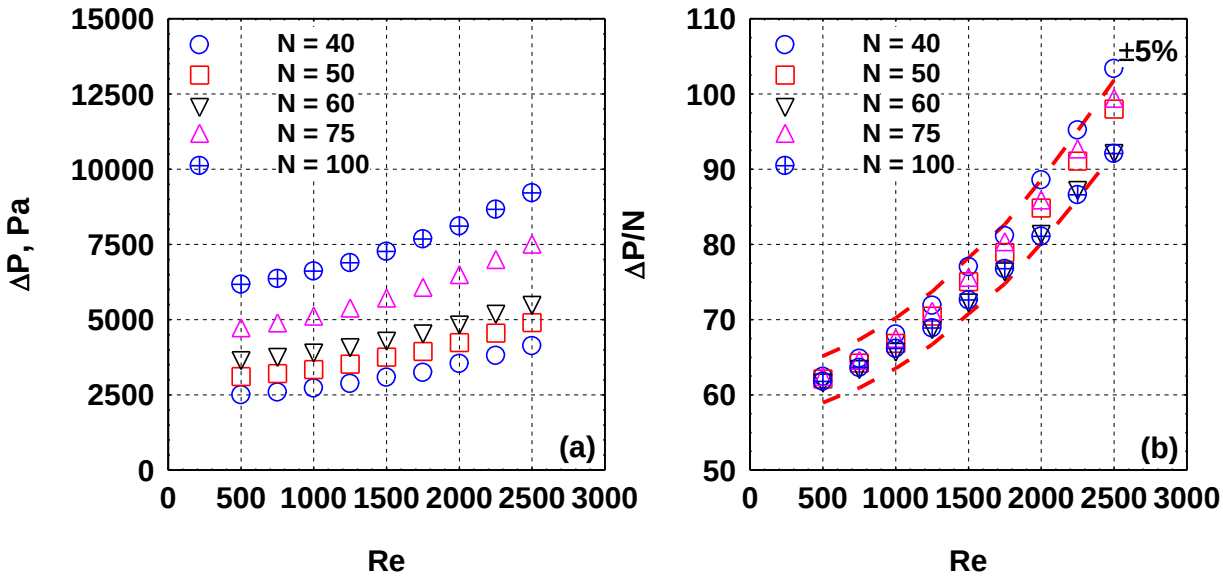

Figure 20. (a) Results for Re vs. ΔP for N = 40, 50, 60, 75, and 100 with Pr = 15.0; (b) Results for Re vs. normalized ΔP with Pr = 15.0.

Chapter 4: Scaling Methodology

Before any nuclear reactor is built at full-scale, the investigated reactor design undergoes several extensive verification procedures using experimental and theoretical analyses at reduced scale using surrogate fluids. Performing reduced scale experimentation requires utilizing similarity scaling techniques, which identify necessary and sufficient conditions required to reproduce a behavior observed at a larger scale. Regarding the determination of reduced scale experimental conditions for convective heat transport similarity, nondimensionalization of the governing differential equations for mass, momentum, and energy conservation produces the Reynolds and Prandtl numbers, which are the two dimensionless numbers necessary to quantify the convective heat transfer performance.

For single-phase incompressible fluids, Re and Pr together produce four degrees of freedom present to design geometrically scaled experiments. These are the length, velocity, average operating temperature, and temperature difference scales encompassed by the thermophysical, geometrical, flow, and heating parameters. By matching the Reynolds and Prandtl numbers, theoretically, the Nusselt number should match. However, due to the complexity of the flow within the PB-FHR core and the use of surrogate fluids in place of the actual coolant, the empirical comparison between the scaled experiment and its prototype always yields some form of distortion of phenomena despite theoretically matching. It is thus imperative to carefully consider each scaling parameter ratio to ensure that the distortion is optimally reduced.

In this chapter, the advantages of using surrogate fluids are discussed. The potential candidates of FLiBe surrogate fluids are identified, and the process of determining them is clarified. The thermophysical properties of the chosen surrogate fluid for this study are defined. The scaling parameters that are reduced/changed are highlighted. The scaling methodology used to define the geometrical, thermophysical, flow, and heating conditions are defined, and the resulting proper ratios are presented. The scaling distortion theory is briefly discussed.

4-1. Surrogate Fluid Utilization in Scaled Experiments

Conducting scaled experiments using surrogate fluids has several advantages compared to using the actual size and coolant. By reducing the size of the experiment, the required flow and heating phenomena to match the hydrodynamic and thermal behavior are reduced. The size reduction allows for low-power heat sources to replicate systems that contain high volumetric heat

sources. Additionally, reducing the size of the experiment contributes to lower inventory and operating costs.

Using surrogate fluids eliminates several potential dangers posed by the actual reactor coolant. For PB-FHRs, the toxicological concerns posed by FLiBe are bypassed by utilizing surrogate fluids, which are typically not corrosive and can match thermophysical properties at more manageable temperatures. Using surrogate fluids instead of FLiBe, safety measures for gaseous tritium and aerosols into the molten salt mixture are unnecessary. In addition, surrogate fluids are much more compatible with off-shelf commercial instrumentation, such as pressure gauges, flowmeters, and thermocouples, than for FLiBe, which typically require custom instrumentation that can withstand the harsh nature of FLiBe at operating conditions.

4-2. Potential Candidates of FLiBe Surrogate Fluids

Bardet and Peterson identified three classes of simulant fluids that can match liquid fluoride salts for geometrically scaled experiments involving convective heat transfer. These were Dowtherm-A, Drakesol 260-AT, and water. Dowtherm-A provided the highest potential temperature limit, recommended up to 400°C with 135 psi of pressure, while the viscosity of Drakesol was shown to degrade when used at temperatures above 120°C. Drakesol has similar properties to the oil used in the Matched Index of Refraction Facility at Idaho National Laboratory [56]. Water can be used for scaled experiments, but only if fluid dynamics is the sole investigated behavior. Out of the three, Dowtherm-A was proven to be the optimal surrogate fluid for FLiBe and other liquid fluoride salts.

4-3. Thermophysical Properties of Dowtherm-A

Shortly after World War 1, Dow Chemical Co. produced diphenyl ether ($C_{12}H_{10}O$) as a by-product of the hydrolysis process of chlorobenzene and caustic soda. Diphenyl ether has a melting point of 70°C, but when mixed with diphenyl with a ratio of 26.5 mol% diphenyl to 73.5 mol% diphenyl ether, the melting temperature decreases to 12°C [57]. This eutectic mixture was labeled Dowtherm-A and is currently considered one of the most thermally stable synthetic organic heat transfer fluids. Given its long fluid life, low operating pressures, and large operating temperatures, Dowtherm-A has been utilized extensively in the pharmaceutical, oil, gas, plastic processing, chemical processing, solar energy, and heat recovery industries. In 2008, Bardet and Peterson experimentally investigated potential simulant-fluid candidates for several categories of liquid

fluoride salts, including FLiBe. One of the potential surrogate fluid candidates for FLiBe was Solutia Therminol® VP-1, which several chemical companies commercialized under different names, such as Dowtherm-A and Xceltherm MK1. They discovered that Dowtherm-A could simultaneously reproduce the Reynolds, Froude, Prandtl, and Grashof numbers for FLiBe in a straight tube. Implementations of Dowtherm-A into scaled experiments were performed on behalf of Kairos Power [58], demonstrating Dowtherm-A to be an acceptable surrogate fluid for molten FLiBe salt for some types of scaled Integral Effects Tests (IETs). Their investigations determined that the principal thermal fluid properties can be appropriately scaled with minor distortions over the range of conditions expected for both normal and off-normal operating conditions of the KP-FHR.

The thermophysical properties of Dowtherm-A used in this study were initially presented in an INL report for future implementation into the RELAP5-3D/ATHENA computer programs [59]. Similar to FLiBe, the liquid Dowtherm-A behavior displays Newtonian behavior and is solely dependent on the temperature of the fluid. The curve fits for the thermophysical properties of Dowtherm-A data were obtained through a Dow Chemical Company brochure [60] and were transformed into polynomial equations using regression analysis techniques. The general form of the polynomial equation used for each property was:

$$property = a + bT + cT^2 + dT^3 + eT^4 + fT^4 + \cdots \quad (39)$$

Since the single-phase properties for liquid Dowtherm-A are not given, it is assumed to be very close to the saturated data at the same temperature. The saturated liquid properties for density $(\rho)_m$, dynamic viscosity $(\mu)_m$, specific heat capacitance $(C_p)_m$ and thermal conductivity $(k)_m$ were listed for Dowtherm-A for a temperature range of 285.15 K to 698.15 K, but for some cases, the curves were required to fit the data range from 318.15 K instead due to some of the input data between 285.15 K and 318.15 K missing from the Dowtherm-A saturated liquid data.

The following regression coefficients determined for saturated liquid Dowtherm-A are presented in Table 10. The Dowtherm-A data from the Dow Chemical brochure and the curve fits are plotted in Figure 21.

The dynamic viscosity required an 8th-degree polynomial, requiring three additional regression coefficients, which were as follows: g = 9.433$\times 10^{-15}$, h = -5.264$\times 10^{-18}$, and i = 1.275$\times 10^{-21}$.

Table 10. Regression coefficients for single-phase thermophysical properties of Dowtherm-A.

Property	a	b	c	d	e	f
$(\rho)_m$	1.493×10^{3}	-3.332	1.248×10^{-2}	-2.968×10^{-5}	3.444×10^{-8}	-1.622×10^{-11}
$(\mu)_m$	5.135	-8.395×10^{-2}	5.971×10^{-4}	-2.409×10^{-6}	6.029×10^{-9}	-9.579×10^{-12}
$(C_p)_m$	-2.364×10^{3}	3.964×10^{-1}	-1.703×10^{-1}	3.904×10^{-4}	-4.422×10^{-7}	1.979×10^{-10}
$(k)_m$	1.856	-8.395×10^{-3}	5.971×10^{-4}	-2.409×10^{-6}	6.029×10^{-9}	-9.579×10^{-12}

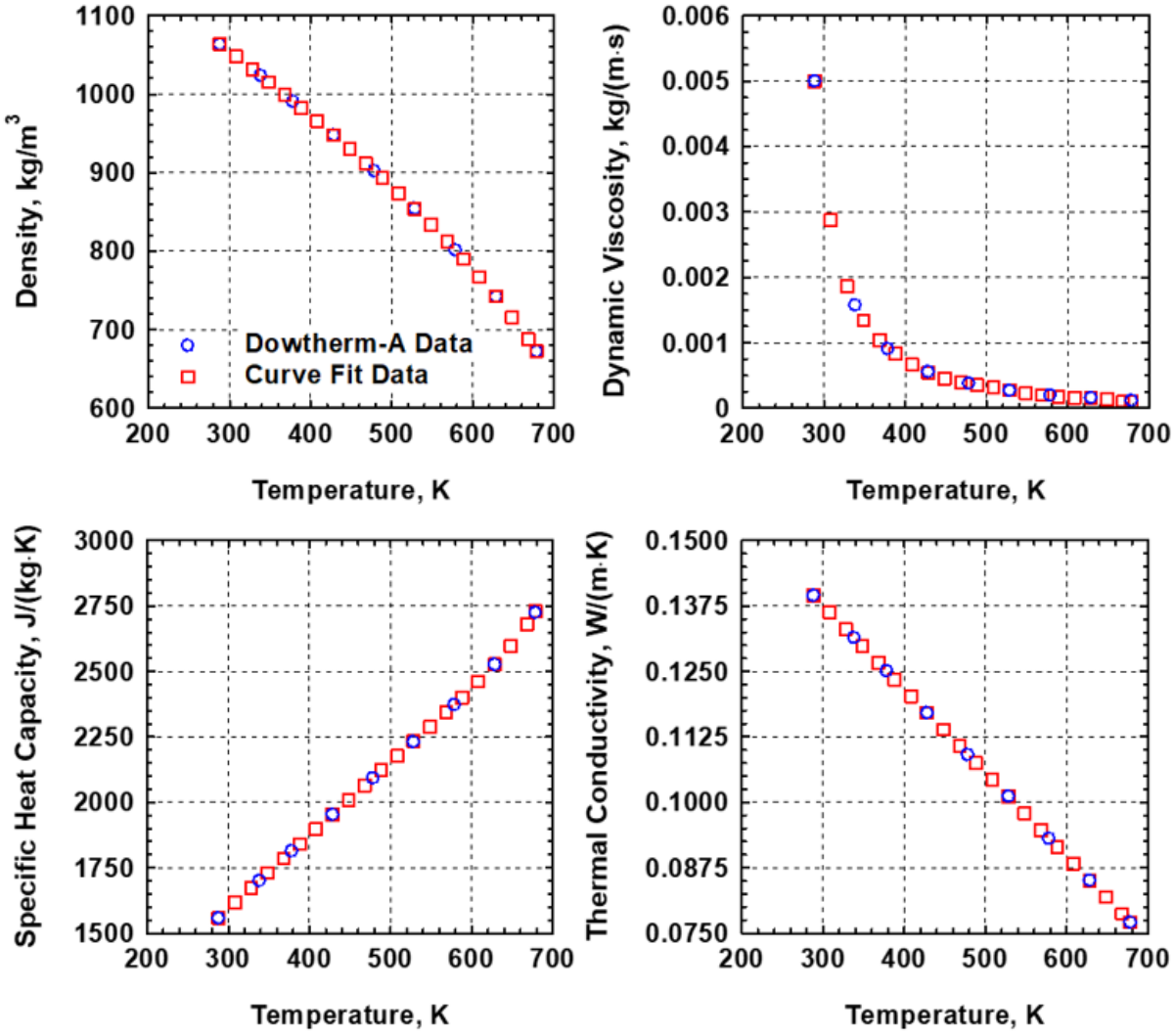

Figure 21. Comparison between Dowtherm-A data and polynomial equations using developed regression coefficients.

4-4. Scaling Methodology

The important scaling parameters for this study are encompassed by the geometrical, thermophysical, flow, and heating conditions. To achieve the model's parameters to theoretically equate the Nu of the prototype, ratios of the necessary geometrical and thermophysical properties

are defined first to define the ratios of the flow and heating conditions. These ratios only approximate the input and output relations of a system. Thus, every condition is defined as constants throughout the system to achieve a steady state. The ratios that help define the model's initial and boundary conditions are defined as:

$$R = \frac{m}{p} \tag{40}$$

where R is the ratio, m is the model, and p is the prototype. The geometrical length scales that are investigated are 1:1 (1.00 Scale), 0.75:1 (0.75 Scale), and 0.5:1 (0.5 Scale), as shown in Figure 22.

Changing the length scale or replacing the coolant with a surrogate fluid independently affects the flow and heating behavior. Thus, either the length scale or Pr must be matched first, but neither the flow nor heating conditions can be determined without first determining the geometrical dimensions with a reduced length scale and matching Pr between the model and prototype. For this study, the Pr is matched first, due to being solely dependent on the thermophysical properties of the fluids.

4.4.1. Thermophysical Property Ratios

The imposed Pr similarity conditions between the model (m) and the prototype (p) are as follows:

$$(Pr)_R = \frac{(Pr)_m}{(Pr)_p} = \frac{(\mu)_m (C_p)_m/(k)_m}{(\mu)_p (C_p)_p/(k)_p} = 1 \tag{41}$$

The equivalent temperatures for Dowtherm-A that match Pr were determined through calibrating the Dowtherm-A thermophysical property equations. Using an excel goal seek what-if analysis, the equivalent temperatures of Dowtherm-A were manipulated to match Pr of FLiBe. The equivalent temperatures for each Pr are presented in Table 11 and visualized in Figures 23-27.

Table 11. Equivalent temperatures between FLiBe and Dowtherm-A that produces identical Pr.

Pr	T_{FLiBe} $(°C)$	$T_{Dowtherm-A}$ $(°C)$
19.4	600	68.058233
15.0	650	92.233500
11.9	700	119.66225
9.64	750	146.78094
7.95	800	177.82780

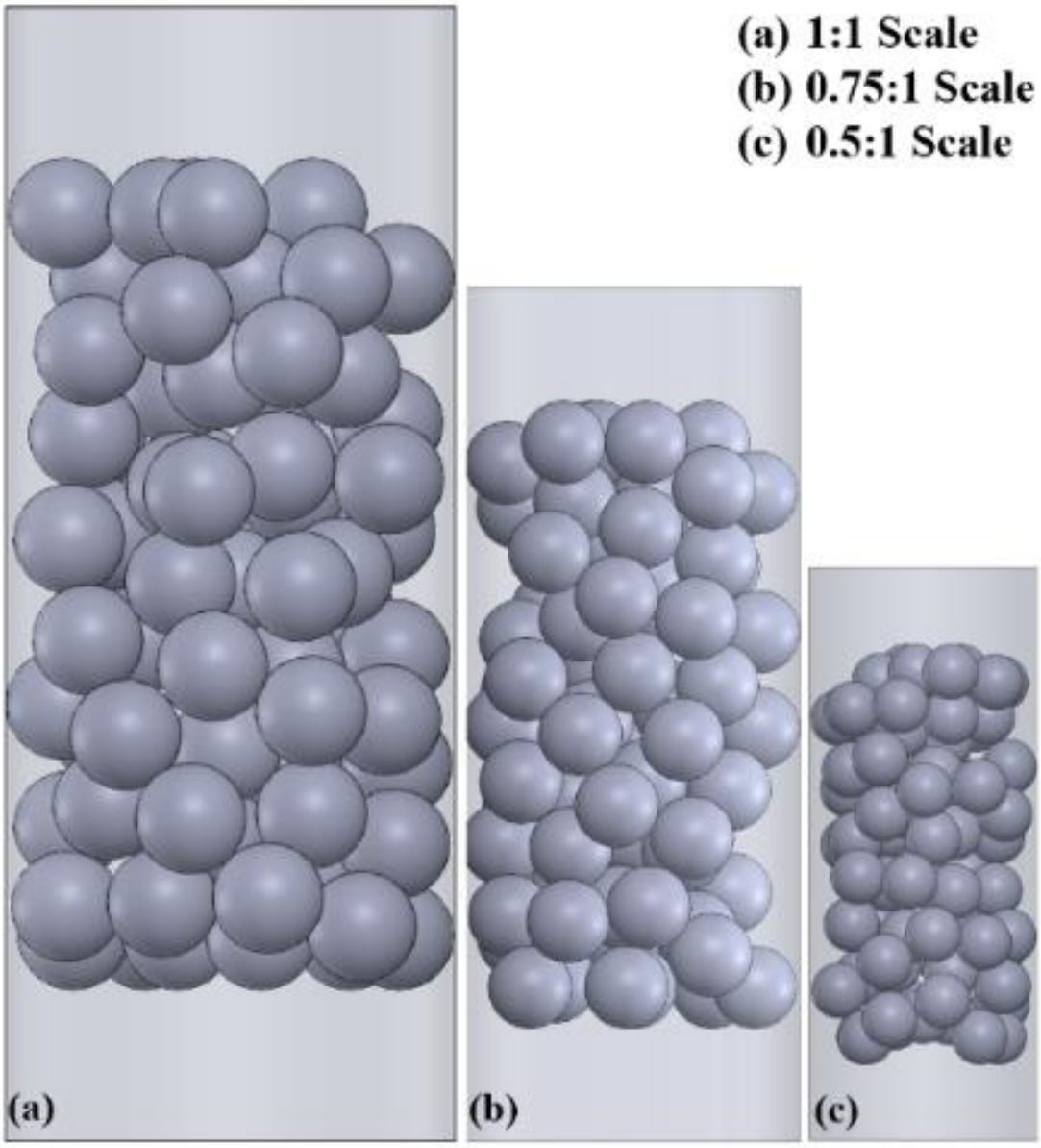

Figure 22. Geometries of varying scales for surrogate fluid cases.

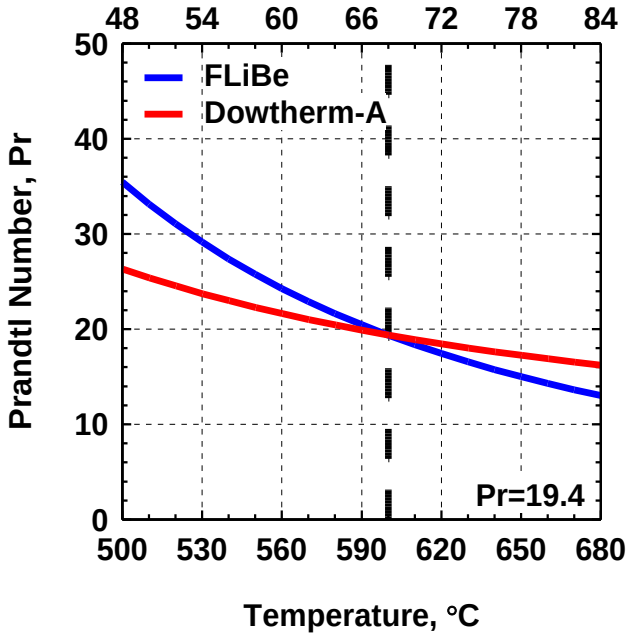

Figure 23. Equivalent temperatures of FLiBe and Dowtherm-A that match *Pr* = 19.4.

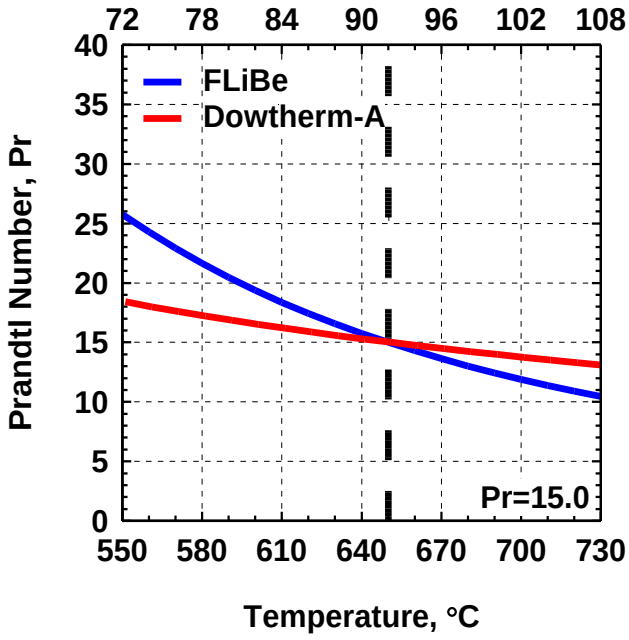

Figure 24. Equivalent temperatures of FLiBe and Dowtherm-A that match *Pr* = 15.0.

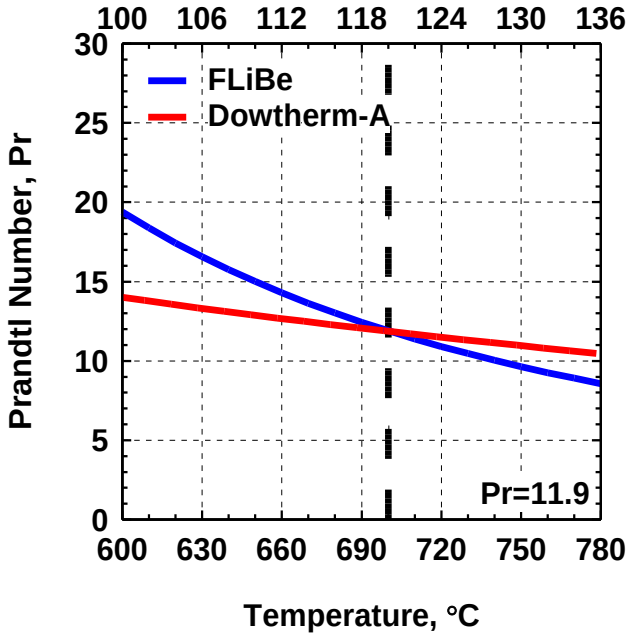

Figure 25. Equivalent temperatures of FLiBe and Dowtherm-A that match *Pr* = 11.9.

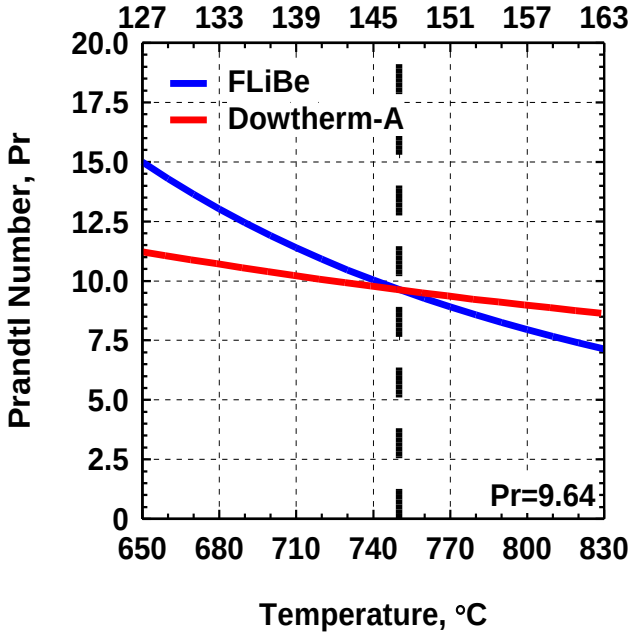

Figure 26. Equivalent temperatures of FLiBe and Dowtherm-A that match *Pr* = 9.64.

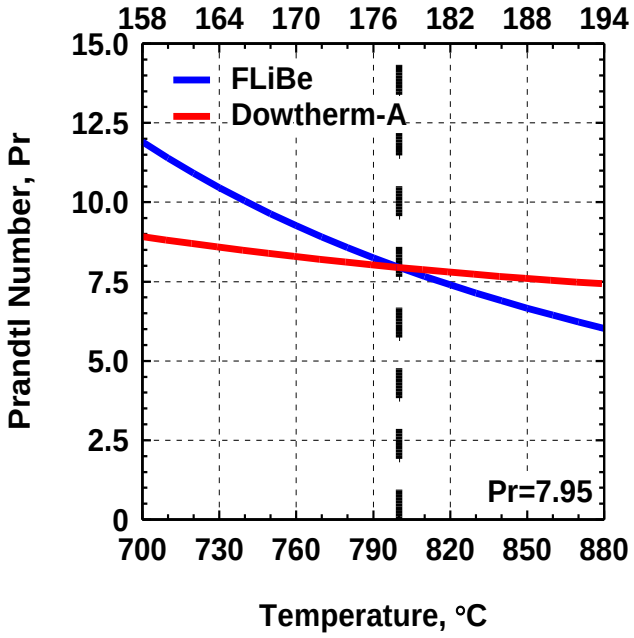

Figure 27. Equivalent temperatures of FLiBe and Dowtherm-A that match Pr = 7.95.

Based on the equivalent temperatures that result in matching Pr between FLiBe and Dowtherm-A, the thermophysical property ratios for the density, dynamic viscosity, specific heat capacity, and thermal conductivity can be determined. The imposed thermophysical property relationships and the determined thermophysical property ratios are shown in Eq. 42 and Table 12:

$$(\rho)_R = \frac{(\rho)_m}{(\rho)_p}, \quad (\mu)_R = \frac{(\mu)_m}{(\mu)_p}, \quad (C_p)_R = \frac{(C_p)_m}{(C_p)_p}, \quad (k)_R = \frac{(k)_m}{(k)_p} \tag{42}$$

Table 12. The thermophysical property ratios determined by matching Pr at certain temperatures.

Property	19.4	15	11.9	9.64	7.95
$(\rho)_R$	1:2.12	1:2.14	1:2.17	1:2.2	1:2.25
$(\mu)_R$	1:5.76	1:6.32	1:6.98	1:7.7	1:8.58
$(C_p)_R$	1:1.41	1:1.36	1:1.3	1:1.25	1:1.2
$(k)_R$	1:8.14	1:8.58	1:9.09	1:9.64	1:10.3

4.4.2. Geometrical Parameter Ratios

The length scale ratios were chosen manually for this study. The geometrical scaling factor ratios for 1D, 2D, and 3D parameters are appropriately defined, as shown in Table 13.

Table 13. Dimensional scaling based on length scale factor

Geometrical Parameter Ratios	1.00 Scale	0.75 Scale	0.5 Scale
Length Ratio, l_R	1:1	1:1.333	1:2
Hydraulic diameter ratio, D_R	1:1	1:1.333	1:2
Area ratio, A_R	1:1	1:1.777	1:4
Volume ratio, V_R	1:1	1:2.370	1:8

Using the chosen length scales, the appropriate dimensions of the cylindrical domain for each size case were identified, as shown in Table 14. The prototype dimensions were derived from the validated case geometry [9].

Table 14. The geometrical parameters used to create geometry surrounding the pebble domain based on length scale factor

Prototype		Model				Units
Parameter	Full-Scale	Parameter	1.00 Scale	0.75 Scale	0.5 Scale	
$(A_{cyl})_p$	11670.22	$(A_{cyl})_m$	11670.22	6564.499	2917.555	mm^2
$(D_{cyl})_p$	121.8974	$(D_{cyl})_m$	121.8974	91.42308	60.94872	mm
$(R_{cyl})_p$	60.94872	$(R_{cyl})_m$	60.94872	45.71154	30.47436	mm
$(H_{cyl})_p$	309.0107	$(H_{cyl})_m$	309.0107	231.7581	154.5054	mm
$(D_p)_p$	30	$(D_p)_m$	30	22.5	15	mm
$(A_s)_p$	2827.433	$(A_s)_m$	2827.433	1590.431	706.8583	mm^2
$(V_p)_p$	14137.17	$(V_p)_m$	14137.17	5964.117	1767.146	mm^3
$(V_{t,p})_p$	1060288	$(V_{t,p})_m$	1060288	447308.8	132535.9	mm^3
$(V_{cyl,p})_p$	2650719	$(V_{cyl,\ p})_m$	2650719	1118272	331339.9	mm^3
$(H_p)_p$	227.1353	$(H_p)_m$	227.1353	170.3515	113.5676	mm
$(H_{add})_p$	81.87546	$(H_{add})_m$	81.87546	61.40659	40.93773	mm

4.4.3. Flow Conditions Ratios

To allow the scaled experiment to reproduce the flow transitions from laminar to turbulent and wall shear stress, the Re must be matched. The imposed Re similarity condition between the model (m) and prototype (p) is as follows:

$$(Re)_R = \frac{(Re)_m}{(Re)_p} = \frac{(\rho)_m(u)_m(d_p)_m/(\mu)_m}{(\rho)_p(u)_p(d_p)_p/(\mu)_p} = 1 \tag{43}$$

Since the Re for both the prototype and model are matched manually ($500 < Re < 2500$), the only unknown from the relationship in Eq. 5 are the velocities. These velocities can be determined independently. The resulting velocity ratios $(u_i)_R$ are constants for each Pr and length

scale. The imposed inlet velocity ratio $(u_i)_R$ and determined velocity ratios for each *Pr* and length scale are shown in Eq. 44 and Table 15. The change in velocity for each *Pr* and length scale is provided for visual reference in Figure 28.

$$(u_i)_R = \frac{(u_i)_m}{(u_i)_p} = \frac{(Re_m \mu_m)/(\rho_m (D_p)_m)}{(Re_p \mu_p)/(\rho_p (D_p)_p)} \tag{44}$$

Table 15. Velocity ratios for each investigated *Pr* and length scale.

Pr	1.00 Scale	0.75 Scale	0.5 Scale
19.4	1:2.720	1:2.040	1:1.360
15.0	1:2.951	1:2.214	1:1.476
11.9	1:3.217	1:2.412	1:1.608
9.64	1:3.497	1:2.623	1:1.749
7.95	1:3.823	1:2.868	1:1.911

4.4.4. Heating Power Ratios

When using surrogate fluids in reduced length scale analyses, the heating power is severely reduced due to the changing fluid density, heat capacity, temperature difference, velocity, and flow area ratios. The imposed power ratio $(Q)_R$ can be defined as a function of thermophysical, flow, geometry, and temperature difference ratios:

$$(Q)_R = (\rho)_R (u_i)_R (A)_R \left(C_p\right)_R (T_{H0} - T_{C0})_R \tag{45}$$

Due to the different ratio of coefficients of thermal expansion between FLiBe and Dowtherm-A, the changes in density do not change linearly with temperature. The density of FLiBe changes more rapidly with temperature than for Dowtherm-A. The temperature difference ratio $(T_{H0} - T_{C0})_R$ must be matched so the density changes between the prototype and model are equivalent. By choosing $(T_{H0} - T_{C0})_R$ = 1/3.3, the density changes between FLiBe and Dowtherm-A can match [58].

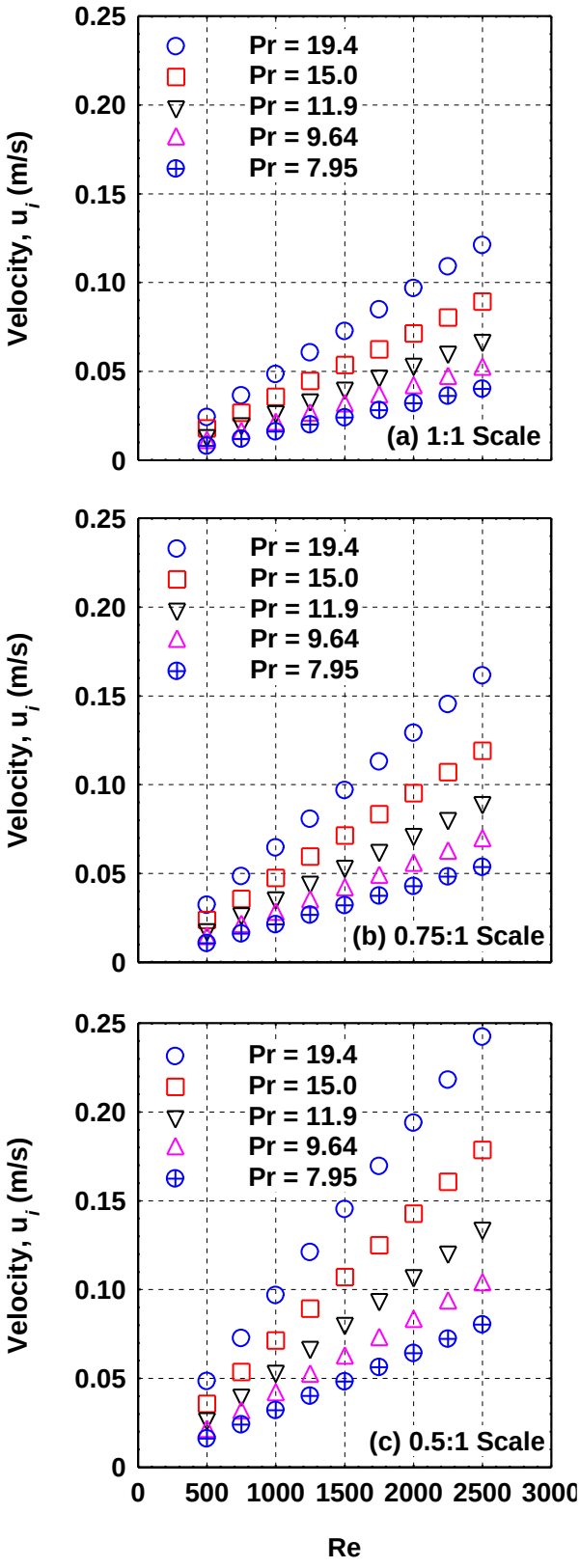

Figure 28. Change in superficial velocity at various Pr for all investigated length scales.

Utilizing the ratios at various Pr and length scales, the required heating power ratio for each pebble at each Pr and length scale was determined, as shown in Table 16.

Table 16. Determination of power ratio required for reduced scales at various Pr.

Length Scale	Pr	$(\rho)_R$	$(u_i)_R$	$(A)_R$	$(C_p)_R$	$(T_{H0}-T_{C0})_R$	$(Q)_R$
1.00 Scale	19.4	1:2.119	1:2.720	1:1	1:1.412	1:3.3	1:26.858
	15.0	1:2.140	1:2.951	1:1	1:1.359	1:3.3	1:28.324
	11.9	1:2.170	1:3.217	1:1	1:1.303	1:3.3	1:30.009
	9.64	1:2.202	1:3.497	1:1	1:1.252	1:3.3	1:31.805
	7.95	1:2.245	1:3.823	1:1	1:1.198	1:3.3	1:33.925
0.75 Scale	19.4	1:2.119	1:2.040	1:1.777	1:1.412	1:3.3	1:35.810
	15.0	1:2.140	1:2.214	1:1.777	1:1.359	1:3.3	1:37.765
	11.9	1:2.170	1:2.412	1:1.777	1:1.303	1:3.3	1:40.011
	9.64	1:2.202	1:2.623	1:1.777	1:1.252	1:3.3	1:42.407
	7.95	1:2.245	1:2.868	1:1.777	1:1.198	1:3.3	1:45.233
0.5 Scale	19.4	1:2.119	1:1.360	1:4	1:1.412	1:3.3	1:53.716
	15.0	1:2.140	1:1.476	1:4	1:1.359	1:3.3	1:56.648
	11.9	1:2.170	1:1.608	1:4	1:1.303	1:3.3	1:60.017
	9.64	1:2.202	1:1.749	1:4	1:1.252	1:3.3	1:63.610
	7.95	1:2.245	1:1.911	1:4	1:1.198	1:3.3	1:67.840

The power ratio $(Q)_R$ was then used to calculate the appropriate heating power per pebble, as shown in Figure 29.

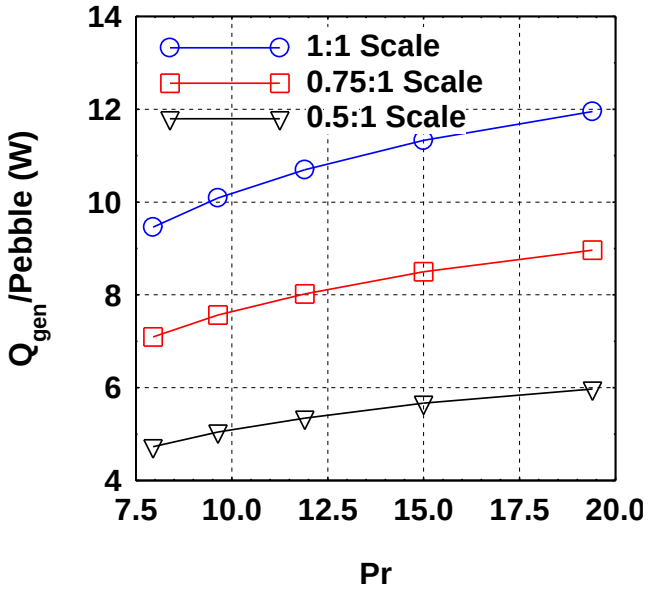

Figure 29. Power provided to each pebble for each reduced length scale case and Pr.

4-5. Scaling Distortion Theory

Scaling distortions are passively created when applying similarity scaling, which is based on similitude theory. Similitude theory is the branch of engineering science that seeks to identify the necessary and sufficient conditions required to reproduce a behavior typically observed at a larger scale. The similarity scaling laws applied to experimental conditions of a scaled model are related to the prototype by similarity conditions, as described in Figure 30.

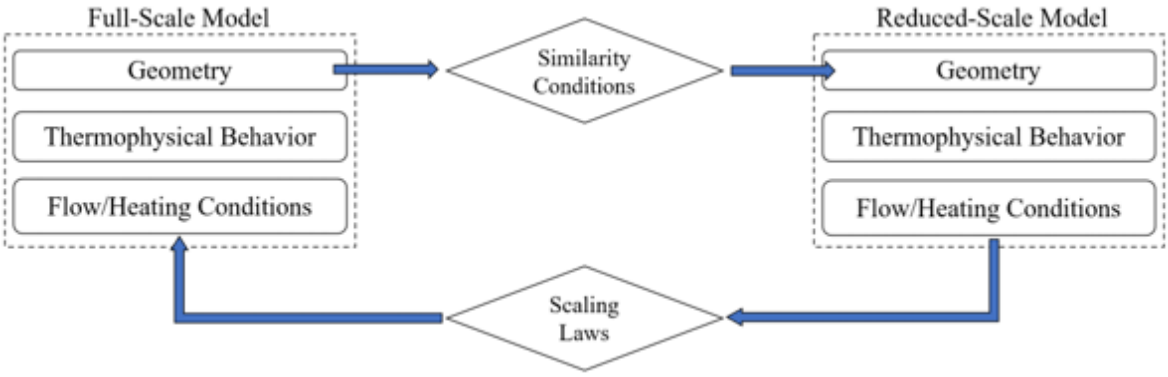

Figure 30. Similitude theory as applied for fluid mechanics and convective heat transfer for this analysis

Applying similitude theory into a given scaling analysis theoretically produces similar behavior at different scales. However, similarity scaling is very sensitive to distortions, which are mainly created due to the thermophysical property differences between the model and prototype fluids. Practically, the only action to reduce the amount of scaling distortion is to optimize its reductions by carefully selecting specific fluids and precisely calculating its requisite flow and heating conditions.

The formal definition of scaling distortion is the fractional difference between the prototype and model in the amount of conserved property transferred through the evolution of a specific process in each module/component during its respective residence time.

The distortion factor ($DF_{j,k}$) can be described as follows:

$$DF_{j,k} = \frac{\left[\boldsymbol{\Pi}_{j,k}\right]_p - \left[\boldsymbol{\Pi}_{j,k}\right]_m}{\left[\boldsymbol{\Pi}_{j,k}\right]_p} \tag{46}$$

where p and m represent the prototype and model, respectively.

Regarding the heat transfer performance, the scaling distortion is defined as:

$$DF_{Nu} = \frac{Nu_{FLiBe} - Nu_{DowthermA}}{Nu_{FLiBe}} \tag{47}$$

Chapter 5: Numerical Results and Discussion

Numerical simulations were performed to analyze the effects of Re and Pr on the Nu and ΔP for flowing FLiBe and Dowtherm-A in a randomly packed pebble bed. The observed Pr values were 19.4, 15.0, 11.9, 9.64, and 7.95, which correlates to T_{in} = 600, 650, 700, 750, and 800°C for FLiBe and T_{in} = 68.1, 92.2, 119.7, 146.8, and 177.8°C for Dowtherm-A. The observed Re was from 500 to 2500 with increments of 250. The low-Re k-ω SST turbulence model with 0.5-mm polyhedral elements and six prism layers were considered sufficient for the investigated behaviors. The same Re and Pr were performed at various reduced length scales (1:1, 0.75:1, and 0.5:1) using Dowtherm-A, and the collected data was then compared to the collected FLiBe data. Nu correlations for a randomly packed pebble bed were developed for FLiBe and Dowtherm-A based on the gathered computational data. A Nu distortion correction factor was developed using the developed Nu correlations.

5-1. Results of FLiBe Cases

The numerical results for all FLiBe cases are presented in Figure 31:

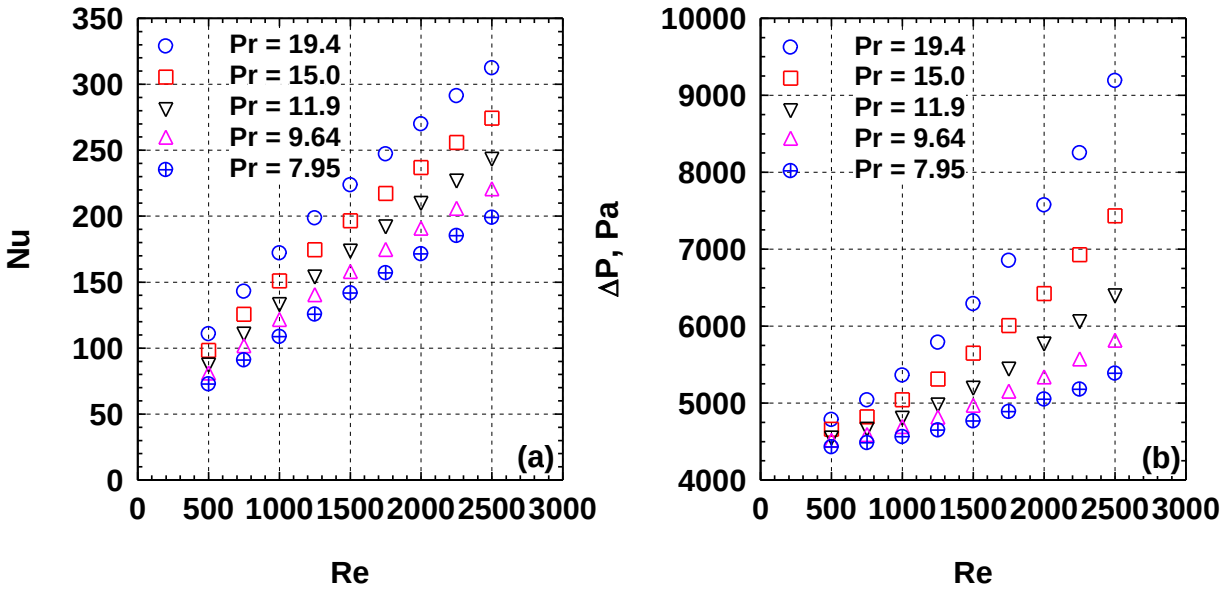

Figure 31. Results of Nu and ΔP for flowing FLiBe for the ranges of 500 < Re < 2500 and 7.95 < Pr < 19.4.

According to Figure 31a, as the Pr was decreased, the Nu also decreased. Also, as the Re was increased, the Nu increased for all investigated Pr. The Nu was reduced by roughly 10-14% for each change in Pr, with reduction change decreasing as Pr was decreased. Since the Re range

is considered laminar, the trend fits previous observations that decreasing Pr would result in decreased Nu. If the Re range was considered turbulent, then as Pr was decreased, Nu would have increased. Regarding ΔP, as the Pr was decreased, the dynamic viscosity (μ) sharply decreased, and the thermal conductivity (k) slightly increased, allowing the flowing FLiBe to maneuver through the test section with lower wall shear stress, resulting in decreased ΔP, as shown in Figure 31b. The ΔP was reduced by roughly 4-12% for each change in Pr, with the reduction change decreasing as Pr decreased. The ΔP observed at the lowest Re of 500 showed about 4-5 kPa across the test bed section, which equates to <1 psi, which is in the same order of magnitude of the Mk-1 PB-FHR technical description.

The temperature and pressure contour of a vertical cross-section of the test section at varying Re and Pr are shown in Figure 32. At higher Re, the temperature profile showed minor temperature variation for all Pr. The core temperature increased linearly as the coolant moved from the bottom of the core to the top. The temperature profile of each pebble showed higher temperatures on the upper half of each pebble due to the separated flow generated around each pebble, causing localized turbulence. These wakes captured better heat transfer, resulting in hot spots occurring more frequently on the upper half of each pebble. Regarding the ΔP, the ΔP increased as the Re increased and decreased as Pr decreased.

5.1.1. Comparison with Established Correlations

Nusselt Number:

Previously established Nu correlations were collected and summarized in Table 17. All previously established correlations except for the Kim correlation were performed using common low-Pr fluids such as water or helium. The Kim correlation, which was developed using FLiBe, states that the existing correlations significantly overestimates the Nu for FLiBe. However, the method used to calculate the Nu using Kim's method was not mentioned in their work. It is speculated that the method of calculating Re and Nu was based on D_{cyl} and not D_p. Since the majority of the known correlations based Re and Nu off of D_p and not D_{cyl}, the same was done for this study. A comparison of the shown correlations with the Pr = 15.0 for FLiBe is shown for the investigated Re range in Figure 33.

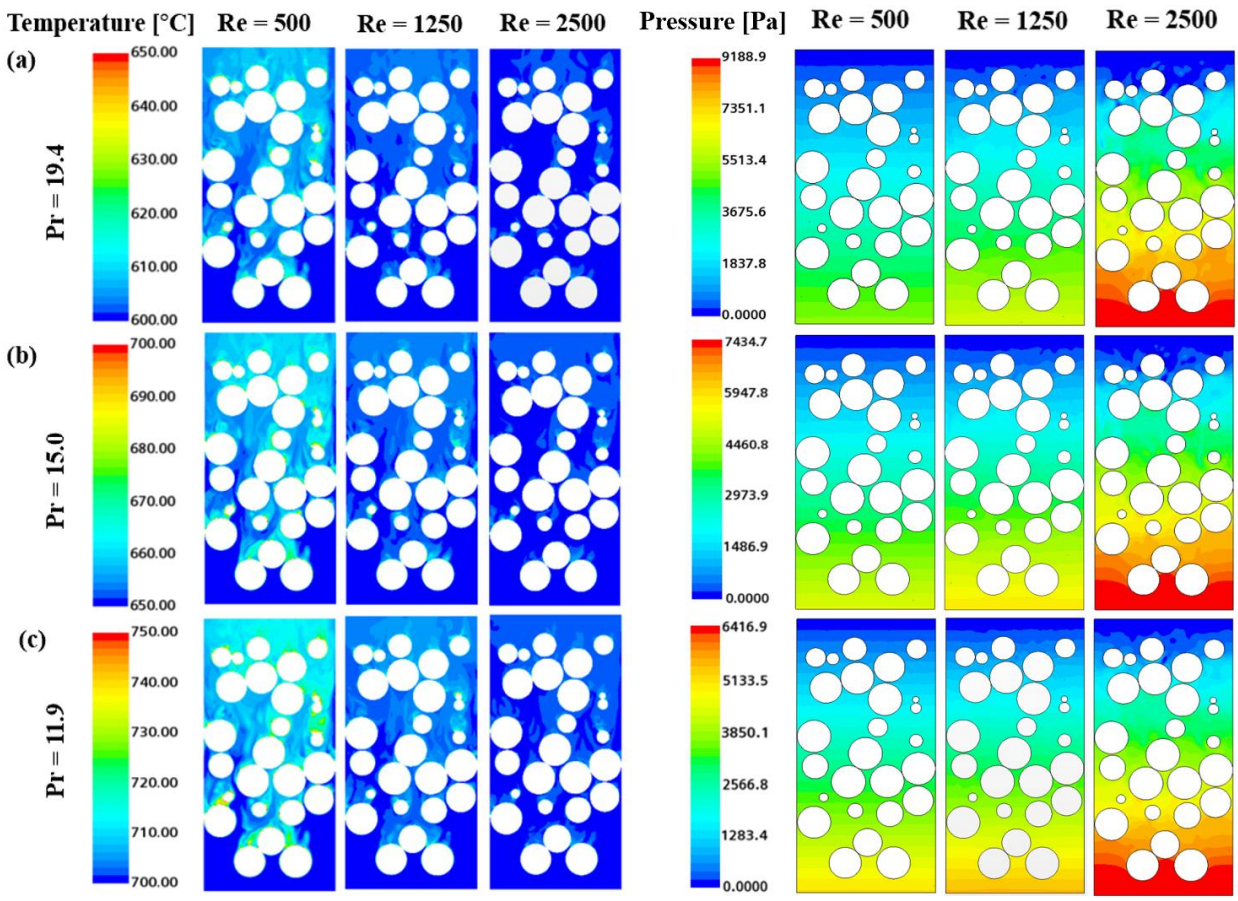

Figure 32. Temperature and pressure contour of a vertical cross-section of test section at various Re and Pr.

Table 17. List of Nu correlations applicable to investigated Re and Pr ranges from this study.

Nu Correlation		Available ranges	Coolant
Wakao and Kaguei, 1982	$Nu = 2 + 1.1{Re_p}^{0.6}Pr^{1/3}$	$15 \leq Re_p \leq 8500$ $0.7 \leq Pr \leq 1$	Gases
Kunii and Levenspeil, 2013	$Nu = 2 + 1.8{Re_p}^{0.5}Pr^{1/3}$	$Re_p \geq 50$	Gases
Meng, 2013	$Nu = 3.212{Re_p}^{0.335}Pr^{1/3}$	-	Water
Satterfield and Resnick, 1954	$Nu = 0.922{Re_p}^{0.66}Pr^{1/3}$	$Re_p \geq 10$	Gases
Eckert and Drake, 1987	$Nu = 0.8{Re_p}^{0.7}Pr^{1/3}$	$Re_p \geq 500$	Gases
Kim, 2019	$Nu = 0.016Re^{0.72}Pr^{0.31}$	$2025 < Re < 17150$, $2.58 \leq Pr \leq 19.08$	FLiBe

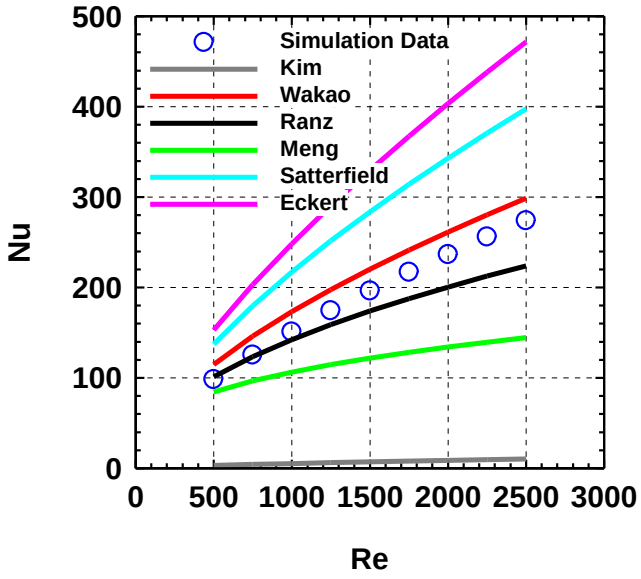

Figure 33. Comparison of various Nu correlations to current simulation data for Pr = 15.0.

By comparing various Nu correlations with the simulation data, the Wakao correlation was shown to have the closest trend to the simulation data from the analysis. The Wakao correlation is currently the most commonly used correlation for calculating Nu for PB-FHR cores with FLiBe as the coolant [61-63]. This correlation was also mentioned in the Technical Description of the Mk-1 PB-FHR as the correlation to predict the heat transfer coefficient [4]. The Wakao correlation states:

$$Nu = 2 + 1.1Re^{0.6}Pr^{1/3} \tag{48}$$

where Re is the Reynolds number based off D_p and Pr is the Prandtl number evaluated at the inlet temperature [24]. To observe the difference between the Wakao correlation and the collected computational data from this analysis, the highest and lowest Pr (Pr = 19.4 and 7.95) were plotted for 500 < Re < 2500 alongside the Wakao correlation, as shown in Figure 34.

According to Figure 34, roughly 11.3% error was observed at the highest Pr (T_{in} = 600°C), and roughly 23.4% error was observed at the lowest Pr (T_{in} = 800°C). Though similar trends can be observed using the Wakao correlation, as stated in Table 17, the Wakao correlation was created for gas-cooled pebble bed reactors, which utilized Helium as its target fluid. The Wakao correlation was built using several experimental data sets observed at steady and non-steady states using only low-Pr fluids. The Wakao correlation was developed by fitting all the experimental data across a wide range of Re and Pr. To observe whether the collected data from this study falls within the

boundaries of the data used for the Wakao correlation, all experimental data sets used in developing the Wakao correlation were plotted alongside the collected data, as shown in Figure 35. Since the Wakao correlation was developed by fitting several experimental, the maximum uncertainty of all data sets showed a roughly +169% and -48% difference from the developed correlation. The simulation data generated from this study falls right below the correlation curve fit, with the observed maximum difference being about -23.4% for the entire investigated Re and Pr ranges.

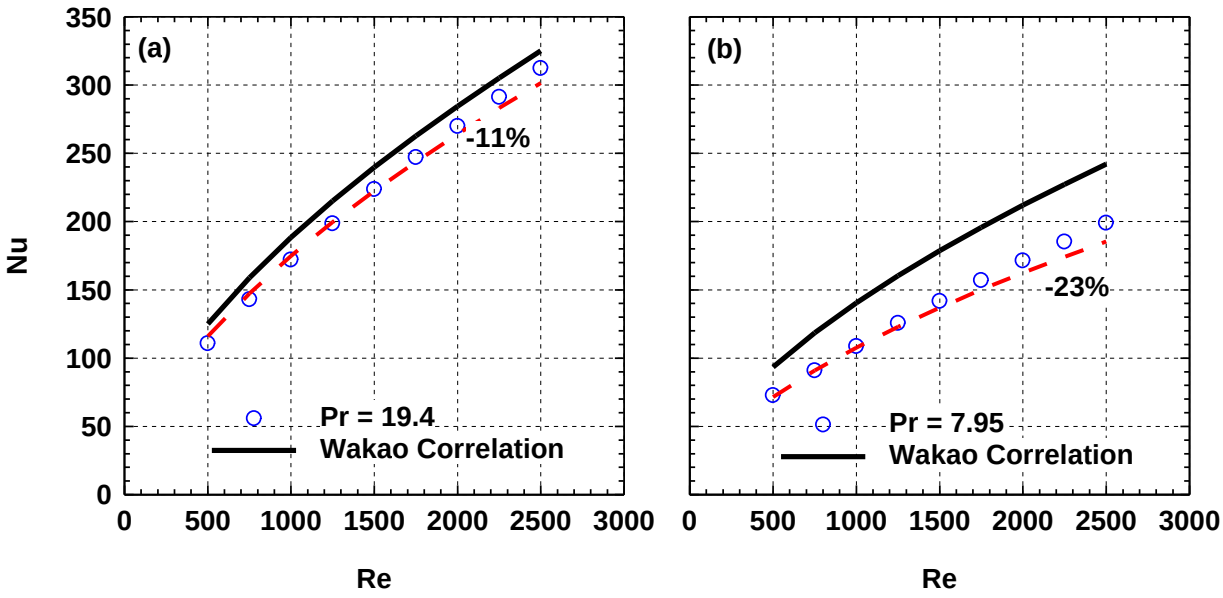

Figure 34. The Nu relative error when compared to the Wakao correlation increases as the core temperature increases.

ΔP and f:

All previous correlations were developed using low-Pr fluids such as air, water, and helium. Additionally, practically all experiments were only intended to observe the hydrodynamic behavior of the pebble bed core, and heat transfer was not considered in the development of each correlation. Since there is no publicly available literature regarding the change in ΔP and f with varying Re and Pr for FLiBe in a heated PB-FHR core, the only way to validate the collected data from this analysis would be to experiment with the exact dimensions and with each pebble in the analysis having a constant surface heat flux. Additionally, as explained in Section 3.4, the number of pebbles in the computational analysis showed to contribute roughly 63-64 Pa of ΔP per pebble, thus N = 75 pebbles are just an arbitrary number chosen to obtain a steady-state Nu and ΔP is

directly affected by how many pebbles are in the analysis. Comparisons between the collected data and previous correlations are plotted in Figure 36.

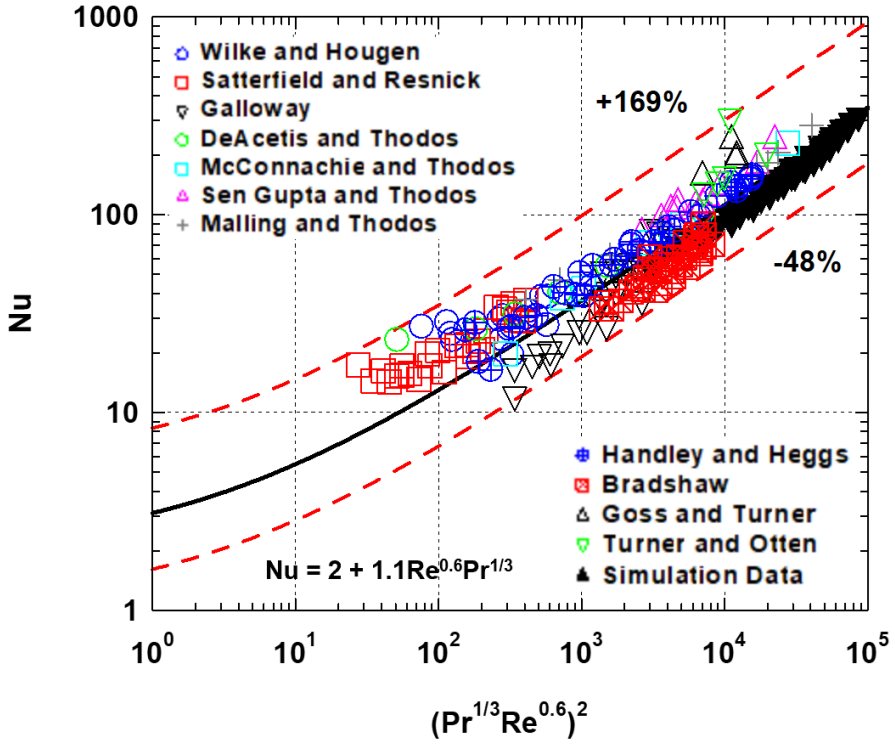

Figure 35. Development of Nu correlation using several experimental data sets. The top legend represents solutions at steady-state, and the bottom legend represents unsteady-state solutions. The data collected for this analysis are compared with all data sets.

To convert ΔP to f for packed beds, the following equation was used [64]:

$$f = \frac{\Delta P}{L} \frac{d_p \varepsilon^3}{\rho u^2 (1-\varepsilon)} \tag{49}$$

where L is the height of the bed, μ is the fluid viscosity, ε is the void fraction, u is the superficial fluid velocity, D_p is the diameter of a pebble, and ρ is the density of the fluid.

According to Figure 36, at the lowest Re of 500, the ΔP and f observed using FLiBe were shown to be about five times higher than the correlations. Only speculations can be made about the deviating phenomenon since there is no way to prove this except by performing experimental analyses. A significant possibility for the incongruity could be the differences in thermophysical properties between FLiBe and the low-Pr fluids used in the development of all the mentioned correlations. Since the flow resistance in flow through any porous medium is the sum of viscous contributions and inertial contributions, the significant difference in viscosity between FLiBe and

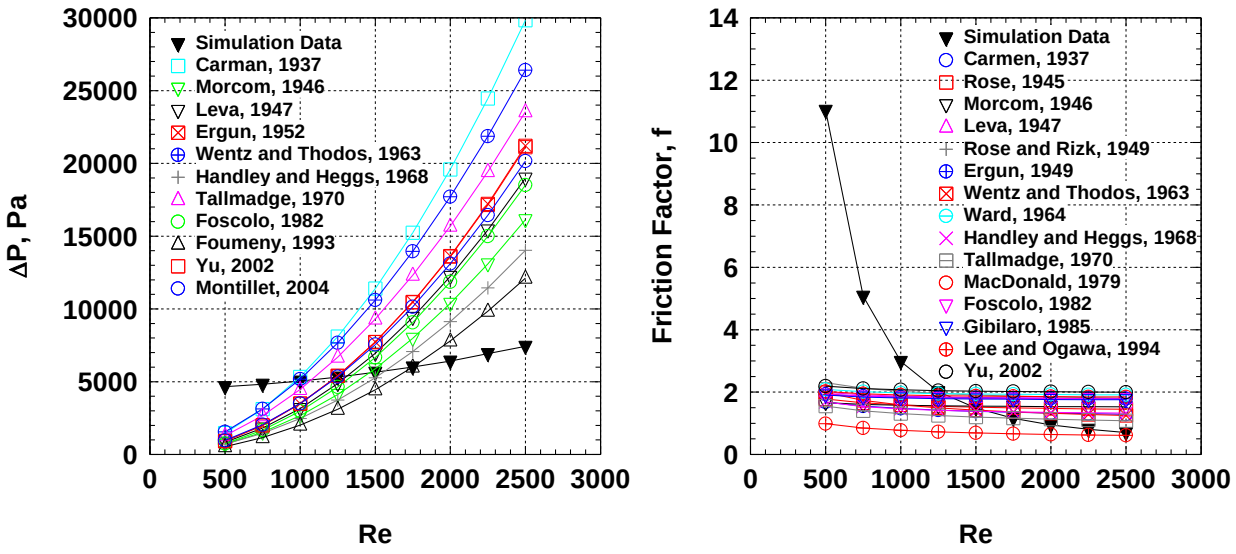

Figure 36. Comparison of collected ΔP and f data for N = 75 pebbles and Pr = 15.0 with previous pebble bed correlations developed for low-Pr fluids.

the low-Pr fluid can explain the significant uptake in ΔP and f at low Re. Other possible reasons for the discrepancies between the collected data and established correlations can be the porosity analyzed, Re ranges observed, size of pebbles used, and dimensional ratios of D_p/D_{cyl}.

5.1.2. Development of FLiBe Nu Correlation

Since similar behavior was observed between the numerical data and the Wakao correlation, the Nu correlation for FLiBe was created in the following form:

$$Nu = aRe^{b}Pr^{c} \tag{50}$$

To create the Nu correlation, the Pr was plotted against $Nu/Re^{0.6}$ and fitted using the power-law form $y = ax^{b}$, as shown in Figure 37a. The $Re^{0.6}$ was chosen to match the Re exponent of the Wakao correlation. By fitting the data, the resulting power-law fit was as follows:

$$\frac{Nu}{Re^{0.6}} = 0.633Pr^{0.499} \tag{51}$$

which can be rearranged to achieve the following correlation:

$$Nu = 0.633Re^{0.6}Pr^{0.5} \tag{52}$$

The proposed correlation for the Nu is for the range of $500 < Re < 2500$ and $7.95 < Pr < 19.4$ with a R^2 value of 0.979. By plotting the Nu correlation versus the Nu numerical data, the overall correlation showed ±5% difference over the investigated Re and Pr range, as shown in Figure 37b. The correlation was then plotted alongside the simulation data, as shown in Figure 38.

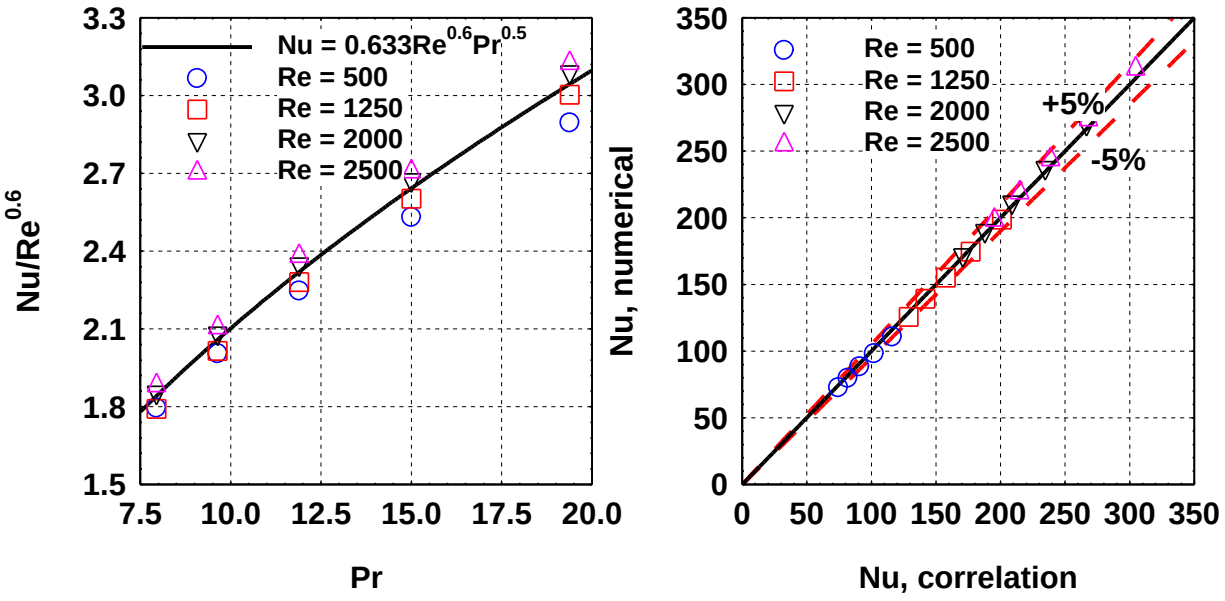

Figure 37. Development of FLiBe Nu correlation in a randomly packed pebble bed for the range of 500 < Re < 2500 and 7.95 < Pr < 19.4.

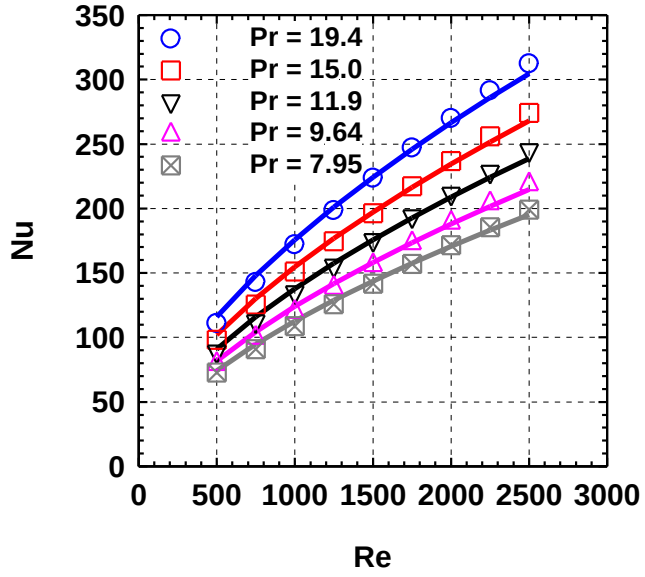

Figure 38. Nu data comparison between collected simulation data (marker) and developed correlation (line).

5-2. Results of Dowtherm-A Cases

Using the similarity scaling analysis results, the requisite flow and heat conditions were determined for a PB-FHR at different length scales using the surrogate fluid Dowtherm-A. Simulations were then performed using the same ranges of 500 < Re < 2500 and 7.95 < Pr < 19.4 used in the FLiBe cases. The exact number of elements used for the FLiBe cases (23.9 million

elements) were used for all analyses. The Nu numerical results for Dowtherm-A at various length scales are shown in Figure 39a-c.

As expected, the Nu behavior of Dowtherm-A showed similar trends to the simulation data for FLiBe. The trends for Dowtherm-A showed increased Nu as Re increased and decreased Nu as Pr decreased. For all investigated length scales, the Nu showed similar behavior, even with the different flow and heating conditions. There is a slight decrease in the Nu as the length scale was reduced, with the maximum difference of +7.7% occurring at the lowest Re of 500.

The ΔP results for Dowtherm-A at various length scales are shown in Figure 39e-f. For the lower Re values, as the length scale decreased, the ΔP also decreased at a linear rate. However, deviating behavior was observed as the Re increased between length scales. The severity of the changing ΔP as Re increases was higher between the 0.75:1 and 0.5:1 scale than between the 1:1 and 0.75:1 scale. Additionally, the ΔP difference between the Pr = 9.64 and 7.95 was much lower than the higher Pr. As the length scale is decreased, the observed ΔP showed a much higher increase as the Re increased. This stark increase in ΔP is likely due to the change in cross-section size. Assuming the flow channel to be empty, a decrease in the diameter of the test section would result in higher pressures needed to drive through the fluid. Though the porosity of the test bed and the active height to diameter ratio are the same for each length scale, the combination of higher pressures needed to drive the fluid upward and the increasing effects of gravity could be some of the main reasons as to why the 0.5:1 scale ΔP had such a significant increase as Re increased.

5.2.1. Development of Dowtherm-A Nu Correlation

A general Nu correlation was developed for Dowtherm-A in a randomly packed bed using the same form used to develop the FLiBe Nu correlation (Eq. 50). The correlation is independent of the length scale factor and is applicable for the same ranges used for the FLiBe cases, namely $500 < Re < 2500$ and $7.95 < Pr < 19.4$. The correlation was created by averaging the Pr exponent over the three length scales. In Figure 40a, the data points for Re = 500, 1250, 2000, and 2500 were plotted for each length scale at each Pr and fitted.

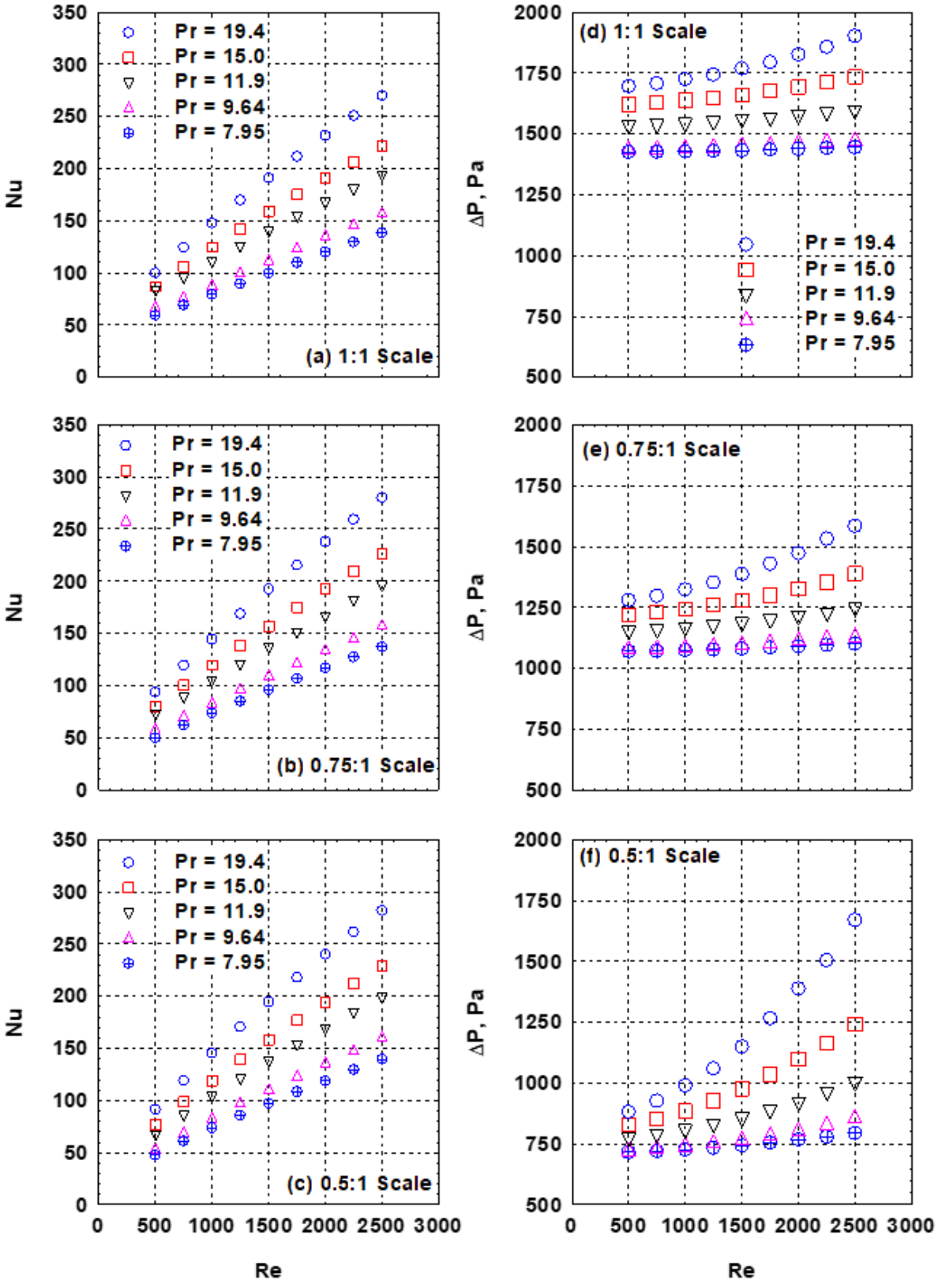

Figure 39. Results of Nu and ΔP for Dowtherm-A for 500 < Re < 2500 and 7.95 < Pr < 19.4.

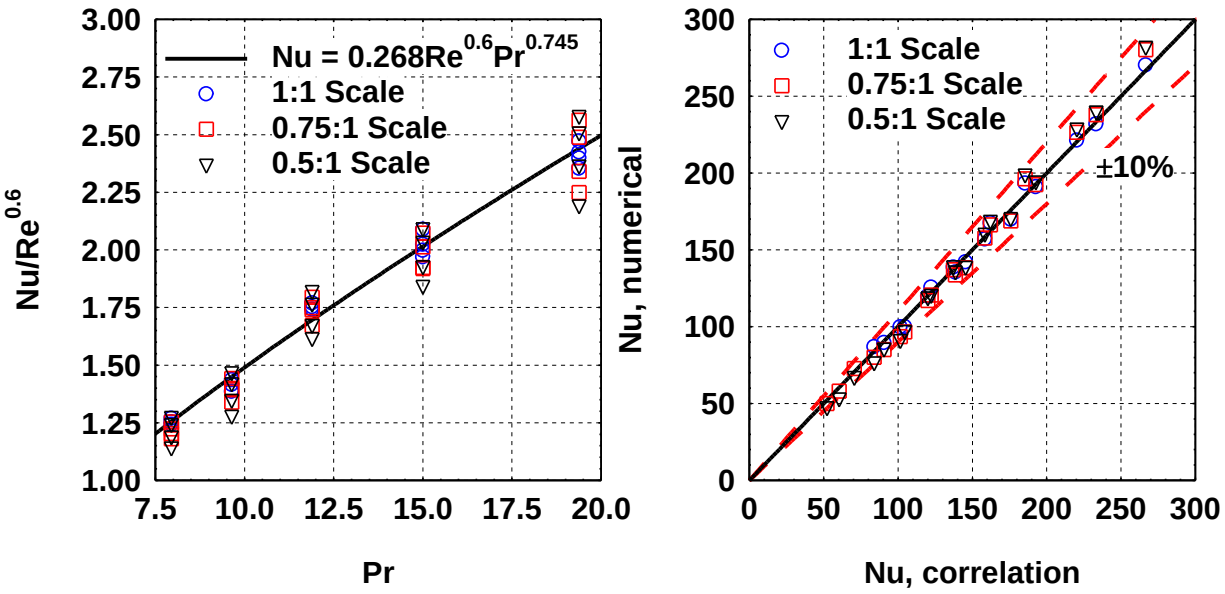

Figure 40. Development of Nu correlation for all investigated length scales (1:1, 0.75:1, and 0.5:1).

The resulting Nu correlation for Dowtherm-A in a randomly packed pebble bed is:

$$Nu = 0.268Re^{0.6}Pr^{0.745} \tag{53}$$

The Nu correlation was compared with the numerical data, showing good agreement with the numerical data with a ±10% difference over the investigated Re and Pr, as shown in Figure 40b. The correlation was then plotted alongside the Dowtherm-A data for all length scales, as shown in Figure 41. The maximum difference was observed at the highest Re.

5-3. Comparative Analysis between FLiBe and Dowtherm-A

Under the scaled geometrical, flow, and heating parameters, the inherent distortion calculated at various length scales showed little to no variation. The average distortion percentage between all reduced length scales at the highest Pr showed roughly -14% distortion and at the lowest Pr showed roughly -30%, as shown in Figure 42. Thus, if a small-scale experiment were to be performed using the same conditions, the heat transfer performance of the surrogate fluid would perform roughly 14% lower than FLiBe at Pr = 19.4 and roughly 30% lower at Pr = 7.95.

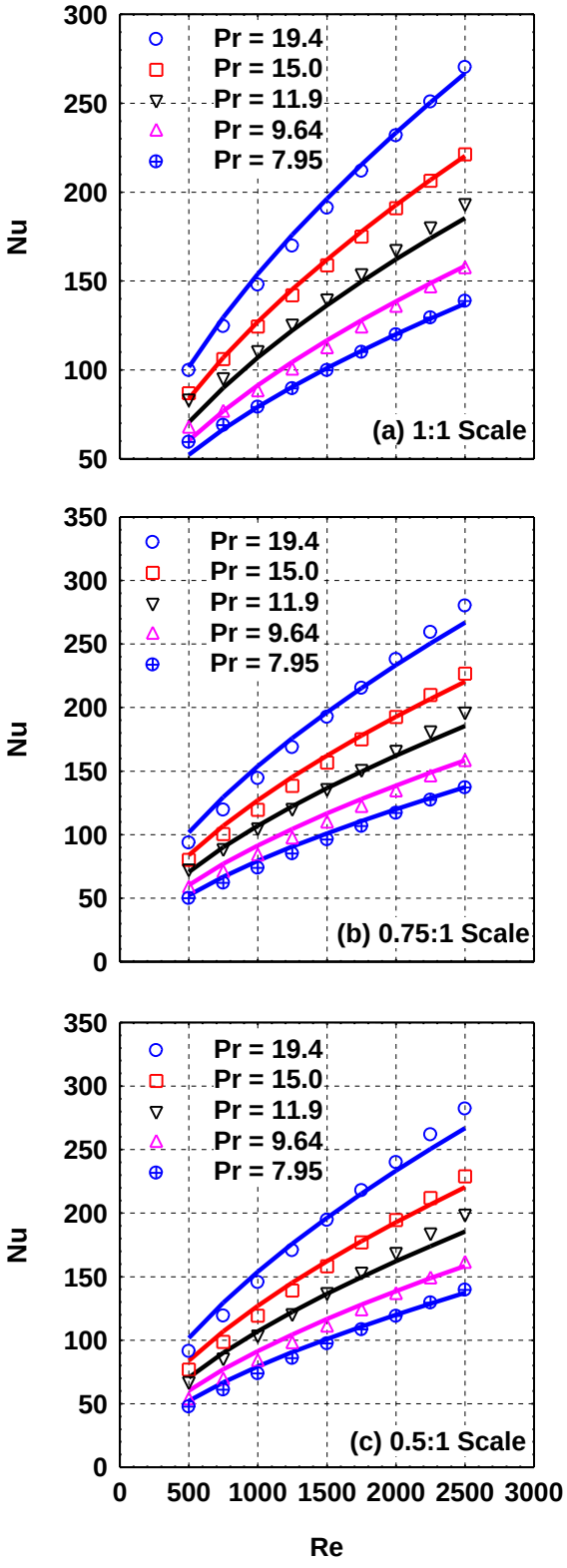

Figure 41. *Nu* data comparison between collected simulation data (marker) and developed correlation (line) for all investigated length scales.

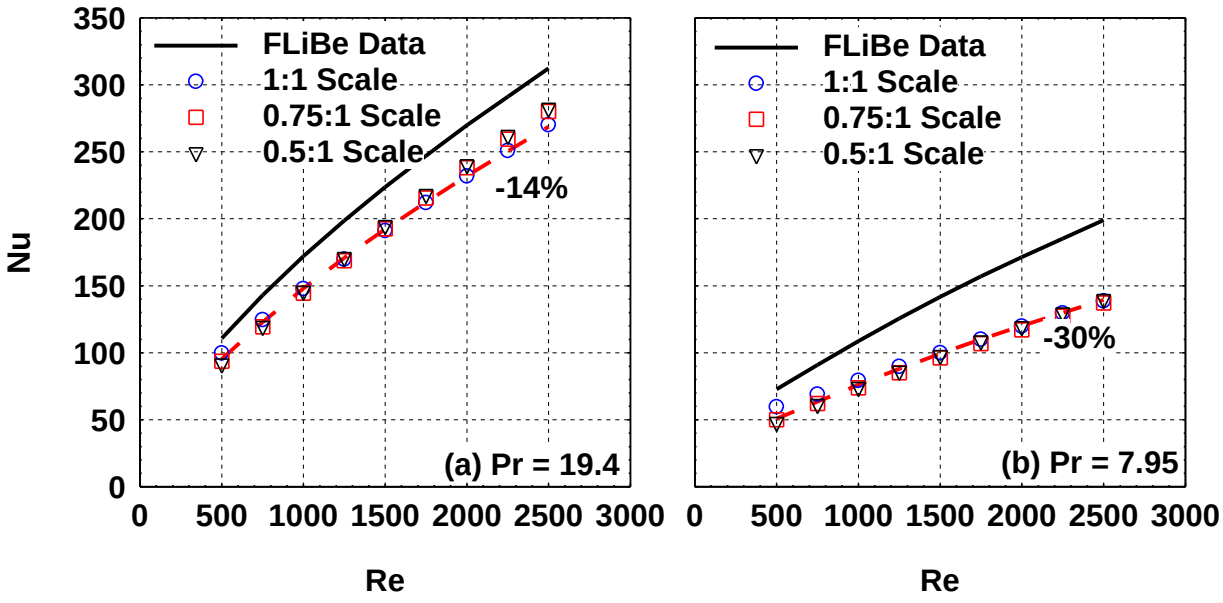

Figure 42. Comparison between all reduced length scales and FLiBe showed similar distortion levels for all investigated Pr.

5-4. Development of Nu Distortion Correction Factor

In a given experiment involving surrogate fluids, a certain degree of distortion is inherently present regardless of how precise the requisite conditions were made. Regarding the inherent distortion observed between FLiBe and Dowtherm-A, at Pr = 19.4, the distortion was about 14%, and at Pr = 7.95, the distortion was about 30%. If Dowtherm-A were to be experimentally investigated in a heated pebble bed test section akin to the Mk-1 PB-FHR core with correctly reduced power and flow conditions and possibly reduced length scale, then the Nu data results would be roughly lower by 14% if FLiBe was instead used.

To develop the Nu distortion factors, the two correlations developed for FLiBe and Dowtherm-A were set equal to each other, and a distortion correction factor (Ψ) was introduced:

$$0.633\mathrm{Re}^{0.6}\mathrm{Pr}^{0.5} = 0.268\mathrm{Re}^{0.6}\mathrm{Pr}^{0.745}\,\Psi \tag{54}$$

Since the Re exponent was fixed to 0.6, the correction factor is independent of the flow conditions. The distortion correction factor can be simplified to:

$$\Psi = \frac{0.633\mathrm{Pr}^{0.5}}{0.268\mathrm{Pr}^{0.745}} \tag{55}$$

which can then be described as a function of Pr. The Nu distortion factor for Dowtherm-A is:

$$\Psi = 2.362\mathrm{Pr}^{-0.245} \tag{56}$$

The FLiBe Nu data results and the Dowtherm-A Nu data results at various length scales for the highest and lowest Pr values with the introduced distortion correction factor are shown in Figure 5.14. At Pr = 19.4, the observed difference between the FLiBe and Dowtherm-A data with the correction factor was about ±2%, and at Pr = 7.95, the observed difference was ±8%.

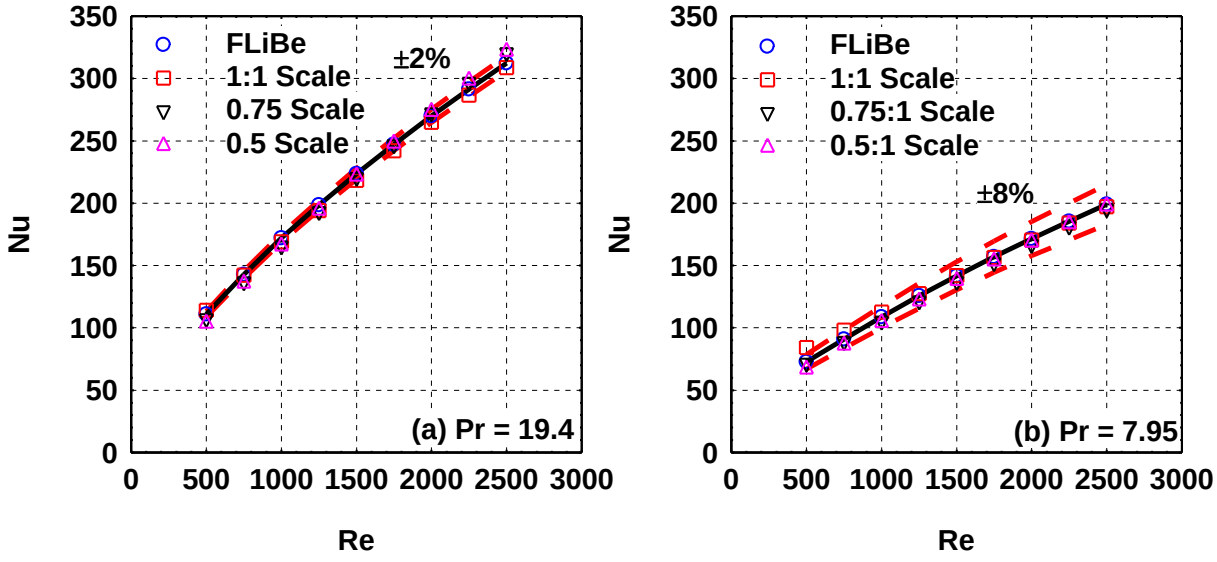

Figure 43. Comparison between FLiBe Nu data results and Dowtherm-A Nu data results with the introduced distortion correction factor.

Chapter 6: Conclusion and Future Work

6-1. Summary of Results

In this analysis, computational simulations were performed to quantify the inherent distortion present in the similarity scaling between FLiBe and Dowtherm-A for a randomly packed pebble bed akin to the Mk-1 PB-FHR core. The optimal geometrical flow path design characteristics of the randomly packed pebble bed were identified for the realistic approach, in which every single pebble in a given simulation was meshed individually to be post-processed individually. The chosen method was the gap method, in which the size of each pebble was not reduced but merely shifted in position to create an artificial gap. The effects of the mesh size/approach and the minimal gap size between pebbles were investigated, resulting in a base element mesh size of 0.5-mm with 100% relative prism layer thickness and 0.005-mm minimal gap size between pebbles to be sufficient for calculating the Nu. The effects of the number of pebbles were then investigated for both the Nu and ΔP with the chosen mesh specifications and minimal gap size. It was concluded that 75 pebbles were a sufficient number of pebbles that can produce a converged Nu, and that a further increase in the number of pebbles was unnecessary. The numerical data collected for FLiBe was validated against q-DNS validated LES data sets, showing <1% error with the k-ω SST turbulence model.

The flow and heating conditions for FLiBe were identified for $500 < Re < 2500$ and $7.95 < Pr < 19.4$ using the core dimensions and thermophysical properties of FLiBe. The thermophysical properties for both FLiBe and Dowtherm-A were obtained through INL reports, with each needed thermophysical property (ρ, μ, C_p, k) being a function of temperature only. By matching the Pr between FLiBe and Dowtherm-A using the two thermophysical property data sets, the respective inlet core temperature for each investigated Pr was calculated for Dowtherm-A. Similarity scaling techniques were then utilized to identify the requisite flow and heating conditions needed to reproduce the same theoretical Nu for FLiBe with Dowtherm-A. The similarity scaling analyses produced flow and heating conditions for Dowtherm-A in a randomly packed pebble bed for three different length scales, namely 1:1 (full scale), 0.75:1, and 0.5:1. Computational simulations for both FLiBe and Dowtherm-A were performed for the aforementioned Re and Pr ranges.

The FLiBe Nu data showed similar trends to the Wakao correlation, which is currently the recommended Nu correlation for PB-FHR cores. The maximum difference for the highest Pr was -11%, and for the lowest Pr was -23%. Since the Wakao correlation was developed only using several experimental data sets for low-Pr fluids in a pebble bed core, a Nu correlation was developed for FLiBe using the collected simulation data. The resulting correlation, $Nu = 0.633Re^{0.6}Pr^{0.5}$ for 500 < Re < 2500 and 7.95 < Pr < 19.4, showed good agreement with the numerical data, showing $\pm$5% error. Comparison between the Dowtherm-A data of the three different length scales showed that for all investigated length scales, the Nu displayed similar behavior despite having distinctly different flow and heating conditions between each length scale. The maximum difference between the three Dowtherm-A data sets was $\pm$7.7% error, observed at Re = 500 and Pr = 19.4. For all investigated length scales, it was concluded that the slight variation in Nu between length scales was more prevalent at the lowest Re. The slight variation between length scales at the lowest Re was most likely due to the viscous wall effects being more prevalent at lower Re and higher Pr. Similar to the FLiBe Nu correlation developed in this analysis, a Nu correlation for Dowtherm-A was developed for the same Re and Pr ranges using the three-length scale data sets, resulting in a Nu independent of length scale. The Nu correlation for Dowtherm-A, $Nu = 0.268Re^{0.6}Pr^{0.745}$ for 500 < Re < 2500 and 7.95 < Pr < 19.4, which also showed good agreement with the numerical data, with $\pm$10% error being observed.

Comparison between the FLiBe and Dowtherm-A data sets showed similar distortion values for all investigated length scales. The maximum percentage difference between FLiBe and Dowtherm-A for the highest Pr was -14% and for the lowest Pr was -30%. So, if a small-scale experiment were to be performed using the exact conditions determined from this analysis, then the heat transfer performance of the surrogate fluid would perform roughly 14% lower than FLiBe for Pr = 19.4 and roughly 30% lower than FLiBe at Pr = 7.95. Using the developed *Nu* correlations for both FLiBe and Dowtherm-A, a Nu distortion correction factor (Ψ) was developed, resulting in $\Psi = 2.362Pr^{-0.245}$. Thus, if Dowtherm-A was experimentally investigated for a PB-FHR core with correctly reduced power and flow conditions, then the data results of the *Nu* can be multiplied by this distortion factor to achieve similar results to FLiBe. By implementing the developed *Nu* distortion correction factor into the Dowtherm-A data sets, roughly $\pm$2% error at Pr = 19.4 and $\pm$8% error at Pr = 7.95 from the FLiBe numerical data results was observed.

6-2. Future Work

Though the Mk-1 PB-FHR preconceptual design has only acted as a precursor to actual commercial reactor designs such as the KP-FHR, the Nu correlations for both FLiBe and Dowtherm-A provide a firm basis for future investigations into PB-FHR technologies. By refining the similarity scaling process to involve the Hierarchical Two-Tiered Scaling (H2TS) Methodology, the natural circulation phenomena in the pebble bed reactor core can be measured, and the contribution of the radiative heat transfer can be quantified. Other potential surrogate fluids can also be investigated under requisite conditions to FLiBe and compared with the Dowtherm-A data sets and various length scales to either recognize its validity and suitability or disprove its usage as a surrogate fluid for FLiBe. Finally, a small-scale experimental facility of the pebble bed core can be created to validate the numerical data presented in this analysis officially. A simple diagram of the basic structure and part of such a setup is provided in Figure 43.

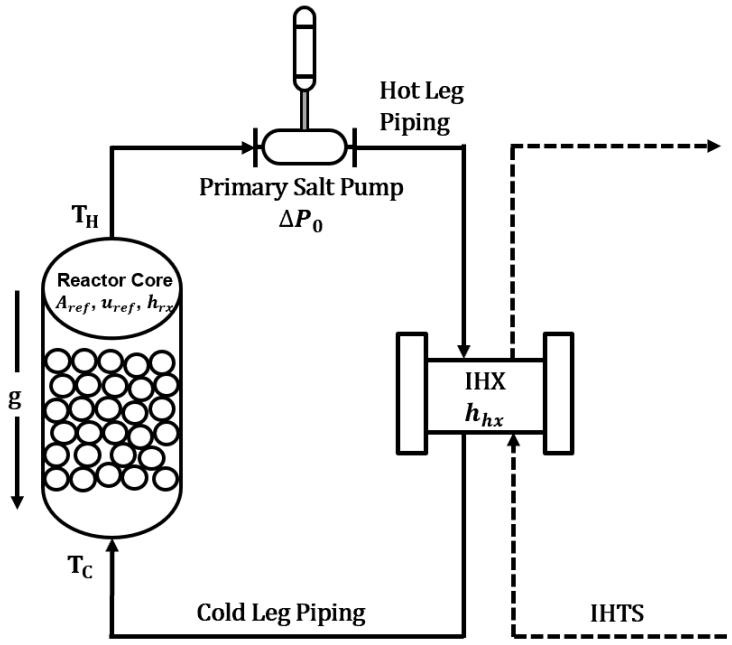

Figure 44: Simple schematic of potential heat transfer facility for experimentally quantifying the thermal-hydraulic behavior of a PB-FHR core.

6-3. Conclusion

Thermal hydraulic similarity scaling is a powerful tool allowing researchers to bypass complications associated with the coolant in question through surrogate fluids. By ensuring the flow and heating conditions are calculated correctly, similar thermal and hydrodynamic behavior(s) akin to the actual reactor coolant can be observed independent of the length scale using

the appropriate simulant fluid. However, though being theoretically analogous, similarity scaling inherently produces some form of inherent distortion. Despite the inevitability of such deviating phenomena, the determination of the level of distortion over a specified range can help justify the reasoning between incongruities between the coolant and surrogate fluid. With the increasing amount of research endeavors into reactor core thermal hydraulics, similarity scaling will continue to be an essential tool in moving forward novel reactor technological systems.

6-4. List of Publications

- Wahlquist, S., Ali, A., 2022, "Similarity Scaling Effects on the Heat Transfer Behavior of a Randomly Packed PB-FHR Core Using a Surrogate Fluid," (Journal article under review).

- Wahlquist, S., Ali, A., 2021, "Numerical Study of the Heat Transfer in Randomly Packed Spheres for Fluoride Salt Cooled High-Temperature Reactors (FHRs)," *ANS Computational Thermal Hydraulics – III*, 811-814; dx.doi.org/10.13182/T124-35255.

References

[1] Bardet, P. M., Peterson, P. F., 2008, "Options for Scaled Experiments for High Temperature Liquid Salt and Helium Fluid Mechanics and Convective Heat Transfer," *Nucl. Tech.*, 163:3, 344-357; https://doi.org/10.13182/NT163-344.

[2] Morris, R. N., Petti, D.A., Powers, D. A., Boyack, B.E., Rubin, M.B., 2004, "TRISO-coated Particle Fuel Phenomenon Identification and Ranking Tables (PIRTs) for Fission Product Transport Due to Manufacturing, Operations, and Accidents," NUREG/CR-6844, 1(2), 1-4.

[3] Andreades, C., Cisneros, A. T., Choi, J. K., Chong, A.Y.K., Fratoni, M., Hong, S., Huddar, L. R., Huff, K. D., Kendrick, J., Krumwiede, D. L., Laufer, M. R., Munk, M., Scarlat, R. O., Zweibaum, N., 2016, "Design Summary of the Mark-1 Pebble-Bed Fluoride Salt-Cooled, High-Temperature Reactor Commercial Power Plant," *Nucl. Tech.*, 195:3, 223-238; https://doi.org/10.13182/NT16-2.

[4] Andreades, C., Cisneros, A. T., Choi, J. K., Chong, A. Y. K., Fratoni, M., Hong, S., Huddar, L. R., Huff, K. D., Krumwiede, D. L., Laufer, M. R., Munk, M., Scarlat, R. O., Zweibaum, N., Greenspan, E., Peterson, P. F., 2014, "Technical Description of the "Mark 1" Pebble-Bed Fluoride-Salt-Cooled High-Temperature Reactor (PB-FHR) Power Plant," UCBTH-14-002 NEUP.

[5] Guardo, A., Coussirat, M., Larrayoz, M. A., Recasens, F., Egusquiza, E., 2004, "CFD Flow and Heat Transfer in Nonregular Packings for Fixed Bed Equipment Design," *Ind. Eng. Chem. Res.*, 43, 22, 7049-7056; DOI:10.1021/ie034229+.

[6] Ferng, Y. M., Lin, K.-Y., 2013, "Investigating effects of BCC and FCC arrangements on flow and heat transfer characteristics in pebbles through CFD methodology," *Nucl. Eng. Des.*, 258, 66-75; https://doi.org/10.1016/j.nucengdes.2013.02.009.

[7] Hassan, Y. A., 2008, "Large eddy simulation in pebble bed gas cooled core reactors," *Nucl. Eng. Des.*, 238:3, 530-537; https://doi.org/10.1016/j.nucengdes.2007.02.041.

[8] Chen, L., Lee, J., 2020, "Effect of pebble diameters on the heat transfer characteristics of a structured pebble bed in an HTGR," *Energy*, 212, 118642; https://doi.org/10.1016/j.energy.2020.118642.

[9] Kim, S. G., Addad, Y., Liu, M., Lee, J. I., Lee, Y., 2019, "Computational investigation into heat transfer coefficients of randomly packed pebbles in flowing FLiBe*," Int. J. Heat Mass Transf.*, 145, 118769; https://doi.org/10.1016/j.ijheatmasstransfer.2019.118769.

[10] Choi, D., Park, S., Han, J., Ahn, M-Y., Lee, Y., Park, Y-H., Cho, S., Sohn, D., 2019, "A DEM-CFD study of the effects of size distributions and packing fractions of pebbles on purge gas flow through pebble beds," *Fus. Eng. Des.*, 143, 24-34; https://doi.org/10.1016/j.fusengdes.2019.03.068.

[11] Wu, C. Y., Ferng, Y. M., Chieng, C. C., Liu, C. C., 2010, "Investigating the advantages and disadvantages of realistic approach and porous approach for closely packed pebbles in CFD simulation," *Nucl. Eng. Des.*, 240:5, 1151-1159; https://doi.org/10.1016/j.nucengdes.2010.01.015.

[12] Ge, J., Wang, C., Xiao, Y., Tian, W., Qiu, S., Su, G. H., Zhang, D., Wu, Y., 2016, "Thermal-hydraulic analysis of a fluoride-salt-cooled pebble-bed reactor with CFD methodology," *Prog. Nucl. Energy,* 91, 83-96; https://doi.org/10.1016/j.pnucene.2016.01.011.

[13] Derkx, O. R., Dixon, A. G., 1996, "Determination of the fixed bed wall heat transfer coefficient using computational fluid dynamics," *Num. Heat Transf., Part A: Applications,* 29:8, 777-794; https://doi.org/10.1080/10407789608913819.

[14] Logtenberg, S. A., Dixon, A. G., 1998, "Computational fluid dynamics studies of fixed bed heat transfer," *Chem. Eng. Processing: Process Intensification,* 37:1, 7-21; https://doi.org/10.1016/S0255-2701(97)00032-9.

[15] Nijemeisland, M., Dixon, A. G., 2004, "CFD study of fluid flow and wall heat transfer in a fixed bed of spheres," *AIChE J.*, 50:5, 906-921; https://doi.org/10.1002/aic.10089.

[16] Taylor, J. B., Yavuzkurt, S., Baratta, A. J., 2002, "Modeling of the fluid flow and heat transfer in a pebble bed modular reactor core with a computational fluid dynamics code," *ICONE10-22286,* 649-658; https://doi.org/10.1115/ICONE10-22286.

[17] Lee, J-J., Park, G-C., Kim, K-Y., Lee, W-J, 2007, "Numerical treatment of pebble contact in the flow and heat transfer analysis of a pebble bed reactor core," *Nucl. Eng. Des.*, 237:22, 2183-2196; https://doi.org/10.1016/j.nucengdes.2007.03.046.

[18] Bu, S. S., Yang, J., Zhou, M., Li, S. Y., Wang, Q. W., Guo, Z. X., 2014, "On contact point modifications for forced convective heat transfer analysis in a structured packed bed of spheres," *Nucl. Eng. Des.*, 270, 21-33; https://doi.org/10.1016/j.nucengdes.2014.01.001.

[19] Eppinger, T., Seidler, K., Kraume, M., 2011, "DEM-CFD simulations of fixed bed reactors with small tube to particle diameter ratios," *Chem. Eng. J.*, 166:1, 324-331; https://doi.org/10.1016/j.cej.2010.10.053.

[20] In, W. K., Lee, S. W., Lim, H. S., Lee, W. J., 2006, "Three-Dimensional Analysis of the Hot-Spot Fuel Temperature in Pebble Bed and Prismatic Modular Reactors," Trans. Korean Nucl. Soc. Spring Meeting.

[21] Dixon, A. G., Nijemeisland, M., Stitt, E. H, 2013, "Systematic mesh development for 3D CFD simulation of fixed beds: Contact points study," *Comp. Chem. Eng.*, 48, 135-153; https://doi.org/10.1016/j.compchemeng.2012.08.011.

[22] Kuroki, M., Ookawara, S., Street, D., Ogawa, K., 2007, "High-fidelity CFD modeling of particle-to-fluid heat transfer in packed bed reactors," ECCE-6.

[23] Lucas, J., 1989, "Review of Fluoride Glasses," *J. Mater. Sci.*, 24, 1-13.

[24] N. Wakao, S. Kaguei, 1982, "Heat and Mass Transfer in Packed Beds," first ed., Gordon and Breach Science Publishers, New York.

[25] R. H. Pletcher, J. C. Tannehill, D. A. Anderson, 2013, "Computational Fluid Mechanics and Heat Transfer," third ed., Taylor & Francis Group, Florida.

[26] Liu, M., Lee, Y., Rao, D. V., 2018, "Development of effective thermal conductivity model for particle-type nuclear fuels randomly distributed in a matrix," *J. Nucl. Mater.*, 508, 168-180; https://doi.org/10.1016/j.jnucmat.2018.05.044.

[27] Celik, I. B., Ghia, U., Roache, P. J., Freitas, C. J., Coleman, H., Raad, P. E. (2008) "Procedure for Estimation and Reporting of Uncertainty Due to Discretization in CFD Applications," *J. Fluid Eng.*, 130(7), 078001; https://doi.org/10.1115/1.2960953.

[28] Cohen, S. I., Jones, T. N., 1954, "A Summary of Density Measurements on Molten Fluoride Mixtures and a Correlation for Predicting Densities of Fluoride Mixtures," Technical Report ORNL-1702(Del.); https://www.osti.gov/biblio/4334794.

[29] Cohen, S. I., Powers, W. D., Greene, N. D., 1956, "A Physical Property Summary for Fluoride Mixtures," Technical Report ORNL-2150(Del.); https://www.osti.gov/biblio/4307984.

[30] Cantor, S., 1968, "Physical Properties of Molten-Salt Reactor Fuel, Coolant, and Flush Salts," Technical Report ORNL-TM-2316; https://doi.org/10.2172/4492893.

[31] Hoffman, H. W., Lones, J., 1955, "Fused Salt Heat Transfer Part II: Forced Convection Heat Transfer in Circular Tubes Containing NaF-KF-LiF Eutectic," Technical Report ORNL-1777; https://doi.org/10.2172/4016896.

[32] Douglas, T. B., Payne, W. H., 1969, "Measured enthalpy and derived thermodynamic properties of solid and liquid lithium tetrafluoroberyllate, Li2be4, from 273 to 900 K," *J. Res. Natl. Bur. Stand A Phys. Chem.*, 73A(5) 479-485; DOI: 10.6028/jres.073A.037.

[33] Rao, M. R., 1941, "Thermal Conductivity of Liquids" *Phys. Rev.*, 59, 212; https://doi.org/10.1103/PhysRev.59.212.

[34] Turnbull, A., 1961, "The thermal conductivity of molten salts. I. A transient measurement method," Australian J. Appl. Sci., 12, 30-41, 324-329; http://hdl.handle.net/102.100.100/331678?index=1.

[35] Cornwell, K., "The thermal conductivity of molten salts," *J. Physics D: Applied Physics*, 4(3), 441-445; https://doi.org/10.1088/0022-3727/4/3/313.

[36] Cantor, S., Ward, W. T., Moynihan, C. T., 1969, "Viscosity and Density in Molten BeF2-LiF Solutions," *J. Chem. Phys.*, 50(7), 2874-2879, https://doi.org/10.1063/1.1671478.

[37] Cantor, S., 1973, "Density and Viscosity of Several Molten Fluoride Mixtures," Technical Report ORNL-TM-4308; https://doi.org/10.2172/4419855.

[38] Cooke, J. W., 1973, "Development of the variable-gap technique for measuring the thermal conductivity of fluoride salt mixtures," Technical Report ORNL-4831; https://www.osti.gov/servlets/purl/4556565.

[39] Janz, G. J., Gardner, G. L., Krebs, U., Tomkins, R. P. T., "Molten Salts: Volume 4, Part 1, Fluorides and Mixtures Electrical Conductance, Density, Viscosity, and Surface Tension Data," *J. Phys. Chem. Ref. Data*, 3(1), 1-115; https://doi.org/10.1063/1.3253134.

[40] Gierszowski, P., Mikic, B., Todreas, N., 1980, "Property Correlation for Lithium, Sodium, Helium, Flibe and Water in Fusion Reactor Applications" Technical Report PFC-RR-80-12; http://hdl.handle.net/1721.1/93392.

[41] Janz, G. J., 1988, "Thermodynamic and transport properties for molten salts: correlation equations for critically evaluated density, surface tension, electrical conductance, and viscosity data," *J. Phys. Chem. Ref. Data.*, 17; https://srd.nist.gov/JPCRD/jpcrdS2Vol17.pdf.

[42] Zaghloul, M. R., Sze, D. K., Raffray, A. R., 2003, "Thermo-Physical Properties and Equilibrium Vapor-Composition of Lithium Fluoride-Beryllium Fluoride (2LiF/BeF_2) Molten Salt," *Fus. Sci. Tech.*, 44:2, 344-350; https://doi.org/10.13182/FST03-A358.

[43] Ignat'ev, V. V., Merzlyakov, A. V., Subbotin, V. G., Panov, A. V., Golovatov, Y. V., 2006, "Experimental investigation of the physical properties of salt melts containing sodium and lithium fluorides and beryllium," *Atomic Energy*, 101(5), 822-829; https://doi.org/10.1007/s10512-006-0175-4.

[44] Benes, O., Konings, R.J.M., 2009, "Thermodynamic Properties and Phase Diagrams of Fluoride Salts for Nuclear Applications," *J. Fluorine Chem.*, 130(1), 22-29; https://doi.org/10.1016/j.jfluchem.2008.07.014.

[45] Abe, Y., Kosugiyama, O., Nagashima, A., 1981, "Viscosity of LiF-BeF2 eutectic mixture (X_{BeF_2} = 0.328) and LiF single salt at elevated temperatures," *J. Nucl. Mat.*, 99(2-3), 173-183; https://doi.org/10.1016/0022-3115(81)90186-0.

[46] Blanke, B. C., Bousquet, E. N., Curtis, M. L., Murphy, E. L., 1956, "Density of Fused Mixtures of Sodium Fluoride, Beryllium Fluoride, and Uranium Fluoride," Technical Report MLM-1076; https://doi.org/10.2172/4331902.

[47] Desyatnik, V. N., Nechaev, A.I., Chervinskii, Y. G., 1981, "Viscosity of molten mixtures of BeF_2 with LiF and NaF," Zhurnal prikladnoi khimii, 54, 2310-2313.

[48] Sohal, M. S., Ebner, M. A., Sabharwall, P., Sharpe, P., 2013, "Engineering Database of Liquid Salt Thermophysical and Thermochemical Properties," Technical Report INL/EXT-10-18297; https://doi.org/10.2172/980801.

[49] Cantor, S., 1966, "Estimating Densities of Molten Fluoride Mixtures," Technical Report ORNL-3913, 27; https://www.osti.gov/servlets/purl/4547015.

[50] Salanne, M., Simon, C., Turq, P., 2006, "A First-Principles Description of Liquid BeF_2 and Its Mixtures with LiF: 2. Network Formation in LiF-BeF_2," *J. Phys. Chem. B*, 110, 23, 11461-11467; https://doi.org/10.1021/jp061002u.

[51] Williams, D. F., Toth, L. M., Clarno, K. T., 2006, "Assessment of Candidate Molten Salt Coolants for the Advanced High-Temperature Reactor (AHTR)," Technical Report ORNL/TM-2006/12; https://doi.org/10.2172/885975.

[52] Grimes, W. R., 1967, "Reactor Chemistry Division Annual Progress Report for Period ending December 31, 1965," Technical Report ORNL-3913; https://www.osti.gov/servlets/purl/4547015.

[53] Allen, T., 2010, "Molten Salt Database, http://allen.neep.wisc.edu/shell/index.php/salts, Nuclear Engineering and Engineering Physics Department, University of Wisconsin.

[54] Shams, A., Roelofs, F., Komen, E.M.J., Baglietto, E., 2012, "Optimization of a pebble bed configuration for quasi-direct numerical simulation," *Nucl. Eng. Des.*, 242, 331-340; https://doi.org/10.1016/j.nucengdes.2011.10.054.

[55] Menter, F., 1994, "Two Equation Eddy-Viscosity Turbulence Modeling for Engineering Applications," *AIAA J.*, 32, 8, 1598-1605; https://doi.org/10.2514/3.12149.

[56] Stoots, C., Becker, S., Condie, K., Durst, F., McEligot, D., "A Large-Scale Matched Index of Refraction Flow Facility for LDA Studies Around Complex Geometries," *Exp. Fluids*, 30, 391-398; https://doi.org/10.1007/s003480000216.

[57] Dagenham, E., 1938, "Dowtherm," *Nature*, 141, 1049-1050.

[58] Zweibaum, N., Blandford, E., Gerardi, C., Peterson, P. F., 2020, "Scaling Methodology for Integral Effects Tests in Support of Fluoride Salt-Cooled High-Temperature Reactor Technology," *Nuc. Sci. Eng.*, 194:8-9, 793-811; https://doi.org/10.1080/00295639.2019.1710976.

[59] Moore, R. L., 2010, "Implementation of DOWTHERM A Properties into RELAP5-3D/ATHENA," Technical Report INL/EXT-10-18651; https://doi.org/10.2172/1037788.

[60] Dowtherm™ A Technical Data Sheet, Dow Chemical, Form 176-01472-0417

[61] Huddar, L., 2016, "Heat Transfer in Pebble-Bed Nuclear Reactor Cores Cooled by Fluoride Salts," Ph.D. Dissertation, University of California, Berkeley; https://escholarship.org/uc/item/3c69q4kf.

[62] Romatoski, R.R., 2017, "Fluoride-Salt-Cooled High-Temperature Test Reactor Thermal-Hydraulic Licensing and Uncertainty Propagation Analysis," Nucl. Tech. 205(11), 1495-1512; https://doi.org/10.1080/00295450.2019.1610686.

[63] Novak, A. J., Schunert, S., Carlsen, R. W., Balestra, P., Slaybaugh, R. N., Martineau, R.C., "Multiscale thermal-hydraulic modeling of the pebble bed fluoride-salt-cooled high-temperature reactor," *Annals Nucl. Energy*, 154, 107968; https://doi.org/10.1016/j.anucene.2020.107968.

[64] Harrison, L. D., Brunner, K. M., Hecker, W. C., 2013, "A Combind Packed-Bed Friction Factor Equation: Extension to Higher Reynolds Number with Wall Effects," *AIChE Letter: Transport Phenomena and Fluid Mechanics*; https://doi.org/10.1002/aic.14034.

Appendix A: Sample of Mesh Sensitivity Data

Table 18. Minimum gap thickness study for δ = 0.05 mm at various mesh sizes with 100% relative prism layer thickness.

FLiBe @ 650 C @ Re=500							
Mesh/PLT (mm)	Heat Transfer Performance			Pressure Drop			
	h_avg	Nu	dNu	High (Pa)	Low (Pa)	ΔP	dΔP
0.8	3841.027	105.5904	0.21%	3640.194	538.5483	3101.6	0.0248%
0.735	3849.771	105.8308	0.02%	3639.502	538.4191	3101.1	0.0066%
0.6	3865.012	106.2498	0.42%	3638.161	538.6789	3099.5	0.0450%
0.5	3857.914	106.0546	0.23%	3638.926	538.4653	3100.5	0.0134%
0.4	3849.001	105.8096	BASE	3638.839	537.9617	3100.9	BASE
FLiBe @ 650 C @ Re=1250							
Mesh/PLT (mm)	Heat Transfer Performance			Pressure Drop			
	h_avg	Nu	dNu	High (Pa)	Low (Pa)	ΔP	dΔP
0.8	6536.064	179.6774	2.45%	4019.714	512.6539	3507.1	0.0304%
0.735	6547.252	179.9849	2.29%	4018.487	520.6991	3497.8	0.2341%
0.6	6628.951	182.2309	1.07%	4010.127	512.9849	3497.1	0.2525%
0.5	6667.525	183.2913	0.49%	4011.461	508.141	3503.3	0.0763%
0.4	6700.472	184.197	BASE	4011.237	505.243	3506	BASE
FLiBe @ 650 C @ Re=2500							
Mesh/PLT (mm)	Heat Transfer Performance			Pressure Drop			
	h_avg	Nu	dNu	High (Pa)	Low (Pa)	ΔP	dΔP
0.8	9983.125	274.4376	1.405%	5245.932	425.3438	4820.6	0.6993%
0.735	9969.671	274.0677	1.538%	5295.88	452.2416	4843.6	1.1809%
0.6	10012.57	275.247	1.115%	5209.885	409.5887	4800.3	0.2755%
0.5	10051.96	276.3299	0.726%	5199.83	418.6358	4781.2	0.1236%
0.4	10125.43	278.3496	BASE	5200.104	412.9942	4787.1	BASE

Table 19. Minimum gap thickness study for δ = 0.01 mm at various mesh sizes with 100% relative prism layer thickness.

FLiBe @ 650 C @ Re=500							
Mesh/PLT (mm)	Heat Transfer Performance			Pressure Drop			
	h_avg	Nu	dNu	High (Pa)	Low (Pa)	ΔP	dΔP
0.8	3616.292	99.41241	1.06%	3628.414	539.1493	3089.2647	0.09%
0.735	3615.954	99.40312	1.05%	3629.565	539.3758	3090.1892	0.12%
0.6	3613.988	99.34907	1.00%	3629.664	538.8879	3090.7761	0.14%
0.5	3599.911	98.96209	0.60%	3627.266	538.7337	3088.5323	0.07%
0.4	3578.299	98.36797	BASE	3625.171	538.7703	3086.4007	BASE
FLiBe @ 650 C @ Re=1250							
Mesh/PLT (mm)	Heat Transfer Performance			Pressure Drop			
	h_avg	Nu	dNu	High (Pa)	Low (Pa)	ΔP	dΔP
0.8	6245.379	171.6864	0.63%	3955.33	521.0781	3434.2519	0.11%
0.735	6242.966	171.6201	0.66%	3954.38	524.8256	3429.5544	0.02%
0.6	6256.036	171.9794	0.46%	3955.727	524.2682	3431.4588	0.03%
0.5	6267.637	172.2983	0.27%	3950.003	519.5812	3430.4218	0.00%
0.4	6284.717	172.7678	BASE	3949.715	519.3192	3430.3958	BASE
FLiBe @ 650 C @ Re=2500							
Mesh/PLT (mm)	Heat Transfer Performance			Pressure Drop			
	h_avg	Nu	dNu	High (Pa)	Low (Pa)	ΔP	dΔP
0.8	9715.032	267.0677	0.054%	5029.102	472.7567	4556.3453	0.3446%
0.735	9686.286	266.2774	0.242%	5029.638	463.3757	4566.2623	0.5630%
0.6	9672.044	265.8859	0.389%	5051.003	453.9045	4597.0985	1.2421%
0.5	9669.131	265.8059	0.419%	4934.695	448.7041	4485.9909	1.2048%
0.4	9709.83	266.9247	BASE	4993.157	452.459	4540.698	BASE

Table 20. Minimum gap thickness study for δ = 0.005 mm at various mesh sizes with 100% relative prism layer thickness.

FLiBe @ 650 C @ Re=500							
Mesh/PLT (mm)	Heat Transfer Performance			Pressure Drop			
	h_avg	Nu	dNu	High (Pa)	Low (Pa)	ΔP	dΔP
0.8	3506.635	96.40039	0.09%	3646.682	539.9107	3106.7713	0.0018%
0.735	3503.35	96.31009	0.05%	3645.767	538.9412	3106.8258	0.0104%
0.6	3505.11	96.35847	0.62%	3644.681	537.5324	3107.1486	0.0284%
0.5	3483.357	95.76046	0.49%	3645.864	539.599	3106.265	0.0208%
0.4	3466.231	95.28965	BASE	3643.645	538.0273	3105.6177	BASE
FLiBe @ 650 C @ Re=1250							
Mesh/PLT (mm)	Heat Transfer Performance			Pressure Drop			
	h_avg	Nu	dNu	High (Pa)	Low (Pa)	ΔP	dΔP
0.8	6168.054	169.5651	0.32%	4052.843	521.9075	3530.9355	0.14%
0.735	6148.31	169.0223	0.04%	4058.083	522.3194	3535.7636	0.40%
0.6	6145.604	168.9479	0.19%	4042.039	520.4289	3521.6101	0.03%
0.5	6133.978	168.6283	0.40%	4041.025	518.4522	3522.5728	0.00%
0.4	6109.385	167.9522	BASE	4039.427	516.9837	3522.4433	BASE
FLiBe @ 650 C @ Re=2500							
Mesh/PLT (mm)	Heat Transfer Performance			Pressure Drop			
	h_avg	Nu	dNu	High (Pa)	Low (Pa)	ΔP	dΔP
0.8	9719.624	267.2008	0.48%	5332.799	473.1502	4859.6488	0.03%
0.735	9673.474	265.9321	0.72%	5318.898	457.9345	4860.9635	0.27%
0.6	9604.692	264.0412	0.10%	5277.246	429.4728	4847.7732	1.06%
0.5	9595.561	263.7902	0.09%	5349.818	450.1791	4899.6389	0.53%
0.4	9603.761	264.0156	BASE	5356.576	430.8737	4925.7023	BASE

Table 21. Grid Convergence Index (GCI) discretization error for δ = 0.05 mm at Re = 500, 1250, and 2500.

Re = 500			Re = 1250			Re = 2500		
Nu			Nu			Nu		
N_1	20743930	cells	N_1	20743930	cells	N_1	20743930	cells
N_2	12597270	cells	N_2	12597270	cells	N_2	12597270	cells
N_3	7020463	cells	N_3	7020463	cells	N_3	7020463	cells
r_{21}	1.2	-	r_{21}	1.2	-	r_{21}	1.2	-
r_{32}	1.225	-	r_{32}	1.225	-	r_{32}	1.225	-
ϕ_1	106.055	-	ϕ_1	183.291	-	ϕ_1	276.330	-
ϕ_2	106.250	-	ϕ_2	182.231	-	ϕ_2	275.247	-
ϕ_3	105.831	-	ϕ_3	179.985	-	ϕ_3	274.068	-
ε_{32}	-0.41898	-	ε_{32}	-2.24592	-	ε_{32}	-1.1793	-
ε_{21}	0.195125	-	ε_{21}	-1.06041	-	ε_{21}	-1.08284	-
s	-1	Osc.	s	1	Mon.	s	1	Mon.
Calculations			Calculations			Calculations		
p iterative process			p iterative process			p iterative process		
p	q(p)		p	q(p)		p	q(p)	
1.000	-0.004907		1.000	-0.051153		1.000	-0.051153	
4.129	-0.025477		3.470	-0.063787		3.470	-0.063787	
3.870	-0.023499		3.311	-0.062919		3.311	-0.062919	
3.895	-0.023688		3.322	-0.062979		3.322	-0.062979	
3.892	-0.023670		3.321	-0.062974		3.321	-0.062974	
3.892	-0.023671		3.321	-0.062975		3.321	-0.062975	
3.892	-0.023671		3.321	-0.062975		3.321	-0.062975	
3.892	-0.023671		3.321	-0.062975		3.321	-0.062975	
3.892	-0.023671		3.321	-0.062975		3.321	-0.062975	
ϕ_{ext}^{21}	105.8658	-	ϕ_{ext}^{21}	184.5656419	-	ϕ_{ext}^{21}	277.6312	-
e_a^{21}	0.2%	%	e_a^{21}	0.6%	%	e_a^{21}	0.4%	%
e_{ext}^{21}	0.2%	%	e_{ext}^{21}	0.69%	%	e_{ext}^{21}	0.47%	%
GCI_{fine}^{21}	**0.223%**	**%**	**GCI_{fine}^{21}**	**0.87%**	**%**	**GCI_{fine}^{21}**	**0.59%**	**%**

Table 22. Grid Convergence Index (GCI) discretization error for δ = 0.01 mm at Re = 500, 1250, and 2500.

Re = 500			Re = 1250			Re = 2500		
Nu			Nu			Nu		
N_1	20804940	cells	N_1	20804940	cells	N_1	20804940	cells
N_2	12357587	cells	N_2	12357587	cells	N_2	12357587	cells
N_3	6951953	cells	N_3	6951953	cells	N_3	6951953	cells
r_{21}	1.5	-	r_{21}	1.5	-	r_{21}	1.5	-
r_{32}	1.333333	-	r_{32}	1.333333333	-	r_{32}	1.333333	-
ϕ_1	99.412	-	ϕ_1	171.686	-	ϕ_1	267.068	-
ϕ_2	99.349	-	ϕ_2	171.979	-	ϕ_2	265.886	-
ϕ_3	98.368	-	ϕ_3	172.768	-	ϕ_3	266.925	-
ε_{32}	-0.9811	-	ε_{32}	0.788444974	-	ε_{32}	1.038743	-
ε_{21}	-0.06334	-	ε_{21}	0.292962522	-	ε_{21}	-1.18175	-
s	1	Mon.	s	1	Mon.	s	-1	Osc.
Calculations			Calculations			Calculations		
p iterative process			p iterative process			p iterative process		
p	q(p)		p	q(p)		p	q(p)	
1.000	0.176091		1.000	0.176091		1.000	0.029963	
7.758	0.427051		3.442	0.254153		0.148	0.003881	
9.183	0.491224		3.885	0.270039		0.296	0.007961	
9.548	0.508037		3.975	0.273332		0.273	0.007310	
9.643	0.512466		3.994	0.274017		0.277	0.007413	
9.668	0.513635		3.998	0.274159		0.276	0.007397	
9.675	0.513943		3.999	0.274189		0.276	0.007399	
9.677	0.514024		3.999	0.274195		0.276	0.007399	
9.677	0.514046		3.999	0.274197		0.276	0.007399	
ϕ_{ext}^{21}	99.41368	-	ϕ_{ext}^{21}	171.6142441	-	ϕ_{ext}^{21}	277.0443	-
e_a^{21}	0.1%	%	e_a^{21}	0.2%	%	e_a^{21}	0.4%	%
e_{ext}^{21}	0.0%	%	e_{ext}^{21}	0.04%	%	e_{ext}^{21}	3.60%	%
GCI_{fine}^{21}	**0.002%**	**%**	**GCI_{fine}^{21}**	**0.05%**	**%**	**GCI_{fine}^{21}**	**4.67%**	**%**

Table 23. Grid Convergence Index (GCI) discretization error for δ = 0.005 mm at Re = 500, 1250, and 2500.

Re = 500			Re = 1250			Re = 2500		
Nu			Nu			Nu		
N_1	20804940	cells	N_1	20804940	cells	N_1	20804940	cells
N_2	12357587	cells	N_2	12357587	cells	N_2	12357587	cells
N_3	6951953	cells	N_3	6951953	cells	N_3	6951953	cells
r_{21}	1.5	-	r_{21}	1.5	-	r_{21}	1.5	-
r_{32}	1.225	-	r_{32}	1.225	-	r_{32}	1.225	-
ϕ_1	3105.618	-	ϕ_1	3522.443	-	ϕ_1	4925.702	-
ϕ_2	3107.149	-	ϕ_2	3521.610	-	ϕ_2	4847.773	-
ϕ_3	3106.826	-	ϕ_3	3535.764	-	ϕ_3	4860.964	-
ε_{32}	-0.3228	-	ε_{32}	14.1535	-	ε_{32}	13.1903	-
ε_{21}	1.5309	-	ε_{21}	-0.8332	-	ε_{21}	-77.9291	-
s	-1	Osc.	s	-1	Osc.	s	-1	Osc.
Calculations			Calculations			Calculations		
p iterative process			p iterative process			p iterative process		
p	q(p)		p	q(p)		p	q(p)	
1.000	0.050610		1.000	0.050610		1.000	0.050610	
3.552	0.232591		7.273	0.572490		4.094	0.278589	
2.518	0.151009		10.237	0.855916		2.799	0.172260	
2.981	0.186464		11.846	1.007927		3.403	0.220303	
2.780	0.170815		12.710	1.088632		3.130	0.198224	
2.869	0.177678		13.168	1.131246		3.255	0.208298	
2.830	0.174660		13.410	1.153685		3.198	0.203686	
2.847	0.175986		13.537	1.165482		3.224	0.205794	
2.840	0.175403		13.604	1.171681		3.212	0.204830	
ϕ_{ext}^{21}	3104.91	-	ϕ_{ext}^{21}	3522.446664	-	ϕ_{ext}^{21}	4954.7985	-
e_a^{21}	0.0493%	%	e_a^{21}	0.0237%	%	e_a^{21}	1.5821%	%
e_{ext}^{21}	0.0228%	%	e_{ext}^{21}	0.0001%	%	e_{ext}^{21}	0.5872%	%
GCI_{fine}^{21}	**0.0285%**	**%**	**GCI_{fine}^{21}**	**0.0001%**	**%**	**GCI_{fine}^{21}**	**0.738376%**	**%**

Appendix B: Sample of Similarity Scaling Data

Table 24. Similarity scaling results between FLiBe and Dowtherm-A at full scale (1:1 scale) for Pr = 19.4.

PROTOTYPE (FLiBe @ 600°C)			MODEL (Dowtherm A @ 68.058°C)			Ratio (m/m)/(p/m)	
Geometrics							
$(A_{ref})_p$	11670.220	mm^2	$(A_{ref})_m$	11670.220	mm^2	1:1	1
$(D_{cyl})_p$	121.89744	mm	$(D_{cyl})_m$	121.89744	mm	1:1	1
$(R_{cyl})_p$	60.94872	mm	$(R_{cyl})_m$	60.94872	mm	1:1	1
$(H_{cyl})_p$	309.01075	mm	$(H_{cyl})_m$	309.01075	mm	1:1	1
$(D_{pebble})_p$	30.00000	mm	$(D_{pebble})_m$	30.00000	mm	1:1	1
$(A_{s,pebble})_p$	2827.43339	mm^2	$(A_{s,pebble})_m$	2827.4334	mm^2	1:1	1
$(V_{pebble})_p$	14137.1669	mm^3	$(V_{pebble})_m$	14137.167	mm^3	1:1	1
$(V_{t\ pebble})_p$	1060287.52	mm^3	$(V_{t\ pebble})_m$	1060287.5	mm^3	1:1	1
$(V_{cyl,\ pebble\ region})_p$	2650718.80	mm^3	$(V_{cyl,\ pebble\ region})_m$	2650718.8	mm^3	1:1	1
$(H_{pebble\ region})_p$	227.13529	mm	$(H_{pebble\ region})_m$	227.13529	mm	1:1	1
$(H_{additional})_p$	81.87546	mm	$(H_{additional})_m$	81.87546	mm	1:1	1
Thermophysical Properties (Equations)							
$(\rho)_p$	2163.5011	kg/m^3	$(\rho)_m$	1021.1826	kg/m^3	1:2.119	0.472
$(\mu)_p$	0.00855	kg/ms	$(\mu)_m$	0.00148	kg/ms	1:5.763	0.174
$(\nu)_p$	3.95361E-06	m^2/s	$(\nu)_m$	1.453E-06	m^2/s	1:2.72	0.368
$(Cp_f)_p$	2415.78000	J/kgK	$(Cp_f)_m$	1710.66	J/kgK	1:1.412	0.708
$(k)_p$	1.06627	W/mK	$(k)_m$	0.13101	W/mK	1:8.139	0.123
$(Pr)_p$	19.37938	-	$(Pr)_m$	19.37939	-	1:1	1.000
Flow/Heating Conditions							
T_{in}	600	°C	T_{in}	68.058233	°C	-	-
T_{in}	873.15	K	T_{in}	341.2082	K	-	-
$(Q)_p$	320.914	W	$(Q)_m$	11.948602	W	1:26.858	0.0372

Table 25. Requisite flow conditions between FLiBe and Dowtherm-A at full scale (1:1 scale) for Pr = 19.4.

PROTOTYPE (FLiBe @ 600°C)			MODEL (Dowtherm A @ 68.058°C)			
Re	$(u_{ref})_p$	$(\dot{m})_p$	Re	$(u_{ref})_m$	$(\dot{m})_m$	$(u_{ref})_R$
500	0.06589	1.66371	500	0.02422	0.28868	1:2.7203
750	0.09884	2.49557	750	0.03633	0.43302	1:2.7203
1000	0.13179	3.32743	1000	0.04845	0.57736	1:2.7203
1250	0.16473	4.15928	1250	0.06056	0.72170	1:2.7203
1500	0.19768	4.99114	1500	0.07267	0.86604	1:2.7203
1750	0.23063	5.82299	1750	0.08478	1.01037	1:2.7203
2000	0.26357	6.65485	2000	0.09689	1.15471	1:2.7203
2250	0.29652	7.48671	2250	0.10900	1.29905	1:2.7203
2500	0.32947	8.31856	2500	0.12112	1.44339	1:2.7203
PROTOTYPE (FLiBe @ 600°C)			MODEL (Dowtherm A @ 68.058°C)			
Re	T_e	$(T_{H0}-T_{C0})_p$	Re	$(T_{H0}-T_{C0})_R$	$(T_{H0}-T_{C0})_m$	T_e
500	605.98845	5.98845	500	1:3.3	1.81468	69.87291
750	603.99230	3.99230	750	1:3.3	1.20979	69.26802
1000	602.99422	2.99422	1000	1:3.3	0.90734	68.96557
1250	602.39538	2.39538	1250	1:3.3	0.72587	68.78411
1500	601.99615	1.99615	1500	1:3.3	0.60489	68.66313
1750	601.71098	1.71098	1750	1:3.3	0.51848	68.57671
2000	601.49711	1.49711	2000	1:3.3	0.45367	68.51190
2250	601.33077	1.33077	2250	1:3.3	0.40326	68.46150
2500	601.19769	1.19769	2500	1:3.3	0.36294	68.42117

Table 26. Similarity scaling results between FLiBe and Dowtherm-A at full scale (1:1 scale) for Pr = 7.95.

PROTOTYPE (FLiBe @ 800°C)			MODEL (Dowtherm A @ 177.828°C)			Ratio (m/m)/(p/m)	
Geometrics							
$(A_{ref})_p$	11670.220	mm^2	$(A_{ref})_m$	11670.220	mm^2	1:1	1
$(D_{cyl})_p$	121.89744	mm	$(D_{cyl})_m$	121.89744	mm	1:1	1
$(R_{cyl})_p$	60.94872	mm	$(R_{cyl})_m$	60.94872	mm	1:1	1
$(H_{cyl})_p$	309.01075	mm	$(H_{cyl})_m$	309.01075	mm	1:1	1
$(D_{pebble})_p$	30.00000	mm	$(D_{pebble})_m$	30.00000	mm	1:1	1
$(A_{s,pebble})_p$	2827.43339	mm^2	$(A_{s,pebble})_m$	2827.43339	mm^2	1:1	1
$(V_{pebble})_p$	14137.1669	mm^3	$(V_{pebble})_m$	14137.1669	mm^3	1:1	1
$(V_{t\ pebble})_p$	1060287.52	mm^3	$(V_{t\ pebble})_m$	1060287.52	mm^3	1:1	1
$(V_{cyl,\ pebble\ region})_p$	2650718.80	mm^3	$(V_{cyl,\ pebble\ region})_m$	2650718.80	mm^3	1:1	1
$(H_{pebble\ region})_p$	227.13529	mm	$(H_{pebble\ region})_m$	227.13529	mm	1:1	1
$(H_{additional})_p$	81.87546	mm	$(H_{additional})_m$	81.87546	mm	1:1	1
Thermophysical Properties (Equations)							
$(\rho)_p$	2082.30110	kg/m^3	$(\rho)_m$	927.43028	kg/m^3	1:2.245	0.445
$(\mu)_p$	0.00384	kg/ms	$(\mu)_m$	0.00045	kg/ms	1:8.584	0.116
$(\nu)_p$	1.84302E-06	m^2/s	$(\nu)_m$	4.8204E-07	m^2/s	1:3.823	0.262
$(Cp_f)_p$	2415.78000	J/kgK	$(Cp_f)_m$	2017.27950	J/kgK	1:1.198	0.835
$(k)_p$	1.16627	W/mK	$(k)_m$	0.11345	W/mK	1:10.28	0.097
$(Pr)_p$	7.94935	-	$(Pr)_m$	7.94935	-	1:1	1.000
Flow/Heating Conditions							
T_{in}	800	°C	T_{in}	177.827800	°C	-	-
T_{in}	1073.15	K	T_{in}	450.977800	K	-	-
$(Q)_p$	320.914	W	$(Q)_m$	9.45960	W	1:33.925	0.0295

Table 27. Requisite flow conditions between FLiBe and Dowtherm-A at full scale (1:1 scale) for Pr = 7.95.

PROTOTYPE (FLiBe @ 800°C)			MODEL (Dowtherm A @ 177.828°C)			
Re	$(u_{ref})_p$	$(\dot{m})_p$	Re	$(u_{ref})_m$	$(\dot{m})_m$	$(u_{ref})_R$
500	0.03072	0.74645	500	0.00803	0.08695	1:3.8234
750	0.04608	1.11968	750	0.01205	0.13043	1:3.8234
1000	0.06143	1.49290	1000	0.01607	0.17391	1:3.8234
1250	0.07679	1.86613	1250	0.02008	0.21739	1:3.8234
1500	0.09215	2.23935	1500	0.02410	0.26086	1:3.8234
1750	0.10751	2.61258	1750	0.02812	0.30434	1:3.8234
2000	0.12287	2.98581	2000	0.03214	0.34782	1:3.8234
2250	0.13823	3.35903	2250	0.03615	0.39129	1:3.8234
2500	0.15359	3.73226	2500	0.04017	0.43477	1:3.8234
PROTOTYPE (FLiBe @ 800°C)			MODEL (Dowtherm A @ 177.828°C)			
Re	T_e	$(T_{H0}-T_{C0})_p$	Re	$(T_{H0}-T_{C0})_R$	$(T_{H0}-T_{C0})_m$	T_e
500	813.34722	13.34722	500	1:3.3	4.04461	181.87241
750	808.89815	8.89815	750	1:3.3	2.69641	180.52421
1000	806.67361	6.67361	1000	1:3.3	2.02231	179.85011
1250	805.33889	5.33889	1250	1:3.3	1.61785	179.44565
1500	804.44907	4.44907	1500	1:3.3	1.34820	179.17600
1750	803.81349	3.81349	1750	1:3.3	1.15560	178.98340
2000	803.33681	3.33681	2000	1:3.3	1.01115	178.83895
2250	802.96605	2.96605	2250	1:3.3	0.89880	178.72660
2500	802.66944	2.66944	2500	1:3.3	0.80892	178.63672

Table 28. Similarity scaling results between FLiBe and Dowtherm-A at reduced length scale (0.75:1 scale) for Pr = 19.4.

PROTOTYPE (FLiBe @ 600°C)			MODEL (Dowtherm A @ 68.058°C)			Ratio (m/m)/(p/m)	
Geometrics							
$(A_{ref})_p$	11670.220	mm^2	$(A_{ref})_m$	6564.49875	mm^2	1:1.778	0.563
$(D_{cyl})_p$	121.89744	mm	$(D_{cyl})_m$	91.4230791	mm	1:1.333	0.750
$(R_{cyl})_p$	60.94872	mm	$(R_{cyl})_m$	45.7115396	mm	1:1.333	0.750
$(H_{cyl})_p$	309.01075	mm	$(H_{cyl})_m$	231.75806	mm	1:1.333	0.750
$(D_{pebble})_p$	30.00000	mm	$(D_{pebble})_m$	22.50000	mm	1:1.333	0.750
$(A_{s,pebble})_p$	2827.43339	mm^2	$(A_{s,pebble})_m$	1590.43128	mm^2	1:1.778	0.563
$(V_{pebble})_p$	14137.1669	mm^3	$(V_{pebble})_m$	5964.11730	mm^3	1:2.37	0.422
$(V_{t\ pebble})_p$	1060287.52	mm^3	$(V_{t\ pebble})_m$	447308.7978	mm^3	1:2.37	0.422
$(V_{cyl,\ pebble\ region})_p$	2650718.80	mm^3	$(V_{cyl,\ pebble\ region})_m$	1118271.994	mm^3	1:2.37	0.422
$(H_{pebble\ region})_p$	227.13529	mm	$(H_{pebble\ region})_m$	170.351467	mm	1:1.333	0.750
$(H_{additional})_p$	81.87546	mm	$(H_{additional})_m$	61.40659	mm	1:1.333	0.750
Thermophysical Properties (Equations)							
$(\rho)_p$	2163.50110	kg/m^3	$(\rho)_m$	1021.18263	kg/m^3	1:2.12	0.472
$(\mu)_p$	0.00855	kg/ms	$(\mu)_m$	0.00148	kg/ms	1:5.76	0.174
$(\nu)_p$	3.95361E-06	m^2/s	$(\nu)_m$	1.45339E-06	m^2/s	1:2.72	0.368
$(Cp_f)_p$	2415.78000	J/kgK	$(Cp_f)_m$	1710.66046	J/kgK	1:1.41	0.708
$(k)_p$	1.06627	W/mK	$(k)_m$	0.13101	W/mK	1:8.14	0.123
$(Pr)_p$	19.37938	-	$(Pr)_m$	19.37939	-	1:1	1.000
Flow/Heating Conditions							
T_{in}	600	°C	T_{in}	68.058233	°C	-	-
T_{in}	873.15	K	T_{in}	341.208233	K	-	-
$(Q)_p$	320.914	W	$(Q)_m$	8.96145144	W	1:35.81	0.0279

Table 29. Requisite flow conditions between FLiBe and Dowtherm-A at reduced length scale (0.75:1 scale) for Pr = 19.4.

PROTOTYPE (FLiBe @ 600°C)			MODEL (Dowtherm A @ 68.058°C)			
Re	$(u_{ref})_p$	$(\dot{m})_p$	Re	$(u_{ref})_m$	$(\dot{m})_m$	$(u_{ref})_R$
500	0.06589	1.66371	500	0.03230	0.21651	1:2.0402
750	0.09884	2.49557	750	0.04845	0.32476	1:2.0402
1000	0.13179	3.32743	1000	0.06460	0.43302	1:2.0402
1250	0.16473	4.15928	1250	0.08074	0.54127	1:2.0402
1500	0.19768	4.99114	1500	0.09689	0.64953	1:2.0402
1750	0.23063	5.82299	1750	0.11304	0.75778	1:2.0402
2000	0.26357	6.65485	2000	0.12919	0.86604	1:2.0402
2250	0.29652	7.48671	2250	0.14534	0.97429	1:2.0402
2500	0.32947	8.31856	2500	0.16149	1.08254	1:2.0402
PROTOTYPE (FLiBe @ 600°C)			MODEL (Dowtherm A @ 68.058°C)			
Re	T_e	$(T_{H0}-T_{C0})_p$	Re	$(T_{H0}-T_{C0})_R$	$(T_{H0}-T_{C0})_m$	T_e
500	605.98845	5.98845	500	1:3.3	1.81468	69.87291
750	603.99230	3.99230	750	1:3.3	1.20979	69.26802
1000	602.99422	2.99422	1000	1:3.3	0.90734	68.96557
1250	602.39538	2.39538	1250	1:3.3	0.72587	68.78411
1500	601.99615	1.99615	1500	1:3.3	0.60489	68.66313
1750	601.71098	1.71098	1750	1:3.3	0.51848	68.57671
2000	601.49711	1.49711	2000	1:3.3	0.45367	68.51190
2250	601.33077	1.33077	2250	1:3.3	0.40326	68.46150
2500	601.19769	1.19769	2500	1:3.3	0.36294	68.42117

Table 30. Similarity scaling results between FLiBe and Dowtherm-A at reduced length scale (0.75:1 scale) for Pr = 7.95.

PROTOTYPE (FLiBe @ 800°C)			MODEL (Dowtherm A @ 177.828°C)			Ratio (m/m)/(p/m)	
Geometrics							
$(A_{ref})_p$	11670.220	mm^2	$(A_{ref})_m$	6564.4988	mm^2	1:1.778	0.563
$(D_{cyl})_p$	121.89744	mm	$(D_{cyl})_m$	91.423079	mm	1:1.333	0.750
$(R_{cyl})_p$	60.94872	mm	$(R_{cyl})_m$	45.711540	mm	1:1.333	0.750
$(H_{cyl})_p$	309.01075	mm	$(H_{cyl})_m$	231.75806	mm	1:1.333	0.750
$(D_{pebble})_p$	30.00000	mm	$(D_{pebble})_m$	22.50000	mm	1:1.333	0.750
$(A_{s,pebble})_p$	2827.43339	mm^2	$(A_{s,pebble})_m$	1590.4313	mm^2	1:1.778	0.563
$(V_{pebble})_p$	14137.1669	mm^3	$(V_{pebble})_m$	5964.1173	mm^3	1:2.37	0.422
$(V_{t\ pebble})_p$	1060287.52	mm^3	$(V_{t\ pebble})_m$	447308.80	mm^3	1:2.37	0.422
$(V_{cyl,\ pebble\ region})_p$	2650718.80	mm^3	$(V_{cyl,\ pebble\ region})_m$	1118272	mm^3	1:2.37	0.422
$(H_{pebble\ region})_p$	227.13529	mm	$(H_{pebble\ region})_m$	170.3515	mm	1:1.333	0.750
$(H_{additional})_p$	81.87546	mm	$(H_{additional})_m$	61.40659	mm	1:1.333	0.750
Thermophysical Properties (Equations)							
$(\rho)_p$	2082.30110	kg/m^3	$(\rho)_m$	927.4303	kg/m^3	1:2.25	0.445
$(\mu)_p$	0.00384	kg/ms	$(\mu)_m$	0.00045	kg/ms	1:8.58	0.116
$(\nu)_p$	1.84302E-06	m^2/s	$(\nu)_m$	4.82E-07	m^2/s	1:3.82	0.262
$(Cp_f)_p$	2415.78000	J/kgK	$(Cp_f)_m$	2017.2795	J/kgK	1:1.2	0.835
$(k)_p$	1.16627	W/mK	$(k)_m$	0.11345	W/mK	1:10.3	0.097
$(Pr)_p$	7.94935	-	$(Pr)_m$	7.94935	-	1:1	1.000
Flow/Heating Conditions							
T_{in}	800	°C	T_{in}	177.8278	°C	-	-
T_{in}	1073.15	K	T_{in}	450.9778	K	-	-
$(Q)_p$	320.914	W	$(Q)_m$	7.094698	W	1:45.233	0.0221

Table 31. Requisite flow conditions between FLiBe and Dowtherm-A at reduced length scale (0.75:1 scale) for Pr = 7.95.

PROTOTYPE (FLiBe @ 800°C)			MODEL (Dowtherm A @ 177.828°C)			
Re	$(u_{ref})_p$	$(\dot{m})_p$	Re	$(u_{ref})_m$	$(\dot{m})_m$	$(u_{ref})_R$
500	0.03072	0.74645	500	0.01071	0.06522	1:2.8675
750	0.04608	1.11968	750	0.01607	0.09782	1:2.8675
1000	0.06143	1.49290	1000	0.02142	0.13043	1:2.8675
1250	0.07679	1.86613	1250	0.02678	0.16304	1:2.8675
1500	0.09215	2.23935	1500	0.03214	0.19565	1:2.8675
1750	0.10751	2.61258	1750	0.03749	0.22825	1:2.8675
2000	0.12287	2.98581	2000	0.04285	0.26086	1:2.8675
2250	0.13823	3.35903	2250	0.04820	0.29347	1:2.8675
2500	0.15359	3.73226	2500	0.05356	0.32608	1:2.8675
PROTOTYPE (FLiBe @ 800°C)			MODEL (Dowtherm A @ 177.828°C)			
Re	T_e	$(T_{H0}-T_{C0})_p$	Re	$(T_{H0}-T_{C0})_R$	$(T_{H0}-T_{C0})_m$	T_e
500	613.34722	13.34722	500	1:3.3	4.04461	181.87241
750	608.89815	8.89815	750	1:3.3	2.69641	180.52421
1000	606.67361	6.67361	1000	1:3.3	2.02231	179.85011
1250	605.33889	5.33889	1250	1:3.3	1.61785	179.44565
1500	604.44907	4.44907	1500	1:3.3	1.34820	179.17600
1750	603.81349	3.81349	1750	1:3.3	1.15560	178.98340
2000	603.33681	3.33681	2000	1:3.3	1.01115	178.83895
2250	602.96605	2.96605	2250	1:3.3	0.89880	178.72660
2500	602.66944	2.66944	2500	1:3.3	0.80892	178.63672

Table 32. Similarity scaling results between FLiBe and Dowtherm-A at reduced length scale (0.5:1 scale) for Pr = 19.4.

PROTOTYPE (FLiBe @ 600°C)			MODEL (Dowtherm A @ 68.058°C)			Ratio (m/m)/(p/m)	
Geometrics							
$(A_{ref})_p$	11670.22	mm^2	$(A_{ref})_m$	2917.555	mm^2	1:4	0.25
$(D_{cyl})_p$	121.89744	mm	$(D_{cyl})_m$	60.948719	mm	1:2	0.5
$(R_{cyl})_p$	60.94872	mm	$(R_{cyl})_m$	30.474360	mm	1:2	0.5
$(H_{cyl})_p$	309.01075	mm	$(H_{cyl})_m$	154.50537	mm	1:2	0.5
$(D_{pebble})_p$	30.00000	mm	$(D_{pebble})_m$	15.00000	mm	1:2	0.5
$(A_{s,pebble})_p$	2827.43339	mm^2	$(A_{s,pebble})_m$	706.85835	mm^2	1:4	0.25
$(V_{pebble})_p$	14137.167	mm^3	$(V_{pebble})_m$	1767.14587	mm^3	1:8	0.125
$(V_{t\ pebble})_p$	1060287.52	mm^3	$(V_{t\ pebble})_m$	132535.94	mm^3	1:8	0.125
$(V_{cyl,\ pebble\ region})_p$	2650718.8	mm^3	$(V_{cyl,\ pebble\ region})_m$	331339.85	mm^3	1:8	0.125
$(H_{pebble\ region})_p$	227.13529	mm	$(H_{pebble\ region})_m$	113.56764	mm	1:2	0.5
$(H_{additional})_p$	81.87546	mm	$(H_{additional})_m$	40.93773	mm	1:2	0.5
Thermophysical Properties (Equations)							
$(\rho)_p$	2163.50110	kg/m^3	$(\rho)_m$	1021.18263	kg/m^3	1:2.12	0.472
$(\mu)_p$	0.00855	kg/ms	$(\mu)_m$	0.00148	kg/ms	1:5.76	0.174
$(\nu)_p$	3.95361E-06	m^2/s	$(\nu)_m$	1.4534E-06	m^2/s	1:2.72	0.368
$(Cp_f)_p$	2415.78000	J/kgK	$(Cp_f)_m$	1710.6605	J/kgK	1:1.41	0.708
$(k)_p$	1.06627	W/mK	$(k)_m$	0.13101	W/mK	1:8.14	0.123
$(Pr)_p$	19.37938	-	$(Pr)_m$	19.37939	-	1:1	1.000
Flow/Heating Conditions							
T_{in}	600	°C	T_{in}	68.058233	°C	-	-
T_{in}	873.15	K	T_{in}	341.208233	K	-	-
$(Q)_p$	320.914	W	$(Q)_m$	5.9743	W	1:53.716	0.0186

Table 33. Requisite flow conditions between FLiBe and Dowtherm-A at reduced length scale (0.5:1 scale) for Pr = 19.4.

PROTOTYPE (FLiBe @ 600°C)			MODEL (Dowtherm A @ 68.058°C)			
Re	$(u_{ref})_p$	$(\dot{m})_p$	Re	$(u_{ref})_m$	$(\dot{m})_m$	$(u_{ref})_R$
500	0.06589	1.66371	500	0.04845	0.14434	1:1.3601
750	0.09884	2.49557	750	0.07267	0.21651	1:1.3601
1000	0.13179	3.32743	1000	0.09689	0.28868	1:1.3601
1250	0.16473	4.15928	1250	0.12112	0.36085	1:1.3601
1500	0.19768	4.99114	1500	0.14534	0.43302	1:1.3601
1750	0.23063	5.82299	1750	0.16956	0.50519	1:1.3601
2000	0.26357	6.65485	2000	0.19379	0.57736	1:1.3601
2250	0.29652	7.48671	2250	0.21801	0.64953	1:1.3601
2500	0.32947	8.31856	2500	0.24223	0.72170	1:1.3601
PROTOTYPE (FLiBe @ 600°C)			MODEL (Dowtherm A @ 68.058°C)			
Re	T_e	$(T_{H0}-T_{C0})_p$	Re	$(T_{H0}-T_{C0})_R$	$(T_{H0}-T_{C0})_m$	T_e
500	605.98845	5.98845	500	1:3.3	1.81468	69.87291
750	603.99230	3.99230	750	1:3.3	1.20979	69.26802
1000	602.99422	2.99422	1000	1:3.3	0.90734	68.96557
1250	602.39538	2.39538	1250	1:3.3	0.72587	68.78411
1500	601.99615	1.99615	1500	1:3.3	0.60489	68.66313
1750	601.71098	1.71098	1750	1:3.3	0.51848	68.57671
2000	601.49711	1.49711	2000	1:3.3	0.45367	68.51190
2250	601.33077	1.33077	2250	1:3.3	0.40326	68.46150
2500	601.19769	1.19769	2500	1:3.3	0.36294	68.42117

Table 34. Similarity scaling results between FLiBe and Dowtherm-A at reduced length scale (0.5:1 scale) for Pr = 11.9.

PROTOTYPE (FLiBe @ 700°C)			MODEL (Dowtherm A @ 119.662°C)			Ratio (m/m)/(p/m)	
Geometrics							
$(A_{ref})_p$	11670.22	mm^2	$(A_{ref})_m$	2917.555	mm^2	1:4	0.25
$(D_{cyl})_p$	121.89744	mm	$(D_{cyl})_m$	60.94872	mm	1:2	0.5
$(R_{cyl})_p$	60.94872	mm	$(R_{cyl})_m$	30.47436	mm	1:2	0.5
$(H_{cyl})_p$	309.01075	mm	$(H_{cyl})_m$	154.50537	mm	1:2	0.5
$(D_{pebble})_p$	30.00000	mm	$(D_{pebble})_m$	15.00000	mm	1:2	0.5
$(A_{s,pebble})_p$	2827.43	mm^2	$(A_{s,pebble})_m$	706.85835	mm^2	1:4	0.25
$(V_{pebble})_p$	14137.167	mm^3	$(V_{pebble})_m$	1767.14587	mm^3	1:8	0.125
$(V_{t\ pebble})_p$	1060287.5	mm^3	$(V_{t\ pebble})_m$	132535.94	mm^3	1:8	0.125
$(V_{cyl,\ pebble\ region})_p$	2650718.8	mm^3	$(V_{cyl,\ pebble\ region})_m$	331339.85	mm^3	1:8	0.125
$(H_{pebble\ region})_p$	227.13529	mm	$(H_{pebble\ region})_m$	113.56765	mm	1:2	0.5
$(H_{additional})_p$	81.87546	mm	$(H_{additional})_m$	40.93773	mm	1:2	0.5
Thermophysical Properties (Equations)							
$(\rho)_p$	2122.9	kg/m^3	$(\rho)_m$	978.43930	kg/m^3	1:2.17	0.461
$(\mu)_p$	0.00550	kg/ms	$(\mu)_m$	0.00079	kg/ms	1:6.98	0.143
$(\nu)_p$	2.59E-06	m^2/s	$(\nu)_m$	8.0521E-07	m^2/s	1:3.22	0.311
$(Cp_f)_p$	2415.78	J/kgK	$(Cp_f)_m$	1853.99683	J/kgK	1:1.3	0.767
$(k)_p$	1.11627	W/mK	$(k)_m$	0.12275	W/mK	1:9.09	0.110
$(Pr)_p$	11.89914	-	$(Pr)_m$	11.89914	-	1:1	1.000
Flow/Heating Conditions							
T_{in}	700	°C	T_{in}	119.66225	°C	-	-
T_{in}	973.15	K	T_{in}	392.81225	K	-	-
$(Q)_p$	320.914	W	$(Q)_m$	5.34704	W	1:60.017	0.0167

Table 35. Requisite flow conditions between FLiBe and Dowtherm-A at reduced length scale (0.5:1 scale) for Pr = 11.9.

PROTOTYPE (FLiBe @ 700°C)			MODEL (Dowtherm A @ 119.662°C)			
Re	$(u_{ref})_p$	$(\dot{m})_p$	Re	$(u_{ref})_m$	$(\dot{m})_m$	$(u_{ref})_R$
500	0.04317	1.06944	500	0.02684	0.07662	1:1.6083
750	0.06475	1.60416	750	0.04026	0.11493	1:1.6083
1000	0.08633	2.13888	1000	0.05368	0.15324	1:1.6083
1250	0.10792	2.67360	1250	0.06710	0.19155	1:1.6083
1500	0.12950	3.20832	1500	0.08052	0.22986	1:1.6083
1750	0.15108	3.74304	1750	0.09394	0.26817	1:1.6083
2000	0.17267	4.27776	2000	0.10736	0.30648	1:1.6083
2250	0.19425	4.81248	2250	0.12078	0.34479	1:1.6083
2500	0.21583	5.34719	2500	0.13420	0.38310	1:1.6083
PROTOTYPE (FLiBe @ 700°C)			MODEL (Dowtherm A @ 119.662°C)			
Re	T_e	$(T_{H0}-T_{C0})_p$	Re	$(T_{H0}-T_{C0})_R$	$(T_{H0}-T_{C0})_m$	T_e
500	709.31615	9.31615	500	1:3.3	2.82308	122.48533
750	706.21077	6.21077	750	1:3.3	1.88205	121.54430
1000	704.65808	4.65808	1000	1:3.3	1.41154	121.07379
1250	703.72646	3.72646	1250	1:3.3	1.12923	120.79148
1500	703.10538	3.10538	1500	1:3.3	0.94103	120.60328
1750	702.66176	2.66176	1750	1:3.3	0.80659	120.46884
2000	702.32904	2.32904	2000	1:3.3	0.70577	120.36802
2250	702.07026	2.07026	2250	1:3.3	0.62735	120.28960
2500	701.86323	1.86323	2500	1:3.3	0.56462	120.22687

Table 36. Requisite flow conditions between FLiBe and Dowtherm-A at reduced length scale (0.5:1 scale) for Pr = 9.64.

PROTOTYPE (FLiBe @ 750°C)			MODEL (Dowtherm A @ 146.781°C)			
Re	$(u_{ref})_p$	$(\dot{m})_p$	Re	$(u_{ref})_m$	$(\dot{m})_m$	$(u_{ref})_R$
500	0.03609	0.88565	500	0.02064	0.05751	1:1.7487
750	0.05414	1.32848	750	0.03096	0.08627	1:1.7487
1000	0.07219	1.77130	1000	0.04128	0.11503	1:1.7487
1250	0.09023	2.21413	1250	0.05160	0.14379	1:1.7487
1500	0.10828	2.65696	1500	0.06192	0.17254	1:1.7487
1750	0.12633	3.09978	1750	0.07224	0.20130	1:1.7487
2000	0.14437	3.54261	2000	0.08256	0.23006	1:1.7487
2250	0.16242	3.98544	2250	0.09288	0.25881	1:1.7487
2500	0.18047	4.42826	2500	0.10320	0.28757	1:1.7487
PROTOTYPE (FLiBe @ 750°C)			MODEL (Dowtherm A @ 146.781°C)			
Re	T_e	$(T_{H0}-T_{C0})_p$	Re	$(T_{H0}-T_{C0})_R$	$(T_{H0}-T_{C0})_m$	T_e
500	761.24940	11.24940	500	1:3.3	3.40891	150.18985
750	757.49960	7.49960	750	1:3.3	2.27261	149.05355
1000	755.62470	5.62470	1000	1:3.3	1.70445	148.48540
1250	754.49976	4.49976	1250	1:3.3	1.36356	148.14451
1500	753.74980	3.74980	1500	1:3.3	1.13630	147.91724
1750	753.21411	3.21411	1750	1:3.3	0.97397	147.75492
2000	752.81235	2.81235	2000	1:3.3	0.85223	147.63317
2250	752.49987	2.49987	2250	1:3.3	0.75754	147.53848
2500	752.24988	2.24988	2500	1:3.3	0.68178	147.46272

Table 37. Similarity scaling results between FLiBe and Dowtherm-A at reduced length scale (0.5:1 scale) for Pr = 7.95.

PROTOTYPE (FLiBe @ 800°C)			MODEL (Dowtherm A @ 177.805°C)			Ratio (m/m)/(p/m)	
Geometrics							
$(A_{ref})_p$	11670.22	mm^2	$(A_{ref})_m$	2917.555	mm^2	1:4	0.25
$(D_{cyl})_p$	121.89744	mm	$(D_{cyl})_m$	60.94872	mm	1:2	0.5
$(R_{cyl})_p$	60.94872	mm	$(R_{cyl})_m$	30.47436	mm	1:2	0.5
$(H_{cyl})_p$	309.01075	mm	$(H_{cyl})_m$	154.50537	mm	1:2	0.5
$(D_{pebble})_p$	30.00000	mm	$(D_{pebble})_m$	15.00000	mm	1:2	0.5
$(A_{s,pebble})_p$	2827.433	mm^2	$(A_{s,pebble})_m$	706.85835	mm^2	1:4	0.25
$(V_{pebble})_p$	14137.167	mm^3	$(V_{pebble})_m$	1767.14587	mm^3	1:8	0.125
$(V_{t\ pebble})_p$	1060287.5	mm^3	$(V_{t\ pebble})_m$	132535.94	mm^3	1:8	0.125
$(V_{cyl,\ pebble\ region})_p$	2650718.8	mm^3	$(V_{cyl,\ pebble\ region})_m$	331339.85	mm^3	1:8	0.125
$(H_{pebble\ region})_p$	227.13529	mm	$(H_{pebble\ region})_m$	113.56765	mm	1:2	0.5
$(H_{additional})_p$	81.87546	mm	$(H_{additional})_m$	40.93773	mm	1:2	0.5
Thermophysical Properties (Equations)							
$(\rho)_p$	2082.30110	kg/m^3	$(\rho)_m$	927.45103	kg/m^3	1:2.25	0.445
$(\mu)_p$	0.00384	kg/ms	$(\mu)_m$	0.00045	kg/ms	1:8.58	0.117
$(\nu)_p$	1.84302E-06	m^2/s	$(\nu)_m$	4.821E-07	m^2/s	1:3.82	0.262
$(Cp_f)_p$	2415.78	J/kgK	$(Cp_f)_m$	2017.215	J/kgK	1:1.2	0.835
$(k)_p$	1.16627	W/mK	$(k)_m$	0.11345	W/mK	1:10.3	0.097
$(Pr)_p$	7.949346	-	$(Pr)_m$	7.95024	-	1:1	1.000
Flow/Heating Conditions							
T_{in}	800	°C	T_{in}	177.8049	°C	-	-
T_{in}	1073.15	K	T_{in}	450.9549	K	-	-
$(Q)_p$	320.914	W	$(Q)_m$	4.73048	W	1:67.84	0.0147

Table 38. Requisite flow conditions between FLiBe and Dowtherm-A at reduced length scale (0.5:1 scale) for Pr = 7.95.

PROTOTYPE (FLiBe @ 800°C)			MODEL (Dowtherm A @ 177.805°C)			
Re	$(u_{ref})_p$	$(\dot{m})_p$	Re	$(u_{ref})_m$	$(\dot{m})_m$	$(u_{ref})_R$
500	0.03072	0.74645	500	0.01607	0.04348	1:1.9114
750	0.04608	1.11968	750	0.02411	0.06523	1:1.9114
1000	0.06143	1.49290	1000	0.03214	0.08697	1:1.9114
1250	0.07679	1.86613	1250	0.04018	0.10871	1:1.9114
1500	0.09215	2.23935	1500	0.04821	0.13045	1:1.9114
1750	0.10751	2.61258	1750	0.05625	0.15220	1:1.9114
2000	0.12287	2.98581	2000	0.06428	0.17394	1:1.9114
2250	0.13823	3.35903	2250	0.07232	0.19568	1:1.9114
2500	0.15359	3.73226	2500	0.08035	0.21742	1:1.9114
PROTOTYPE (FLiBe @ 800°C)			MODEL (Dowtherm A @ 177.805°C)			
Re	T_e	$(T_{H0}-T_{C0})_p$	Re	$(T_{H0}-T_{C0})_R$	$(T_{H0}-T_{C0})_m$	T_e
500	813.34722	13.34722	500	1:3.3	4.04461	181.84951
750	808.89815	8.89815	750	1:3.3	2.69641	180.50130
1000	806.67361	6.67361	1000	1:3.3	2.02231	179.82720
1250	805.33889	5.33889	1250	1:3.3	1.61785	179.42274
1500	804.44907	4.44907	1500	1:3.3	1.34820	179.15310
1750	803.81349	3.81349	1750	1:3.3	1.15560	178.96050
2000	803.33681	3.33681	2000	1:3.3	1.01115	178.81605
2250	802.96605	2.96605	2250	1:3.3	0.89880	178.70370
2500	802.66944	2.66944	2500	1:3.3	0.80892	178.61382

Appendix C: Sample of Numerical Data

Table 39. Numerical results for FLiBe at Pr = 19.4 with N = 75 pebbles.

T_{FLiBe}=600°C					
Re	HTC (W/m^2K)	Nu (hD_p/k)	High (Pa)	Low (Pa)	ΔP (Pa)
500	3940.781	110.8755	5033.795	248.7913	4785
750	5079.477	142.9132	5284.143	243.4651	5040.68
1000	6115.888	172.073	5600.567	239.6595	5360.91
1250	7058.043	198.5809	6006.977	217.1319	5789.85
1500	7949.742	223.6693	6497.59	208.81	6288.78
1750	8780.634	247.0467	7062.091	208.2615	6853.83
2000	9594.482	269.9447	7745.884	173.3051	7572.58
2250	10354.96	291.341	8408.046	157.9233	8250.12
2500	11102.08	312.3616	9343.995	155.0779	9188.92

Table 40. Numerical results for Dowtherm-A at full length scale (1:1) for Pr = 19.4 with N = 75 pebbles.

T_{FLiBe} (600°C) = $T_{Dowtherm-A}$ (68.058°C)					
Re	HTC (W/m^2K)	Nu (hD_p/k)	High (Pa)	Low (Pa)	ΔP (Pa)
500	435.92	99.82008	1788.705	93.48964	1695.22
750	543.8839	124.5424	1801.268	93.49031	1707.78
1000	645.9412	147.9122	1817.653	92.95649	1724.7
1250	741.5925	169.8152	1835.833	92.78591	1743.05
1500	834.6887	191.133	1861.606	92.52519	1769.08
1750	925.4611	211.9187	1886.534	91.59371	1794.94
2000	1012.474	231.8435	1917.466	90.60696	1826.86
2250	1095.893	250.9454	1945.587	88.63606	1856.95
2500	1180.089	270.2252	1989.34	87.02606	1902.31

Table 41. Numerical results for Dowtherm-A at reduced length scale (0.75:1) for Pr = 19.4 with N = 75 pebbles.

T_{FLiBe} (600°C) = $T_{Dowtherm-A}$ (68.058°C)					
Re	HTC (W/m^2K)	Nu (hD_p/k)	High (Pa)	Low (Pa)	ΔP (Pa)
500	545.1248	93.61994	1506.168	227.3168	1278.85
750	695.3253	119.4154	1524.462	227.373	1297.09
1000	841.3425	144.4925	1549.828	227.1817	1322.65
1250	982.9014	168.8039	1578.794	226.5274	1352.27
1500	1121.356	192.5821	1612.248	225.6225	1386.63
1750	1254.886	215.5146	1654.931	224.9952	1429.94
2000	1386.077	238.0454	1697.346	225.0379	1472.31
2250	1510.791	259.4638	1753.938	222.1068	1531.83
2500	1631.564	280.2054	1806.563	221.6048	1584.96

Table 42. Numerical results for Dowtherm-A at reduced length scale (0.5:1) for Pr = 19.4 with N = 75 pebbles.

T_{FLiBe} (600°C) = $T_{Dowtherm-A}$ (68.058°C)					
Re	HTC (W/m^2K)	Nu (hD_p/k)	High (Pa)	Low (Pa)	ΔP (Pa)
500	797.4986	91.30847	1031.573	149.7894	881.784
750	1042.02	119.3046	1074.507	147.7903	926.717
1000	1271.409	145.5682	1136.242	145.9252	990.317
1250	1491.335	170.7483	1203.043	142.4077	1060.64
1500	1699.861	194.6232	1288.755	138.2907	1150.46
1750	1902.432	217.8163	1397.247	131.4343	1265.81
2000	2096.943	240.0865	1515.956	126.7416	1389.21
2250	2287.737	261.9312	1620.982	115.5358	1505.45
2500	2465.032	282.2303	1784.05	113.3401	1670.71